Eddy Parameterisation and Eddy Energy Budget



Ke Zhao

Mansfield College

University of Oxford

A thesis submitted for the degree of

Master of Science by Research

Trinity 2026

Contents

1 Introduction 1

2 Framework of Thickness-Weighted Average 6

2.1 Boussinesq Primitive Equations in the Buoyancy Coordinates 6

2.2 Thickness-Weighted Average and Eliassen-Palm tensor 11

2.3 Spherical Buoyancy Coordinates 21

2.4 GEOMETRIC Framework for Eddy Parameterisation 24

2.5 Eddy Stress Tensor 26

2.6 Summary 33

3 Eddy Energy Definition 34

3.1 Eddy Energy under the Framework of thickness-weighted Average . . . 34

3.2 Eddy Energy Constraint on the Eliassen-Palm Stress Tensor 37

3.3 Summary 40

4 Eddy Energy Cycle 41

4.1 Eddy Kinetic Energy Equation 41

4.2 Eddy Potential Energy Equation 46

4.3 Energy Conversion from the Perspective of the Mean Field 50

4.4 Energy Conversion from the Perspective of the Eddy Field 53

4.5 Summary 55

5 Diagnostic Analysis of Model Results 56

5.1 Overview of MITgcm and Model Configuration 57
5.2 Eddy Energy 58
5.3 Eddy Energy Source 64
5.4 The Phase Speed of Long Baroclinic Rossby Wave 70
5.5 Positive Correlation between EPE and EKE 73
5.6 Summary 83

6 Discussion and Conclusions 86
6.1 Summary of the Thesis 86
6.2 Future Work 88

References 90

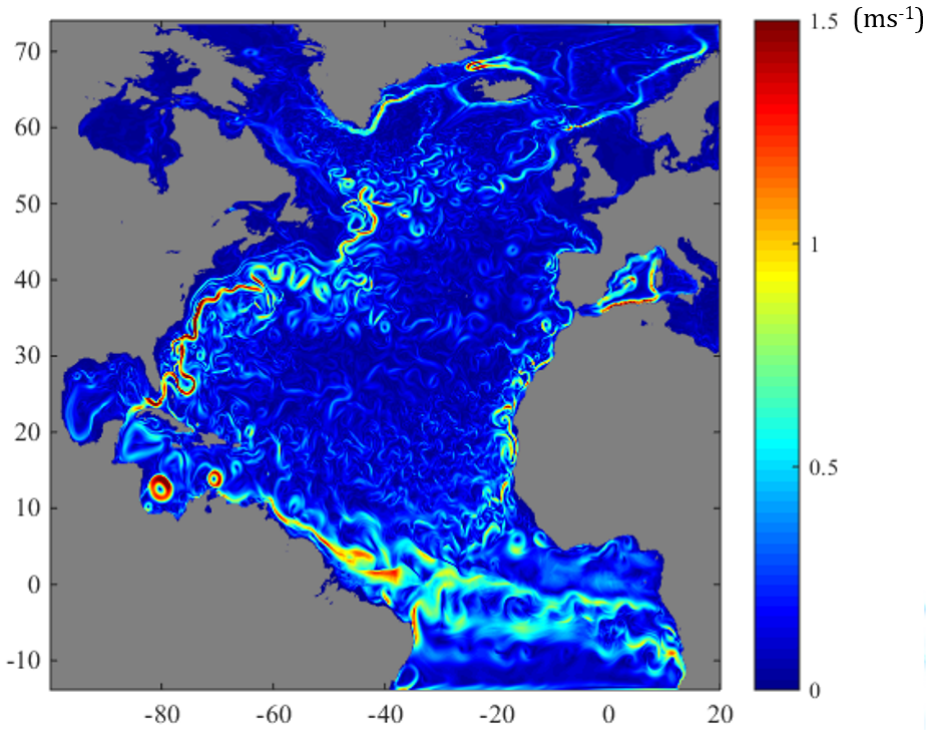


Figure: Snapshot of the horizontal speed ($\mathrm{m\ s^{-1}}$) at the sea surface in March from the MITgcm North Atlantic simulation analysed in this thesis.

Abstract

Mesoscale eddies strongly influence ocean circulation and tracer transport, yet remain unresolved in coarse-resolution climate models. The GEOMETRIC parameterisation constrains the Eliassen-Palm (E-P) eddy stress tensor using total eddy energy, but determining this energy prognostically remains challenging. This thesis investigates the definition, budget, and diagnosis of eddy kinetic energy (EKE) and eddy potential energy (EPE) within the thickness-weighted averaging (TWA) framework.

EKE is defined through thickness-weighted horizontal velocity variance, while EPE uses isopycnal averaging to preserve non-negativity under stable stratification and consistency with the E-P tensor. Applying the Cauchy-Schwarz inequality in the low Rossby number limit, with small layer-thickness perturbations, yields an energy bound on the TWA E-P tensor, linking TWA energetics to GEOMETRIC. Complementary budget derivations identify the inner product of residual-mean velocity and E-P tensor divergence as the primary mean–eddy energy conversion term.

Diagnostics use one year of five-day snapshots from a $1/10^\circ$ MITgcm North Atlantic simulation. Model outputs are mapped into neutral density coordinates, and a four-month moving average separates the mean and eddy fields. Diagnosed energy distributions are qualitatively consistent with Argo and altimetry estimates, showing energetic structures along the Gulf Stream and its extension, substantial EPE in the subpolar gyre, and basin-integrated EPE exceeding EKE. Baroclinic instability and Montgomery potential work are major sources in the EPE and EKE budgets, respectively, while vertical buoyancy flux indicates net conversion from EPE to EKE. Long Rossby wave speeds for the first baroclinic mode are broadly consistent with the latitude dependence of observed westward eddy propagation speeds. EKE-weighted least squares regression in log–log space captures energetic EPE structures better than ordinary least squares, yet time-varying coefficients and regional errors show that EKE acts as a diagnostic constraint in energetic regions rather than a complete EPE parameterisation.

Chapter 1

Introduction

Eddies are ubiquitous in the ocean and are perpetually created, propagated and dissipated. The energetic nature of mesoscale eddies is exemplified by the visual evidence in the figure on the table of contents page. Generally, these eddies are on the scale of the Rossby deformation radius, typically ranging from 10 km to 100 km (Chelton et al., 1998), as demonstrated in the diagnostic results presented in later chapters. Mesoscale eddies are primarily generated via baroclinic instability, which arises from the horizontal density gradient in a rotating, stably stratified fluid. Eddies play an important role in the oceanic transport of momentum, heat, salt and passive tracers including CO_2, O_2. The spatial structure and the variability of the eddy field are often quantified using the eddy energy, especially eddy kinetic energy (EKE), as established in foundational studies Qiu (1999) and Chelton et al. (2007).

In terms of numerical simulation, ocean models are categorised into climate models, eddy-permitting models and eddy-resolving models, based on their horizontal resolution. Specifically, an eddy-resolving model requires a horizontal resolution at least of the order of 10km and an integration of thousands of years to reach equilibrium in the deep ocean. While it is currently feasible to run such high-resolution ocean models over several decades, this remains insufficient for

the need of climate sensitivity studies. Standard climate models typically employ a resolution of 1° as noted in the Intergovernmental Panel on Climate Change (IPCC) reports (Eyring et al., 2021). Under such circumstances, the influence of eddies on large-scale circulation must be represented through eddy parameterisations. Consequently, there remains a sustained demand for a physically realistic parameterisations to represent sub-grid eddy processes.

The GEOMETRIC framework for the eddy closure was proposed by Marshall et al. (2012), where the eddy stress tensor is parameterised and constrained by the total eddy energy. The coefficients within this framework are dimensionless and can be geometrically characterised as a tilted three-dimensional ellipsoid. The framework naturally associates with the Gent and McWilliams eddy parameterisation (GM90) (Gent and McWilliams, 1990) through eddy buoyancy fluxes.

In the study of baroclinic instability, the Eady problem serves as a critical benchmark due to its analytical wave solution. In the Eady problem, the eddy streamfunction grows exponentially at a maximum rate of $0.31 f U_z/\mathcal{N}_0$, known as the Eady growth rate (Eady, 1949; Vallis, 2017). Here, f is the Coriolis parameter, U_z is the vertical velocity shear, and $\mathcal{N}_0$ is the buoyancy frequency. The eddy energy grows at twice this rate, $0.61 f U_z/\mathcal{N}_0$. The GEOMETRIC parameterisation exhibits the desirable property of preserving this functional form, while mathematically bounding the coefficient in front of the eddy energy growth rate by 1 rather than 0.61, as shown in Marshall et al. (2012).

Bachman et al. (2017) have compared the performance of five eddy parameterisations, including the GEOMETRIC framework, in reproducing the thickness diffusivity for the nonlinear Eady problem within an idealised ocean model, illustrated by Figure 1.1. Among these, (a) GEOMETRIC, (c) Bachman and Fox-Kemper (2013) and (d) Eden and Greatbatch (2008) significantly out-perform the other eddy parameterisations. However, these schemes typically require precise knowledge

of the total eddy energy or EKE field, which is usually unavailable or tenuous in practical applications. The GEOMETRIC framework matches the diagnostic diffusivity the best among the eddy closures concerned over a wide range of values. Additionally, in idealised configurations, the GEOMETRIC parameterisation produces "eddy saturation" – a phenomenon where the Antarctic Circumpolar Current (ACC) volume transport exhibits minimal sensitivity to the surface wind forcing with sufficient resolution, shown in Figure 1.2 from Munday et al. (2013) and Mak et al. (2018). In contrast, coarse-resolution models employing the standard GM90 with a constant thickness diffusivity fail to capture this behaviour.

The GEOMETRIC parameterisation is constrained by the eddy energy (the sum of eddy kinetic energy and eddy potential energy). However, the practical difficulty in determining eddy energy for prognostic simulations hinders the widespread application of this framework. Therefore, this thesis aims to investigate the eddy energy cycle and to contribute ultimately towards establishing a parameterisation for the eddy energy itself. Relevant prior research includes the analysis of the mean kinetic energy budget using thickness-weighted averaging (Aiki and Richards, 2008). Roullet et al. (2014) provided the first global diagnosis of eddy potential energy (EPE) using Argo float data – a global array of free-drifting profiling floats measuring hydrological data in the upper 2000 m. They also estimated surface EKE from satellite altimetry via geostrophic balance. This thesis compares diagnostic results with eddy energy estimates derived from such observations.

The remainder of this thesis is structured as follows. Chapter 2 establishes the theoretical framework of thickness-weighted averaging (TWA), following the dual-basis formulation of Young (2012) and reviews the GEOMETRIC parameterisation (Marshall et al., 2012). Chapter 3 proposes the definition of EKE and EPE in the buoyancy coordinates and validates the role of total eddy energy as a constraint for the eddy stress tensor within the TWA framework at small Rossby numbers.

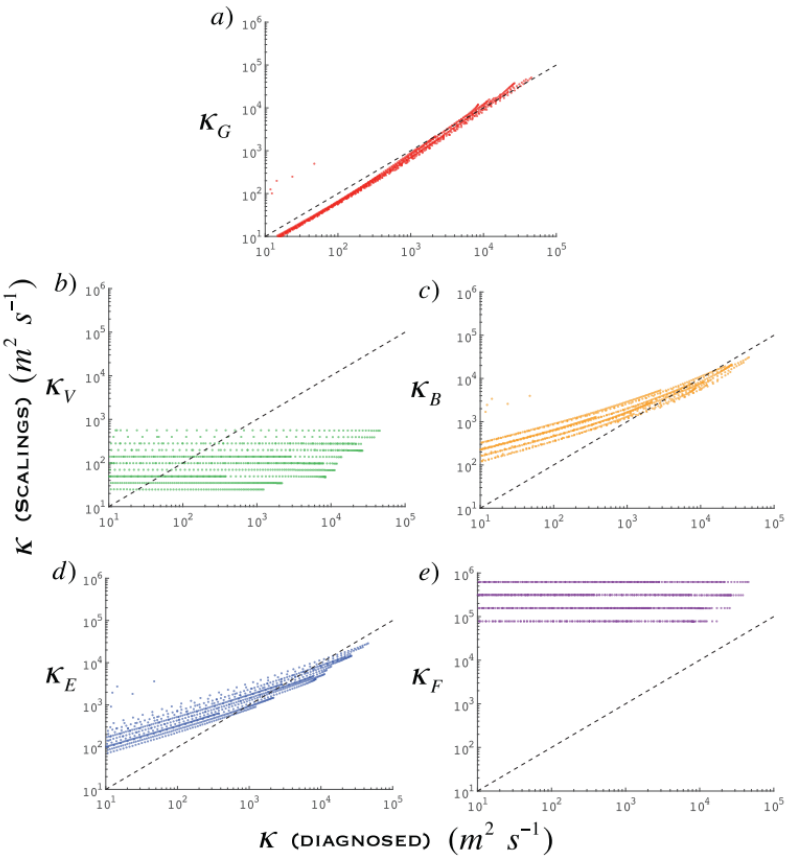
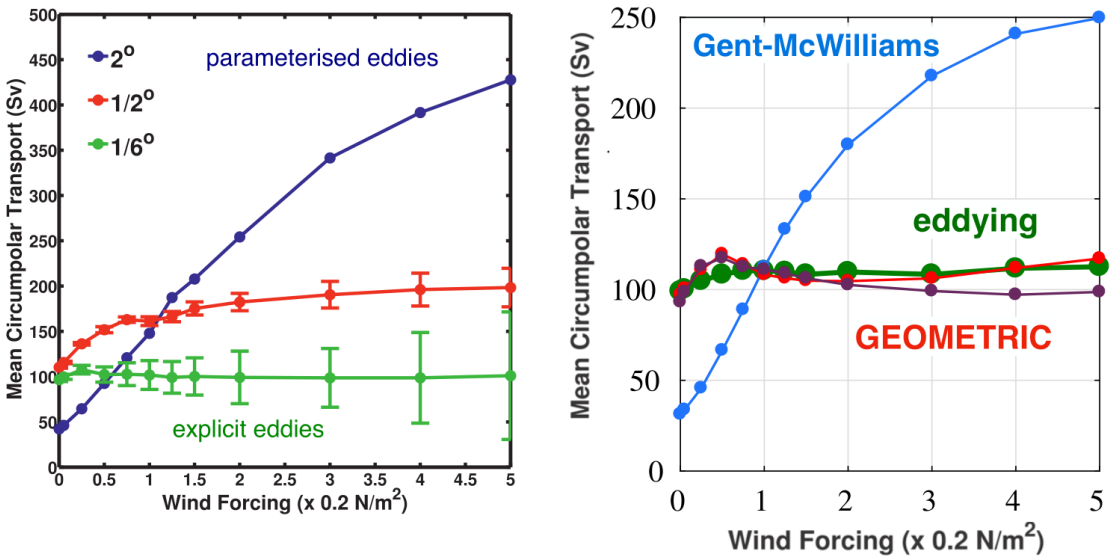


Figure 1.1: Scatter plots of domain-averaged scaling diffusivity against diagnostic diffusivity ($\mathrm{m}^2\ \mathrm{s}^{-1}$) for sixteen simulations, reproduced from Bachman et al. (2017). (a) The GEOMETRIC framework in Marshall et al. (2012), (b) Visbeck et al. (1997), (c) Bachman and Fox-Kemper (2013), (d) Eden and Greatbatch (2008), (e) Fox-Kemper et al. (2008). The GEOMETRIC framework performs better in reproducing the diffusivity than other eddy parameterisations.

Furthermore, Chapter 4 derives the equations for the eddy energy cycle, followed by a diagnostic analysis of an eddy-resolving North Atlantic simulation in Chapter 5. Conclusions and suggestions for future work are summarised in Chapter 6.



(Munday et al., 2013) *(Mak et al., 2018)*

Figure 1.2: ACC volume transport (Sv) as a function of wind forcing, reproduced from Munday et al. (2013) and Mak et al. (2018). In both panels, wind forcing is scaled by $0.2\,\mathrm{N\ m^{-2}}$. In the left panel, the blue dots represent the coarse-resolution model with GM90 eddy parameterisation, while the red and green dots denote two eddy-permitting models showing much less sensitivity of ACC volume transport to the wind stress. This is known as "eddy saturation". The right panel shows the ACC volume transport on a β-plane for varying wind stress.

Chapter 2

Framework of Thickness-Weighted Average

This chapter reviews and establishes the framework of the thickness-weighted average (TWA) in buoyancy coordinates. The derivation presented in Sections 2.1 and 2.2 primarily follows the foundational theory developed by Young (2012). Section 2.3 provides necessary background on tensor analysis for a rigorous expression of nabla operator in the general curvilinear coordinates. Section 2.4 reviews the GEOMETRIC parameterisation of eddy stress tensor proposed by Marshall et al. (2012). Finally, Section 2.5 examines various forms of eddy stress tensor and the corresponding transformations based on Maddison and Marshall (2013).

2.1 Boussinesq Primitive Equations in the Buoyancy Coordinates

Young (2012) formulated the Boussinesq primitive equations in a buoyancy coordinate system, applied the thickness-weighted average (TWA) to the variables at constant buoyancy, and transformed the equations back into the Cartesian coordinate system. This process facilitates the operation of averaging along the buoyancy

or density surfaces.

The standard Boussinesq primitive equations consist of the horizontal momentum equations, the continuity equation, the thermodynamic equation, and the hydrostatic balance, which is simplified from the vertical momentum equation. In Cartesian coordinates (x, y, z), these are expressed as:

$$\frac{\mathrm{D}u}{\mathrm{D}t} - fv + \frac{\partial p}{\partial x} = \mathcal{X}, \tag{2.1}$$

$$\frac{\mathrm{D}v}{\mathrm{D}t} + fu + \frac{\partial p}{\partial y} = \mathcal{Y}, \tag{2.2}$$

$$\frac{\partial p}{\partial z} = b, \tag{2.3}$$

$$\frac{\partial u}{\partial x} + \frac{\partial v}{\partial y} + \frac{\partial w}{\partial z} = 0, \tag{2.4}$$

$$\frac{\mathrm{D}b}{\mathrm{D}t} = \varpi, \tag{2.5}$$

where (u, v, w) are 3-D velocities, f is the Coriolis parameter and the buoyancy b is defined as $b \stackrel{def}{=} -g\left(\rho - \rho_0\right)/\rho_0$. For brevity of notation, p refers to the pressure normalised by ρ_0 and here after goes by the name of "pressure". $\mathcal{X}, \mathcal{Y}$ represent non-conservative body forces. The term ϖ denotes diapycnal processes, dominated by temperature and salinity fluctuations. If the effects of haline process are neglected, an adiabatic process would lead to $\varpi = 0$. It is important to note that in this z-coordinate formulation, the continuity equation (2.4) acts as a linear constraint on the velocity field rather than a prognostic equation.

The material derivative is defined as

$$\frac{\mathrm{D}}{\mathrm{D}t} \stackrel{def}{=} \frac{\partial}{\partial t} + u\frac{\partial}{\partial x} + v\frac{\partial}{\partial y} + w\frac{\partial}{\partial z}\,. \tag{2.6}$$

For notational convenience, subscripts denote partial derivatives, e.g., $\theta_x \stackrel{def}{=} \frac{\partial \theta}{\partial x}$.

The transformation to buoyancy coordinates $(\tilde{x}, \tilde{y}, \tilde{b}, \tilde{t})$ is defined by:

$$\tilde{x} = x,\ \tilde{y} = y,\ \tilde{b} = b\,(x, y, z, t)\,,\ \tilde{t} = t. \tag{2.7}$$

Here, the tilde distinguishes the buoyancy coordinates from the Cartesian system. We assume stable stratification, implying a monotonic relationship between buoyancy and depth ($b_z \neq 0$).

Following Young (2012), the differential operators transform as

$$\partial_x = \partial_{\tilde{x}} + b_x \partial_{\tilde{b}}\,, \tag{2.8}$$

$$\partial_y = \partial_{\tilde{y}} + b_y \partial_{\tilde{b}}\,, \tag{2.9}$$

$$\partial_z = b_z \partial_{\tilde{b}}\,, \tag{2.10}$$

$$\partial_t = \partial_{\tilde{t}} + b_t \partial_{\tilde{b}}\,. \tag{2.11}$$

$\zeta(\tilde{x}, \tilde{y}, \tilde{b}, \tilde{t})$ is the depth of a buoyancy surface, i.e., $z = \zeta$. The isopycnal thickness σ, a fundamental quantity in TWA, is defined as the Jacobian of the vertical transformation:

$$\sigma \overset{def}{=} \zeta_{\tilde{b}} = b_z^{-1}. \tag{2.12}$$

Differentiation of ζ with $(2.8 - 2.11)$ yields

$$\zeta_{\tilde{x}} = -\sigma b_x\,, \tag{2.13}$$

$$\zeta_{\tilde{y}} = -\sigma b_y\,, \tag{2.14}$$

$$\sigma = b_z^{-1}, \tag{2.15}$$

$$\zeta_{\tilde{t}} = -\sigma b_t\,. \tag{2.16}$$

Substituting into $(2.8 - 2.11)$, we obtain the derivatives in terms of σ and ζ:

$$\partial_x = \partial_{\tilde{x}} - \zeta_{\tilde{x}} \sigma^{-1} \partial_{\tilde{b}} \,, \tag{2.17}$$

$$\partial_y = \partial_{\tilde{y}} - \zeta_{\tilde{y}} \sigma^{-1} \partial_{\tilde{b}} \,, \tag{2.18}$$

$$\partial_z = \sigma^{-1} \partial_{\tilde{b}} \,, \tag{2.19}$$

$$\partial_t = \partial_{\tilde{t}} - \zeta_{\tilde{t}} \sigma^{-1} \partial_{\tilde{b}} \,. \tag{2.20}$$

Using the thermodynamic equation (2.5) and the relations above, the vertical velocity w can be expressed in buoyancy coordinates as

$$w = \zeta_{\tilde{t}} + u\zeta_{\tilde{x}} + v\zeta_{\tilde{y}} + \varpi\zeta_{\tilde{b}} \,. \tag{2.21}$$

Consequently, the material derivative in buoyancy coordinates becomes:

$$\frac{\mathrm{D}}{\mathrm{D}t} = \partial_{\tilde{t}} + u\partial_{\tilde{x}} + v\partial_{\tilde{y}} + \varpi\partial_{\tilde{b}} \,. \tag{2.22}$$

This formulation highlights that ϖ acts as a diapycnal velocity, transporting material across buoyancy surfaces. Furthermore, Eq. (2.21) implies the prognostic equation for the vertical position of the isopycnal:

$$\frac{\mathrm{D}\zeta}{\mathrm{D}t} = w \,. \tag{2.23}$$

Substituting the vertical velocity expression into the Cartesian non-divergent condition (2.4) leads to the conservation of mass in buoyancy coordinates, known as the thickness equation:

$$\sigma_{\tilde{t}} + (\sigma u)_{\tilde{x}} + (\sigma v)_{\tilde{y}} + (\sigma\varpi)_{\tilde{b}} = 0. \tag{2.24}$$

Applying the thickness equation (2.24), the material derivative for any scalar field $\theta(\tilde{x}, \tilde{y}, \tilde{b}, \tilde{t})$ in the buoyancy coordinates can be written in flux form:

$$\frac{\mathrm{D}\theta}{\mathrm{D}t} = \sigma^{-1}\left[(\sigma\theta)_{\tilde{t}} + (\sigma u\theta)_{\tilde{x}} + (\sigma v\theta)_{\tilde{y}} + (\sigma\varpi\theta)_{\tilde{b}}\right]. \tag{2.25}$$

To complete the transformation of the Boussinesq primitive equations in the buoyancy coordinate system, we introduce the Montgomery potential m, following Young (2012), defined as

$$m\left(\tilde{x}, \tilde{y}, \tilde{b}, \tilde{t}\right) \stackrel{def}{=} p - \tilde{b}\,\zeta. \tag{2.26}$$

The hydrostatic balance (2.3) simplifies to:

$$m_{\tilde{b}} + \zeta = 0. \tag{2.27}$$

Similarly, the horizontal pressure gradient in Cartesian coordinates transforms to the gradient of the Montgomery potential along buoyancy surfaces:

$$m_{\tilde{x}} = p_x, \quad m_{\tilde{y}} = p_y. \tag{2.28}$$

The Montgomery potential makes an adjustment to the pressure for the convenience of differentiating along the buoyancy surface.

Thus, the Boussinesq primitive equations in the buoyancy coordinate system are summarised as:

$$\frac{\mathrm{D}u}{\mathrm{D}t} - fv + m_{\tilde{x}} = \mathcal{X}, \tag{2.29}$$

$$\frac{\mathrm{D}v}{\mathrm{D}t} + fu + m_{\tilde{y}} = \mathcal{Y}, \tag{2.30}$$

$$\zeta + m_{\tilde{b}} = 0, \tag{2.31}$$

$$\sigma_{\tilde{t}} + (\sigma u)_{\tilde{x}} + (\sigma v)_{\tilde{y}} + (\sigma\varpi)_{\tilde{b}} = 0. \tag{2.32}$$

In contrast to the Cartesian formulation $(2.1 - 2.5)$, where the continuity equation (2.4) acts as a linear constraint on the velocity field, the buoyancy coordinate system transforms this diagnostic requirement into the prognostic thickness equation (2.32). Additionally, the thermodynamic equation (2.5) is implicitly satisfied by the coordinate definition $\mathrm{D}\tilde{b}/\mathrm{D}t \equiv \varpi$, reducing of the number of governing equations by one.

2.2 Thickness-Weighted Average and Eliassen-Palm tensor

Following the theoretical framework established by Young (2012), this section introduces the thickness-weighted average (TWA) and its application to the Boussinesq equations.

We define three distinct averaging operators: the Eulerian average $\overline{\theta}^z$, the isopycnal average $\overline{\theta}^b$, and the TWA $\hat{\theta}$ (Young, 2012). The conventional Eulerian average is conducted at constant depths in the Cartesian coordinate. In contrast, the latter two operators are defined in the buoyancy coordinate. This is physically motivated by the tendency of tracers to be transported along density surfaces with minimal diapycnal mixing (Young, 2012; Jansen et al., 2024). The operator $\overline{\theta}^b$ denotes averaging along isopycnals; conceptually, this corresponds to sampling a variable while following a specific buoyancy surface (e.g., a neutral density surface). The distinction between Eulerian and isopycnal averaging is illustrated in Figure 2.1, adapted from Aiki et al. (2016). In the Eulerian framework (Figure 2.1(b), the average can create a spurious, non-physical water mass by blending layers. Conversely, the isopycnal average (Figure 2.1(c) treats density as the coordinate and the surface height as the variable, thereby preserving the water mass structure.

The TWA incorporates the layer thickness σ into its formulation and is defined as

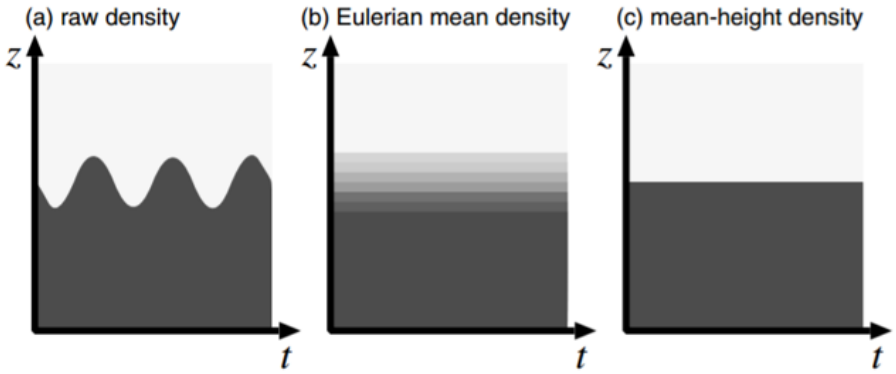


Figure 2.1: Schematic diagram from Aiki et al. (2016) comparing Eulerian and isopycnal averaging for a two-layer flow: (a) shows the time-evolving raw profile; (b) shows the mean density at fixed depths (Eulerian mean); (c) shows the mean interface height (isopycnal mean).

(Young, 2012; Lee et al., 1997)

$$\hat{\theta} \overset{def}{=} \frac{\overline{\sigma\theta}^{b}}{\overline{\sigma}^{b}}, \tag{2.33}$$

where the overline denotes the isopycnal average. The physical significance of TWA is demonstrated in Figure 2.2: while an Eulerian mean might incorrectly indicate zero net transport, the TWA accurately captures the net volume transport to the right by weighting the velocity with the fluctuating layer thickness Lee et al. (1997). For a comprehensive recent study applying these three average operators to the hydrostatic Boussinesq system, see Jansen et al. (2024).

For brevity of notation, the superscript b is omitted hereafter when operating within buoyancy coordinates. The averaged field $\theta(\tilde{x}, \tilde{y}, \tilde{b}, \tilde{t})$ in the buoyancy coordinate system is simply expressed as $\overline{\theta}(\tilde{x}, \tilde{y}, \tilde{b}, \tilde{t})$. The average is treated as an ensemble average, which is a linear operator satisfying:

$$\overline{\overline{\theta}} = \overline{\theta}, \quad \overline{\overline{\theta}\phi} = \overline{\theta\phi}, \quad \overline{\partial_{\tilde{x}}\theta} = \partial_{\tilde{x}}\overline{\theta}, \tag{2.34}$$

where θ and ϕ are random quantities. In buoyancy coordinates, the coordinate $\tilde{b}$

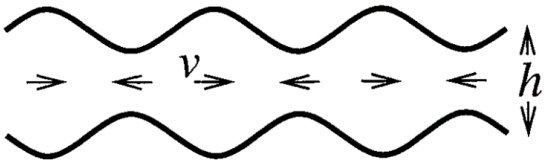


Figure 2.2: Schematic diagram of the thickness-weighted average (Lee et al., 1997). The Eulerian average fails to capture net transport when thickness and velocity are correlated; the TWA correctly captures the volume transport by incorporating the layer thickness.

is unaffected by the average by definition. We apply the Reynolds decomposition for ensemble averages, $\theta = \overline{\theta} + \theta'$, and the TWA decomposition, $\theta = \hat{\theta} + \theta''$, where by definition $\widehat{\theta''} = 0$ (Young, 2012). Applying TWA to the product of two variables yields:

$$\widehat{\theta\phi} = \hat{\theta}\hat{\phi} + \widehat{\theta''\phi''}\,. \tag{2.35}$$

To rigorously derive the TWA primitive equations, we employ tensor analysis in the non-orthogonal buoyancy coordinate system (Young, 2012; De Szoeke and Bennett, 1993).

The contravariant basis vectors, expressed by superscripts, $\boldsymbol{e}^1, \boldsymbol{e}^2, \boldsymbol{e}^3$ in the buoyancy coordinates are

$$\boldsymbol{e}^1 = \boldsymbol{i},\ \boldsymbol{e}^2 = \boldsymbol{j},\ \boldsymbol{e}^3 = \nabla b\,. \tag{2.36}$$

The covariant basis vectors in the buoyancy coordinates are

$$\boldsymbol{e}_1 = \boldsymbol{i} + \zeta_{\tilde{x}}\,\boldsymbol{k},\ \boldsymbol{e}_2 = \boldsymbol{j} + \zeta_{\tilde{y}}\,\boldsymbol{k},\ \boldsymbol{e}_3 = \sigma\boldsymbol{k}, \tag{2.37}$$

where $\boldsymbol{e}_1, \boldsymbol{e}_2$ are tangent to the buoyancy surface and $\boldsymbol{e}_3$ penetrates the surface.

Any arbitrary vector $\boldsymbol{a}$ can be represented as

$$\boldsymbol{a} = a_1\,\boldsymbol{e}^1 + a_2\,\boldsymbol{e}^2 + a_3\,\boldsymbol{e}^3 = a^1\,\boldsymbol{e}_1 + a^2\,\boldsymbol{e}_2 + a^3\,\boldsymbol{e}_3\,. \tag{2.38}$$

For example, the velocity vector can be written as

$$\begin{aligned}\boldsymbol{u} &= u\,\boldsymbol{i} + v\,\boldsymbol{j} + w\,\boldsymbol{k}\\ &= (u + w\zeta_{\tilde{x}})\,\boldsymbol{e}^1 + \left(v + w\zeta_{\tilde{y}}\right)\boldsymbol{e}^2 + \sigma w\,\boldsymbol{e}^3\\ &= u\,\boldsymbol{e}_1 + v\,\boldsymbol{e}_2 + \left(\sigma^{-1}\zeta_{\tilde{t}} + \varpi\right)\boldsymbol{e}_3\,.\end{aligned} \tag{2.39}$$

If the flow is adiabatic and steady, the third contravariant component remains zero, implying the residual velocity perfectly follows a buoyancy surface.
The divergence of $\boldsymbol{a}$ can be compactly written using its contravariant components:

$$\nabla\cdot\boldsymbol{a} = \sigma^{-1}\left[\left(\sigma a^1\right)_{\tilde{x}} + \left(\sigma a^2\right)_{\tilde{y}} + \left(\sigma a^3\right)_{\tilde{b}}\right]. \tag{2.40}$$

This formula is readily validated via the explicit expression of the covariant basis vectors (2.37).

Applying the average operator to the buoyancy coordinates maps the covariant basis vectors to $\overline{\boldsymbol{e}}_i$. Due to the linearity of the operator, no eddy contribution is present:

$$\overline{\boldsymbol{e}}_1 = \boldsymbol{i} + \overline{\zeta}_{\tilde{x}}\,\boldsymbol{k},\ \overline{\boldsymbol{e}}_2 = \boldsymbol{j} + \overline{\zeta}_{\tilde{y}}\,\boldsymbol{k},\ \overline{\boldsymbol{e}}_3 = \overline{\sigma}\,\boldsymbol{k}. \tag{2.41}$$

The divergence is subsequently transformed to:

$$\nabla\cdot\boldsymbol{a} = \overline{\sigma}^{-1}\left[\left(\overline{\sigma}a^1\right)_{\tilde{x}} + \left(\overline{\sigma}a^2\right)_{\tilde{y}} + \left(\overline{\sigma}a^3\right)_{\tilde{b}}\right], \tag{2.42}$$

which differs from (2.40) solely by the substitution of σ with $\bar{\sigma}$.

Following the application of TWA, the velocity field maps to the residual veloc-

ity $\boldsymbol{u}^\sharp$, with $\hat{u}$ and $\hat{v}$ acting as the horizontal components. In analogy to (2.21), the third component in the Cartesian coordinates can be defined as

$$w^\sharp \overset{def}{=} \overline{\zeta}_{\tilde{t}} + \hat{u}\,\overline{\zeta}_{\tilde{x}} + \hat{v}\,\overline{\zeta}_{\tilde{y}} + \hat{\varpi}\,\overline{\zeta}_{\tilde{b}}\,. \tag{2.43}$$

Accordingly, the 3-D residual velocity is expressed as

$$\begin{aligned} \boldsymbol{u}^\sharp &= \hat{u}\,\boldsymbol{i} + \hat{v}\,\boldsymbol{j} + w^\sharp\,\boldsymbol{k} \\ &= \left(\hat{u} + w^\sharp\,\overline{\zeta}_{\tilde{x}}\right)\overline{\boldsymbol{e}}^1 + \left(\hat{v} + w^\sharp\,\overline{\zeta}_{\tilde{y}}\right)\overline{\boldsymbol{e}}^2 + \overline{\sigma} w^\sharp\,\overline{\boldsymbol{e}}^3 \\ &= \hat{u}\,\overline{\boldsymbol{e}}_1 + \hat{v}\,\overline{\boldsymbol{e}}_2 + \overline{\sigma}^{-1}\left(\overline{\zeta}_{\tilde{t}} + \hat{\varpi}\,\overline{\zeta}_{\tilde{b}}\right)\overline{\boldsymbol{e}}_3\,. \end{aligned} \tag{2.44}$$

Averaging the exact thickness equation (2.24) yields the averaged thickness equation (Young, 2012):

$$\overline{\sigma}_{\tilde{t}} + \left(\overline{\sigma}\hat{u}\right)_{\tilde{x}} + \left(\overline{\sigma}\hat{v}\right)_{\tilde{y}} + \left(\overline{\sigma}\hat{\varpi}\right)_{\tilde{b}} = 0. \tag{2.45}$$

By evaluating the divergence of the residual velocity $\boldsymbol{u}^\sharp$ using (2.42), it matches the left-hand side of the averaged thickness equation (2.45), demonstrating that

$$\nabla \cdot \boldsymbol{u}^\sharp = 0. \tag{2.46}$$

In essence, the incompressibility of the residual velocity field is mathematically equivalent to the averaged thickness equation in the buoyancy coordinate system.

The thickness-weighted averaged material derivative can then be constructed

starting from (2.25):

$$\begin{aligned}\overline{\sigma\frac{\mathrm{D}\theta}{\mathrm{D}t}} &= \left(\overline{\sigma\theta}\right)_{\tilde{t}} + \left(\overline{\sigma u\theta}\right)_{\tilde{x}} + \left(\overline{\sigma v\theta}\right)_{\tilde{y}} + \left(\overline{\sigma\varpi\theta}\right)_{\tilde{b}} \\ &= \left(\overline{\sigma}\hat{\theta}\right)_{\tilde{t}} + \left(\overline{\sigma}\,\widehat{u\theta}\right)_{\tilde{x}} + \left(\overline{\sigma}\,\widehat{v\theta}\right)_{\tilde{y}} + \left(\overline{\sigma}\,\widehat{\varpi\theta}\right)_{\tilde{b}} \\ &= \left[\left(\overline{\sigma}\hat{\theta}\right)_{\tilde{t}} + \left(\overline{\sigma}\hat{u}\hat{\theta}\right)_{\tilde{x}} + \left(\overline{\sigma}\hat{v}\hat{\theta}\right)_{\tilde{y}} + \left(\overline{\sigma}\hat{\varpi}\hat{\theta}\right)_{\tilde{b}}\right] + \left[\left(\overline{\sigma}\,\widehat{u''\theta''}\right)_{\tilde{x}} + \left(\overline{\sigma}\,\widehat{v''\theta''}\right)_{\tilde{y}} + \left(\overline{\sigma}\,\widehat{\varpi''\theta''}\right)_{\tilde{b}}\right].\end{aligned} \tag{2.47}$$

Here, the adjusted material derivative $\mathrm{D}^\sharp/\mathrm{D}t$ is introduced, based entirely on the residual velocity in buoyancy coordinates (Young, 2012):

$$\frac{\mathrm{D}^\sharp}{\mathrm{D}t} \overset{def}{=} \partial_{\tilde{t}} + \hat{u}\,\partial_{\tilde{x}} + \hat{v}\,\partial_{\tilde{y}} + \hat{\varpi}\,\partial_{\tilde{b}}\,. \tag{2.48}$$

With this operator, the vertical component of the residual velocity $w^\sharp$ in (2.43) collapses to:

$$w^\sharp = \frac{\mathrm{D}^\sharp\overline{\zeta}}{\mathrm{D}t}\,. \tag{2.49}$$

Substituting $(2.17-2.20)$ into (2.48), the adjusted material derivative represented in the Cartesian coordinates becomes

$$\frac{\mathrm{D}^\sharp}{\mathrm{D}t} = \partial_t + \hat{u}\,\partial_x + \hat{v}\,\partial_y + w^\sharp\,\partial_z\,. \tag{2.50}$$

Analogous to the procedure of deriving the material derivative (2.25), applying the averaged thickness equation (2.45) expands the adjusted material derivative (2.48) into:

$$\begin{aligned}\frac{\mathrm{D}^\sharp\theta}{\mathrm{D}t} &= \overline{\sigma}^{-1}\left(\overline{\sigma}\theta_{\tilde{t}} + \overline{\sigma}\hat{u}\theta_{\tilde{x}} + \overline{\sigma}\hat{v}\theta_{\tilde{y}} + \overline{\sigma}\hat{\varpi}\theta_{\tilde{b}}\right) \\ &= \overline{\sigma}^{-1}\left[\left(\overline{\sigma}\theta\right)_{\tilde{t}} + \left(\overline{\sigma}\hat{u}\theta\right)_{\tilde{x}} + \left(\overline{\sigma}\hat{v}\theta\right)_{\tilde{y}} + \left(\overline{\sigma}\hat{\varpi}\theta\right)_{\tilde{b}}\right] - \overline{\sigma}^{-1}\theta\left[\overline{\sigma}_{\tilde{t}} + \left(\overline{\sigma}\hat{u}\right)_{\tilde{x}} + \left(\overline{\sigma}\hat{v}\right)_{\tilde{y}} + \left(\overline{\sigma}\hat{\varpi}\right)_{\tilde{b}}\right] \\ &= \overline{\sigma}^{-1}\left[\left(\overline{\sigma}\theta\right)_{\tilde{t}} + \left(\overline{\sigma}\hat{u}\theta\right)_{\tilde{x}} + \left(\overline{\sigma}\hat{v}\theta\right)_{\tilde{y}} + \left(\overline{\sigma}\hat{\varpi}\theta\right)_{\tilde{b}}\right].\end{aligned} \tag{2.51}$$

The eddy-correlation fluxes generated under the TWA framework are defined as

$$\boldsymbol{J}^{\theta} \overset{def}{=} \widehat{u''\theta''}\,\overline{\boldsymbol{e}}_1 + \widehat{v''\theta''}\,\overline{\boldsymbol{e}}_2 + \widehat{\varpi''\theta''}\,\overline{\boldsymbol{e}}_3\,, \tag{2.52}$$

so that its divergence has the form:

$$\nabla\cdot\boldsymbol{J}^{\theta} = \overline{\sigma}^{-1}\left[\left(\overline{\sigma}\,\widehat{u''\theta''}\right)_{\tilde{x}} + \left(\overline{\sigma}\,\widehat{v''\theta''}\right)_{\tilde{y}} + \left(\overline{\sigma}\,\widehat{\varpi''\theta''}\right)_{\tilde{b}}\right]. \tag{2.53}$$

Substituting (2.51) and (2.53) into (2.47), establishes the exact thickness-weighted averaged material derivative (Young, 2012):

$$\frac{\widehat{\mathrm{D}\theta}}{\mathrm{D}t} = \overline{\sigma}^{-1}\left(\overline{\sigma\frac{\mathrm{D}\theta}{\mathrm{D}t}}\right) = \frac{\mathrm{D}^{\sharp}\hat{\theta}}{\mathrm{D}t} + \nabla\cdot J^{\theta}. \tag{2.54}$$

Equation (2.54) formally isolates the advective transport by the residual velocity within the adjusted material derivative from the eddy contributions, which appear exclusively in the divergence of the eddy-correlation fluxes.

To consistently apply TWA to the momentum equations, it is necessary to rigorously treat the gradient of the Montgomery potential, for example $m_{\tilde{x}}$:

$$\sigma m_{\tilde{x}} = \zeta_{\tilde{b}}\, m_{\tilde{x}} = (\zeta m_{\tilde{x}})_{\tilde{b}} - \zeta\,(m_{\tilde{x}})_{\tilde{b}}\ . \tag{2.55}$$

Application of the hydrostatic balance $m_{\tilde{b}} = -\zeta$ from (2.31) leads to

$$\sigma m_{\tilde{x}} = (\zeta m_{\tilde{x}})_{\tilde{b}} + \frac{1}{2}\left(\zeta^2\right)_{\tilde{x}}\ . \tag{2.56}$$

The thickness-weighted averaged Montgomery potential partial derivative (Young,

2012) resolves to

$$\begin{aligned}
\widehat{m_{\tilde{x}}} &= \overline{\sigma}^{-1}\,\overline{\sigma m_{\tilde{x}}} \\
&= \overline{\sigma}^{-1}\left[\left(\overline{\zeta m_{\tilde{x}}}\right)_{\tilde{b}} + \frac{1}{2}\left(\overline{\zeta^2}\right)_{\tilde{x}}\right] \\
&= \overline{\sigma}^{-1}\left[\left(\overline{\zeta}\,\overline{m}_{\tilde{x}}\right)_{\tilde{b}} + \left(\overline{\zeta' m'_{\tilde{x}}}\right)_{\tilde{b}} + \frac{1}{2}\left(\overline{\zeta}^2\right)_{\tilde{x}} + \frac{1}{2}\left(\overline{\zeta'^2}\right)_{\tilde{x}}\right] \\
&= \overline{m}_{\tilde{x}} + \overline{\sigma}^{-1}\left(\overline{\zeta' m'_{\tilde{x}}}\right)_{\tilde{b}} + \frac{1}{2}\,\overline{\sigma}^{-1}\left(\overline{\zeta'^2}\right)_{\tilde{x}}\,, \qquad (2.57)
\end{aligned}$$

which can be elegantly rewritten in vector divergence form:

$$\widehat{m_{\tilde{x}}} = \overline{m}_{\tilde{x}} + \nabla\cdot\left(\frac{1}{2}\,\overline{\sigma}^{-1}\overline{\zeta'^2}\,\overline{\boldsymbol{e}}_1 + \overline{\sigma}^{-1}\,\overline{\zeta' m'_{\tilde{x}}}\,\overline{\boldsymbol{e}}_3\right). \qquad (2.58)$$

Therefore, as derived in Young (2012), the precise formulation of the TWA primitive equations in the buoyancy coordinate system are

$$\frac{\mathrm{D}^{\sharp}\hat{u}}{\mathrm{D}t} - f\hat{v} + \overline{m}_{\tilde{x}} + \nabla\cdot\boldsymbol{E}^u = \hat{\mathcal{X}}, \qquad (2.59)$$

$$\frac{\mathrm{D}^{\sharp}\hat{v}}{\mathrm{D}t} + f\hat{u} + \overline{m}_{\tilde{y}} + \nabla\cdot\boldsymbol{E}^v = \hat{\mathcal{Y}}, \qquad (2.60)$$

$$\overline{\zeta} + \overline{m}_{\tilde{b}} = 0, \qquad (2.61)$$

$$\overline{\sigma}_{\tilde{t}} + \left(\overline{\sigma}\hat{u}\right)_{\tilde{x}} + \left(\overline{\sigma}\hat{v}\right)_{\tilde{y}} + \left(\overline{\sigma}\hat{\varpi}\right)_{\tilde{b}} = 0, \qquad (2.62)$$

where $\boldsymbol{E}^u$, $\boldsymbol{E}^v$ are the components of horizontal Eliassen-Palm (E-P) stress tensor:

$$\boldsymbol{E}^u \overset{def}{=} \boldsymbol{J}^u + \frac{1}{2}\overline{\sigma}^{-1}\overline{\zeta'^2}\,\overline{\boldsymbol{e}}_1 + \overline{\sigma}^{-1}\overline{\zeta' m'_{\tilde{x}}}\,\overline{\boldsymbol{e}}_3\,, \qquad (2.63)$$

$$\boldsymbol{E}^v \overset{def}{=} \boldsymbol{J}^v + \frac{1}{2}\overline{\sigma}^{-1}\overline{\zeta'^2}\,\overline{\boldsymbol{e}}_2 + \overline{\sigma}^{-1}\overline{\zeta' m'_{\tilde{y}}}\,\overline{\boldsymbol{e}}_3\,. \qquad (2.64)$$

The E-P stress tensor $\boldsymbol{E_P}$ absorbs all the residual eddy flux correlations. The full

E-P stress tensor $\boldsymbol{E_P}$ in the TWA framework is given by Young (2012):

$$\boldsymbol{E_P} = \begin{bmatrix} \widehat{u''^2} + \frac{1}{2}\overline{\sigma}^{-1}\overline{\zeta'^2} & \widehat{u''v''} & 0 \\ \widehat{u''v''} & \widehat{v''^2} + \frac{1}{2}\overline{\sigma}^{-1}\overline{\zeta'^2} & 0 \\ \widehat{u''\varpi''} + \overline{\sigma}^{-1}\overline{\zeta' m'_{\tilde{x}}} & \widehat{v''\varpi''} + \overline{\sigma}^{-1}\overline{\zeta' m'_{\tilde{y}}} & 0 \end{bmatrix}. \tag{2.65}$$

Note that all dynamical quantities embedded in the upper 2×2 matrix of the E-P stress tensor carry the dimensions of energy per unit mass ($\mathrm{m}^2\,\mathrm{s}^{-2}$). Meanwhile, the elements in the third row possess units of $\mathrm{m}^2\,\mathrm{s}^{-4}$. This dimensional discrepancy arises purely because the vertical coordinate $\tilde{b}$ maintains a different physical unit compared to the horizontal axes within the buoyancy coordinate system.

The final objective is to transform the averaged primitive equations in the buoyancy coordinate system back into the Cartesian space, following De Szoeke and Bennett (1993) and Young (2012). When bridging the two coordinate systems, the mean buoyancy surface height maps to $z = \overline{\zeta}(\tilde{x}, \tilde{y}, \tilde{b}, \tilde{t})$, representing depth in Cartesian coordinates. Crucially, this geometric relationship can be inverted to define the continuous buoyancy field in Cartesian space, expressed as $\tilde{b} = b^\sharp\left(x, y, \overline{\zeta}, t\right)$. Here, the superscript $\sharp$ refers to variables evaluated in the averaged Cartesian coordinates, which is consistent with the definition of the vertical residual velocity component $w^\sharp$. Meanwhile, $b^\sharp$ corresponds to the reconstructed buoyancy field, which is dynamically distinct from the standard Eulerian mean $\bar{b}$ because it inherently results from an along-isopycnal average. In summary, the mathematical bridge governing this coordinate transformation is

$$\tilde{b} = b^\sharp\left(x, y, \overline{\zeta}(\tilde{x}, \tilde{y}, \tilde{b}, \tilde{t}), t\right), \tag{2.66}$$

$$z = \overline{\zeta}\left(\tilde{x}, \tilde{y}, b^\sharp(x, y, b, t), \tilde{t}\right). \tag{2.67}$$

Differentiating (2.67) with respect to the Cartesian coordinates (x, y, b, t) yields

$$b_x^\sharp = -\,\overline{\sigma}^{-1}\,\overline{\zeta}_{\tilde{x}}\,, \tag{2.68}$$

$$b_y^\sharp = -\,\overline{\sigma}^{-1}\,\overline{\zeta}_{\tilde{y}}\,, \tag{2.69}$$

$$b_z^\sharp = \overline{\sigma}^{-1}, \tag{2.70}$$

$$b_t^\sharp = -\,\overline{\sigma}^{-1}\,\overline{\zeta}_{\tilde{t}}\,. \tag{2.71}$$

Applying the derivative relations $(2.68 - 2.71)$ to compute the adjusted material derivative of the buoyancy field in Cartesian space, it gives

$$\frac{\mathrm{D}^\sharp b^\sharp}{\mathrm{D}t} = b_t^\sharp + \hat{u} b_x^\sharp + \hat{v} b_y^\sharp + w^\sharp b_z^\sharp = \hat{\varpi}\,, \tag{2.72}$$

confirming that the prognostic buoyancy equation collapses to the adjusted material derivative format when mapped appropriately.By examining (2.72), it becomes apparent that the left-hand variable $b^\sharp$ corresponds physically to the isopycnal-averaged interface height $\overline{\zeta}$, while the forcing term right-hand side $\hat{\varpi}$ is modulated by TWA. Consequently, within the TWA framework, the buoyancy surface height ζ corresponds to its isopycnal mean $\overline{\zeta}$, as opposed to the thickness-weighted height $\hat{\zeta}$.

Furthermore, to reformulate the horizontal pressure gradients, a modified pressure field $p^\sharp$ is introduced (Young, 2012):

$$p^\sharp\,(x, y, z, t) \overset{def}{=} \overline{m} + b^\sharp\, z\,. \tag{2.73}$$

Similar to the demonstration of (2.28) and (2.31), it naturally follows that

$$\overline{m}_{\tilde{x}} = p_x^\sharp\,, \quad p_z^\sharp = b^\sharp\,. \tag{2.74}$$

Ultimately, the thickness-weighted averaged Boussinesq primitive equations take the following form in the Cartesian coordinate system (Young, 2012):

$$\frac{\mathrm{D}^{\sharp}\hat{u}}{\mathrm{D}t} - f\hat{v} + p_x^{\sharp} + \nabla \cdot \boldsymbol{E}^u = \hat{\mathcal{X}}, \tag{2.75}$$

$$\frac{\mathrm{D}^{\sharp}\hat{v}}{\mathrm{D}t} + f\hat{u} + p_y^{\sharp} + \nabla \cdot \boldsymbol{E}^v = \hat{\mathcal{Y}}, \tag{2.76}$$

$$p_z^{\sharp} = b^{\sharp}, \tag{2.77}$$

$$\hat{u}_x + \hat{v}_y + w_z^{\sharp} = 0, \tag{2.78}$$

$$\frac{\mathrm{D}^{\sharp}b^{\sharp}}{\mathrm{D}t} = \hat{\varpi}. \tag{2.79}$$

2.3 Spherical Buoyancy Coordinates

This section outlines the framework of the thickness-weighted average in the spherical buoyancy coordinate system, which is practically adopted in global ocean numerical simulations. The rigorous derivations of the metric tensor, Christoffel symbols, and covariant derivatives for general curvilinear coordinates are standard tensor calculus results, e.g. Aris (2012); Kundu et al. (2024). Therefore, they are omitted here for brevity, and the focus is placed directly on their application to the spherical buoyancy coordinate system.

The orthogonal spherical coordinate system is given by $\{\lambda, \phi, r\}$, where λ is the longitude, ϕ is the latitude and r denotes the radial distance from the centre of the sphere, as illustrated in Figure 2.3. The corresponding unit vectors are $\boldsymbol{\lambda}, \boldsymbol{\phi}, \boldsymbol{r}$, respectively.

In the spherical buoyancy coordinates, the location of a point is given by $\{\tilde{\lambda}, \tilde{\phi}, \tilde{b}\}$, where $\tilde{\lambda}$ is the longitude, $\tilde{\phi}$ is the latitude and $\tilde{b}$ represents the buoyancy coordinate. The superscript tilde distinguishes the non-orthogonal buoyancy coordinate system from the standard orthogonal spherical coordinates.

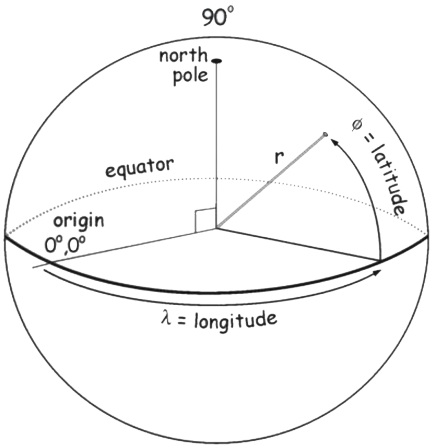


Figure 2.3: The schematic of the orthogonal spherical coordinate system, reproduced from Van Sickle (2017). $0 \leq \lambda \leq 2\pi$ is the longitude, $-\pi/2 \leq \phi \leq \pi/2$ is the latitude and r represents the radial distance measured from the centre of the sphere.

In the spherical buoyancy coordinates, the contravariant basis vectors are

$$\begin{aligned} \boldsymbol{e}^1 &= \nabla\tilde{\lambda} = \frac{1}{r\cos\phi}\,\boldsymbol{\lambda}, \\ \boldsymbol{e}^2 &= \nabla\tilde{\phi} = \frac{1}{r}\,\boldsymbol{\phi}, \\ \boldsymbol{e}^3 &= \nabla\tilde{b} = \frac{1}{r\cos\phi}\frac{\partial b}{\partial\lambda}\,\boldsymbol{\lambda} + \frac{1}{r}\frac{\partial b}{\partial\phi}\,\boldsymbol{\phi} + \frac{\partial b}{\partial r}\,\boldsymbol{r}. \end{aligned} \tag{2.80}$$

The contravariant components of the metric tensor are

$$\{g^{ij}\} = \begin{bmatrix} (r\cos\phi)^{-2} & 0 & (r\cos\phi)^{-2}\,\dfrac{\partial b}{\partial\lambda} \\ 0 & r^{-2} & r^{-2}\,\dfrac{\partial b}{\partial\phi} \\ (r\cos\phi)^{-2}\,\dfrac{\partial b}{\partial\lambda} & r^{-2}\,\dfrac{\partial b}{\partial\phi} & (r\cos\phi)^{-2}\left(\dfrac{\partial b}{\partial\lambda}\right)^2 + r^{-2}\left(\dfrac{\partial b}{\partial\phi}\right)^2 + \left(\dfrac{\partial b}{\partial r}\right)^2 \end{bmatrix}. \tag{2.81}$$

Following the notation in Section 2.1, $\sigma = (\partial b/\partial r)^{-1}$ denotes the isopycnal thickness. As a result, the metric determinant can be written as

$$g = \det\left(g^{ij}\right)^{-1} = \sigma^2 r^4 \cos^2\phi\,. \tag{2.82}$$

The covariant basis vectors are

$$\begin{aligned}
\boldsymbol{e}_1 &= \sqrt{g}\,\boldsymbol{e}^2 \times \boldsymbol{e}^3 = r\cos\phi\,\boldsymbol{\lambda} - \sigma\frac{\partial b}{\partial \lambda}\,\boldsymbol{r},\\
\boldsymbol{e}_2 &= \sqrt{g}\,\boldsymbol{e}^3 \times \boldsymbol{e}^1 = r\,\boldsymbol{\phi} - \sigma\frac{\partial b}{\partial \phi}\,\boldsymbol{r},\\
\boldsymbol{e}_3 &= \sqrt{g}\,\boldsymbol{e}^1 \times \boldsymbol{e}^2 = \sigma\,\boldsymbol{r}.
\end{aligned} \tag{2.83}$$

Thus, the covariant components of the metric tensor are

$$\{g_{ij}\} = \begin{bmatrix}
(r\cos\phi)^2 + \sigma^2\left(\dfrac{\partial b}{\partial \lambda}\right)^2 & \sigma^2\dfrac{\partial b}{\partial \lambda}\dfrac{\partial b}{\partial \phi} & -\sigma^2\dfrac{\partial b}{\partial \lambda}\\
\sigma^2\dfrac{\partial b}{\partial \lambda}\dfrac{\partial b}{\partial \phi} & r^2 + \sigma^2\left(\dfrac{\partial b}{\partial \phi}\right)^2 & -\sigma^2\dfrac{\partial b}{\partial \phi}\\
-\sigma^2\dfrac{\partial b}{\partial \lambda} & -\sigma^2\dfrac{\partial b}{\partial \phi} & \sigma^2
\end{bmatrix}. \tag{2.84}$$

Comparing the expression of the contravariant and covariant basis vectors in the standard buoyancy coordinates $\{\tilde{x}, \tilde{y}, \tilde{b}\}$ with those in the spherical buoyancy coordinates $\{\tilde{\lambda}, \tilde{\phi}, \tilde{b}\}$, the distinction primarily lies in the coefficients of the radial distance, i,e, r and $r\cos\phi$. Consequently, transitioning to buoyancy coordinates does not alter the physical interpretation of the horizontal velocity vector components.

For clarity, the velocity vector $\boldsymbol{u}$ in the $\{\tilde{x}, \tilde{y}, \tilde{b}\}$ coordinates can be written as

$$\boldsymbol{u} = u\,\boldsymbol{e}_1 + v\,\boldsymbol{e}_2 + \left(\sigma^{-1}\zeta_{\tilde{t}} + \varpi\right)\boldsymbol{e}_3\,, \tag{2.85}$$

where the horizontal velocity components u and v require no geometric scaling,

matching the Cartesian coordinates exactly.

In contrast, the velocity vector in the spherical buoyancy coordinate system $\{\tilde{\lambda}, \tilde{\phi}, \tilde{b}\}$ takes the form:

$$\boldsymbol{u} = \frac{u}{r\cos\tilde{\phi}}\,\boldsymbol{e}_1 + \frac{v}{r}\,\boldsymbol{e}_2 + \left(\sigma^{-1}\zeta_{\tilde{t}} + \varpi\right)\boldsymbol{e}_3\,, \tag{2.86}$$

where $\zeta = r - r_0$ and r_0 is the constant Earth radius. Here, the velocity components share the exact same scaling coefficients (i.e., $1/(r\cos\tilde{\phi})$ and $1/r$) with the standard spherical coordinates.

This equivalence in physical interpretation explains why the $\{\tilde{x}, \tilde{y}, \tilde{b}\}$ coordinate system is utilised to illustrate the fundamental concepts of the thickness-weighted average framework in Section 2.1. It avoids the geometric complexities of spherical coordinates without losing any physical generality.

2.4 GEOMETRIC Framework for Eddy Parameterisation

The thickness-weighted averaged Boussinesq primitive equations, derived in Section 2.1, provide a cornerstone, as the eddy flux terms are isolated within the horizontal momentum equations. This section introduces the GEOMETRIC framework (Marshall et al., 2012; Mak et al., 2018) for parameterising the eddy stress tensor, subject to constraints imposed by the total eddy energy. The derivations and equations presented below explicitly reproduce the foundational theory established by Marshall et al. (2012). While this presentation focuses on the quasi-geostrophic system for simplicity, these results generalise to the exact thickness-weighted averaged primitive equations (Young, 2012; Maddison and Marshall, 2013).

In the Cartesian coordinate system, the Eliassen-Palm (E-P) stress tensor is defined

by

$$\boldsymbol{E_p} = \begin{bmatrix} -M+P & N & 0 \\ N & M+P & 0 \\ -S & R & 0 \end{bmatrix}, \tag{2.87}$$

where $M = (\overline{v'^2 - u'^2})/2$ and $N = \overline{u'v'}$ denote the eddy Reynolds stresses; $P = \overline{b'^2}/(2\mathcal{N}_0^2)$ is related to the eddy potential energy in the Cartesian coordinates; $R = (f_0/\mathcal{N}_0^2)\,\overline{b'u'}$ and $S = (f_0/\mathcal{N}_0^2)\,\overline{b'v'}$ are the eddy form stresses, which are proportional to the eddy buoyancy fluxes.

Before defining the parameterisation, it is necessary to establish the physical and mathematical bounds on the eddy stress tensor components. By applying the Cauchy-Schwarz inequality to the covariance matrix of the horizontal eddy velocity and buoyancy fluctuations, the cross-terms are fundamentally bounded by the total eddy energy E (comprising eddy kinetic energy and eddy potential energy). As derived by Marshall et al. (2012), this yields the following energetic bound:

$$M^2 + N^2 + P^2 + \frac{\mathcal{N}_0^2}{2f_0^2}\left(R^2 + S^2\right) \leq K^2 + 2KP + P^2 = E^2, \tag{2.88}$$

where $K = (\overline{u'^2 + v'^2})/2$ is the eddy kinetic energy.

With this mathematical preparation established, the eddy stress tensor components can be parameterised using the eddy energy and five bounded, dimensionless coefficients. Following equation [16] in Marshall et al. (2012), we define

$$\begin{gathered} M = -\gamma_m E \cos 2\phi_m \cos^2\lambda,\ N = \gamma_m E \sin 2\phi_m \cos^2\lambda, \\ P = E\sin^2\lambda, \\ R = \gamma_b \frac{f_0}{\mathcal{N}_0} E \cos\phi_b \sin 2\lambda,\ S = \gamma_b \frac{f_0}{\mathcal{N}_0} E \sin\phi_b \sin 2\lambda. \end{gathered} \tag{2.89}$$

The system parameters have direct geometric and physical interpretations (Mar-

shall et al., 2012). For example, $\lambda \in [0, \pi/2]$ partitions the total eddy energy into the kinetic and potential energy, such that $K = E\cos^2\lambda$. The angle $\phi_m \in [0, \pi]$ reflects the relative amplitude and orientation of the eddy Reynolds stresses, while $\gamma_b \in [0, 1]$ and $\phi_b \in [-\pi, \pi]$ characterise the buoyancy flux components. Specifically, $\gamma_m \in [0, 1]$ measures the amplitude of eddy Reynolds stress against the eddy kinetic energy:

$$\gamma_m \overset{def}{=} \frac{\sqrt{M^2 + N^2}}{K} = \frac{L}{K}, \tag{2.90}$$

where $L \overset{def}{=} \sqrt{M^2 + N^2}$ represents the eddy anisotropy. The geometric nature of these parameters is conceptualised through an elliptical horizontal eddy model, where ϕ_m indicates the principal axis orientation and γ_m determines the elliptical eccentricity. Similarly, γ_b and λ describe the structure of a vertically planar elliptical eddy (Waterman and Lilly, 2015).

Furthermore, the GEOMETRIC framework integrates natively with the GM90 thickness diffusivity κ. The GM90 scheme is formulated to parameterise the eddy buoyancy fluxes, corresponding to the last row of the E-P eddy stress tensor in (2.87). Consequently, κ can be explicitly related to the eddy energy:

$$\kappa = \alpha E \frac{\mathcal{N}_0}{\left|\nabla_h \overline{b}\right|}, \tag{2.91}$$

where α is a non-dimensional coefficient defined by γ_b and the associated trigonometric functions, such that its magnitude is bounded by 1 (Marshall et al., 2012).

2.5 Eddy Stress Tensor

Eddy stress tensors have taken various forms during the development of eddy-mean flow interaction theories. In this section, the essential nature and internal connections of eddy stress tensors are explored, based on the theoretical frame-

work established by Maddison and Marshall (2013).

In studies of eddy-mean flow interaction, the traditional method introduces E-P flux components and the eddy interaction terms that explicitly appear only in the momentum equations (Young, 2012). First, the eddy stress tensor in the quasi-geostrophic (QG) case is discussed, followed by the transformations between various tensors. Finally, by retreating from the Boussinesq system to the QG approximation, the equivalence of the E-P flux vectors in Section 2.1 and the eddy stress tensor introduced in Section 2.4 is demonstrated. Tensor analysis and the Einstein summation convention are utilised throughout this section.

The quasi-geostrophic equations are derived by expanding the primitive equations by a small Rossby number:

$$\left(\partial_t + u_g\partial_x + v_g\partial_y\right) u_g - f_0 v_{ag} - \beta y v_g = -\partial_x p_{ag} + F_x\,, \tag{2.92}$$

$$\left(\partial_t + u_g\partial_x + v_g\partial_y\right) v_g + f_0 u_{ag} + \beta y u_g = -\partial_y p_{ag} + F_y\,, \tag{2.93}$$

$$\left(\partial_t + u_g\partial_x + v_g\partial_y\right) b + w_{ag}\mathcal{N}_0^2 = B, \tag{2.94}$$

where $\boldsymbol{u_g}$ and $\boldsymbol{u_{ag}}$ are geostrophic and ageostrophic components of the velocity, respectively:

$$\boldsymbol{u_g} \overset{def}{=} \begin{pmatrix} u_g \\ v_g \\ 0 \end{pmatrix}, \quad \boldsymbol{u_{ag}} \overset{def}{=} \begin{pmatrix} u_{ag} \\ v_{ag} \\ w_{ag} \end{pmatrix}. \tag{2.95}$$

Both geostrophic and ageostrophic velocity are non-divergent:

$$\nabla \cdot \boldsymbol{u_g} = 0,\ \nabla \cdot \boldsymbol{u_{ag}} = 0. \tag{2.96}$$

Following Maddison and Marshall (2013), the quasi-geostrophic equations are rewritten using the vector $\boldsymbol{D}$, whose divergence is associated with the potential

vorticity, and the vector $\boldsymbol{F}$ is arranged accordingly:

$$\boldsymbol{D} \stackrel{def}{=} \begin{pmatrix} v_g \\ -u_g \\ \dfrac{f_0}{\mathcal{N}_0^2} b \end{pmatrix}, \; \boldsymbol{F} \stackrel{def}{=} \begin{pmatrix} F_y \\ -F_x \\ \dfrac{f_0}{\mathcal{N}_0^2} B \end{pmatrix}. \tag{2.97}$$

Therefore, the horizontal momentum equations and the buoyancy equation constitute the quasi-geostrophic dynamical equation:

$$\left(\partial_t + \boldsymbol{u_g} \cdot \nabla\right) \boldsymbol{D} + f_0 \, \boldsymbol{u_{ag}} + \beta y \, \boldsymbol{u_g} = \boldsymbol{k} \times \nabla p_{ag} + \boldsymbol{F} \, . \tag{2.98}$$

The divergence of the vector $\boldsymbol{D}$ yields the quasi-geostrophic potential vorticity (QGPV):

$$q = \nabla \cdot \boldsymbol{D} + \beta y \, . \tag{2.99}$$

Accordingly, taking the divergence of the dynamical equation (2.98), the QGPV equation is obtained:

$$\partial_t q + \nabla \cdot \left(\boldsymbol{u_g} \, q\right) = \nabla \cdot \boldsymbol{F} \, . \tag{2.100}$$

These equations can be conveniently expressed using the Einstein summation convention in general curvilinear coordinates. Note that non-indexed subscripts are enclosed in square brackets to avoid ambiguity; the partial derivative with respect to a coordinate is denoted by a comma preceding the corresponding index, and the covariant derivative with respect to the indexed coordinate is represented by a semicolon.

The dynamical equation becomes

$$\partial_t D^i + \left(\left[u_g\right]^j D^i \right)_{;j} + \left[f_0\right] \left[u_{ag}\right]^i + \left[f_1\right] \left[u_g\right]^i = \varepsilon^{ijk} Z_j \left[p_{ag}\right]_{,k} + F^i, \tag{2.101}$$

where $[f_1] = \beta y$ and Z denotes the components of the vertical unit vector $\boldsymbol{k}$.
The continuity equation and QGPV are given by

$$\left[u_g\right]^i_{;i} = 0, \quad \left[u_{ag}\right]^i_{;i} = 0\,; \tag{2.102}$$

$$q = D^i_{;i} + [f_1]\,. \tag{2.103}$$

Applying the averaging operator to the dynamical equation (2.101) yields the averaged form:

$$\partial_t \overline{D^i} + \left(\overline{\left[u_g\right]^j}\,\overline{D^i}\right)_{;j} + [f_0]\,\overline{\left[u_{ag}\right]^i} + [f_1]\,\overline{\left[u_g\right]^i} = \varepsilon^{ijk} Z_j \overline{\left(p_{ag}\right)}_{,k} + \overline{F^i} - T^{ij}_{;j}\,, \tag{2.104}$$

where the eddy flux tensor is defined by

$$T^{ij} \overset{def}{=} \overline{\left[u_g\right]^{j'} D^{i'}}\,. \tag{2.105}$$

The averaged QGPV equation is

$$\partial_t \overline{q} + \left(\overline{\left[u_g\right]^i}\,\overline{q}\right)_{;i} = \overline{F^i_{;i}} - T^{ij}_{;ij}\,. \tag{2.106}$$

In Cartesian coordinates, the eddy flux tensor T^{ij} has the following components (Maddison and Marshall, 2013):

$$T^j_i = g_{is} T^{sj} = \begin{bmatrix} N & M-K & R \\ M+K & -N & S \\ 0 & 0 & 0 \end{bmatrix}, \tag{2.107}$$

where the contravariant index determines the row, and M, N, K, R, S share the similar definition as (2.87), if the perturbed velocity is substituted with $\left(u'_g, v'_g\right)$.

Because the double divergence of eddy flux tensor $T^{ij}_{;ij}$ controls the QGPV evo-

lution, the divergence of the tensor, i.e. $T^{ij}_{;j}$, takes the form of the eddy QGPV flux plus an arbitrary rotational term (Maddison and Marshall, 2013). Specifically, the averaged QGPV equation (2.106) is not influenced by adding any antisymmetric tensor to T^{ij}:

$$[T^*]^{ij} = T^{ij} + A^{ij} \,, \tag{2.108}$$

where A^{ij} is the antisymmetric and non-divergent tensor, i.e. $A^{ij} = -A^{ji}$. Such a transformation does not affect the double divergence of eddy flux tensor and thus conserves QGPV. However, the dynamical equation is vulnerable to this transformation due to the introduction of an additional rotational term. Thus, the residual mean ageostrophic velocity can be defined by

$$\left[u^*_{ag}\right]^i \overset{def}{=} \overline{\left[u_{ag}\right]^i} - \frac{1}{[f_0]} A^{ij}_{;j} \,. \tag{2.109}$$

The averaged dynamical equation then becomes

$$\partial_t \overline{D^i} + \left(\overline{\left[u_g\right]^j}\,\overline{D^i}\right)_{;j} + [f_0]\,\overline{\left[u^*_{ag}\right]^i} + [f_1]\,\overline{\left[u_g\right]^i} = \varepsilon^{ijk} Z_j \overline{\left(p_{ag}\right)}_{,k} + \overline{F^i} - [T^*]^{ij}_{;j} \,. \tag{2.110}$$

Normally the eddy terms affect all three components in the dynamical equation including momentum and buoyancy equations. But if A^{ij} is chosen properly such that $[T^*]^{ij}\, Z_i = 0$, the eddy flux will not appear explicitly in the buoyancy equation(Maddison and Marshall, 2013). For example, selecting

$$A^{ij} = T^{ji} - T^{ij} \tag{2.111}$$

gives rise to the residual-mean eddy stress tensor:

$$[T^*_R]^{ij} = T^{ji} = \overline{\left[u_g\right]^{i'} D^{j'}} \,,$$

whose components in the Cartesian coordinate system are

$$[T_R^*]_i^j = g_{is}\,[T_R^*]^{sj} = \begin{bmatrix} N & M+K & 0 \\ M-K & -N & 0 \\ R & S & 0 \end{bmatrix}. \tag{2.112}$$

Applying the cross product of $\boldsymbol{k}$ to the dynamical equation (2.110) with the choice of A^{ij} (2.111) yields the horizontal momentum equations. Focusing on the momentum equations as the buoyancy equation no longer contains any eddy terms, the result simplifies directly to (Maddison and Marshall, 2013):

$$\partial_t \overline{\left[u_g\right]^i} + \left(\overline{\left[u_g\right]^j \left[u_g\right]^i}\right)_{;j} - [f_0]\,\varepsilon^{ijk}\,\left[u_{ag}^*\right]_j\,Z_k - [f_1]\,\varepsilon^{ijk}\overline{\left[u_g\right]}_j\,Z_k = -h^{ij}\,\overline{\left[p_{ag}\right]}_{,j} + \overline{F^i} - [E_R]^{ij}_{;j}\ , \tag{2.113}$$

where $h^{ij} = g^{ij} - Z^i Z^j$ and $[E_R]^{ij}$ is the Eliassen-Palm flux tensor:

$$[E_R]^{ij} \overset{def}{=} \boldsymbol{k} \times \tilde{\boldsymbol{T}}_R = -\varepsilon^{iks}\,[T_R^*]_k^j\,Z_s\,. \tag{2.114}$$

In the Cartesian coordinates, the residual-mean E-P tensor has the form:

$$[E_R^*]_i^j = g_{is}\,[E_R^*]^{sj} = \begin{bmatrix} -M-K & N & 0 \\ N & M-K & 0 \\ -S & R & 0 \end{bmatrix}. \tag{2.115}$$

It is now possible to associate the E-P tensor in the thickness-weighted average framework (2.65) with the QGPV eddy stress tensor (2.87) used for the geometric decomposition in Section 2.4, following Maddison and Marshall (2013). In the Boussinesq system, the E-P components constitute the E-P eddy stress tensor

(2.65):

$$E^{ij} = \begin{bmatrix} \widehat{u''^2} + \frac{1}{2}\overline{\sigma}^{-1}\overline{\zeta'^2} & \widehat{u''v''} & 0 \\ \widehat{u''v''} & \widehat{v''^2} + \frac{1}{2}\overline{\sigma}^{-1}\overline{\zeta'^2} & 0 \\ \widehat{u''\varpi''} + \overline{\sigma}^{-1}\overline{\zeta' m'_{\tilde{x}}} & \widehat{v''\varpi''} + \overline{\sigma}^{-1}\overline{\zeta' m'_{\tilde{y}}} & 0 \end{bmatrix}. \tag{2.116}$$

This form relates with the GEOMETRIC E-P eddy stress tensor (2.87) through the QGPV conserved transformation introduced above. By choosing A^{ij} to be

$$A^{ij} = \begin{bmatrix} 0 & \frac{\widehat{u''^2} + \widehat{v''^2}}{2} & 0 \\ -\frac{\widehat{u''^2} + \widehat{v''^2}}{2} & 0 & 0 \\ 0 & 0 & 0 \end{bmatrix}, \tag{2.117}$$

the TWA E-P tensor can be transformed to

$$E^{ij} = \begin{bmatrix} \frac{\widehat{u''^2} - \widehat{v''^2}}{2} + \frac{1}{2}\overline{\sigma}^{-1}\overline{\zeta'^2} & \widehat{u''v''} & 0 \\ \widehat{u''v''} & \frac{\widehat{v''^2} - \widehat{u''^2}}{2} + \frac{1}{2}\overline{\sigma}^{-1}\overline{\zeta'^2} & 0 \\ \widehat{u''\varpi''} + \overline{\sigma}^{-1}\overline{\zeta' m'_{\tilde{x}}} & \widehat{v''\varpi''} + \overline{\sigma}^{-1}\overline{\zeta' m'_{\tilde{y}}} & 0 \end{bmatrix}. \tag{2.118}$$

Under the geostrophic limit $p_x = m_{\tilde{x}} = f_0 v,\ p_y = m_{\tilde{y}} = -f_0 u$, together with the relation $b' = -\mathcal{N}_0^2 \zeta'$ and neglecting diapycnal processes, the E-P eddy stress tensor in the quasi-geostrophic regime can be estimated as

$$E^{ij} = \begin{bmatrix} \frac{\widehat{u''^2} - \widehat{v''^2}}{2} + \frac{\overline{b'^2}}{2\mathcal{N}_0^2} & \widehat{u''v''} & 0 \\ \widehat{u''v''} & \frac{\widehat{v''^2} - \widehat{u''^2}}{2} + \frac{\overline{b'^2}}{2\mathcal{N}_0^2} & 0 \\ -\frac{f_0}{\mathcal{N}_0^2}\overline{v'b'} & \frac{f_0}{\mathcal{N}_0^2}\overline{u'b'} & 0 \end{bmatrix}. \tag{2.119}$$

Note that in quasi-geostrophic system, the background buoyancy is strictly a function of depth, $b = b(z)$, which implies that there is no analytical difference between averaging along the density surfaces and along constant depths in the quasi-geostrophic limit. For this reason, the thickness-weighted averaged E-P tensor (2.65) directly maps to the E-P tensor (2.87) in the Cartesian coordinate system.

2.6 Summary

In Chapter 2, the foundational framework of the thickness-weighted average (TWA) has been reviewed. The Boussinesq primitive equations were first expressed in the buoyancy coordinates, and three distinct averaging operators were distinguished. Following Young (2012), the Boussinesq primitive equations with TWA were presented, demonstrating that all eddy components naturally appear within the Eliassen-Palm (E-P) stress tensor. To bridge the theoretical framework with practical global ocean modelling, these mathematical formulations were then directly applied to the spherical buoyancy coordinate system. Furthermore, this chapter reviewed the theory of the GEOMETRIC parameterisation (Marshall et al., 2012), which is rigorously constrained by the total eddy energy. This highlights the critical importance of understanding and quantifying the total eddy energy, setting the primary objective for the subsequent chapters. Finally, various forms of the E-P stress tensor and their interconnections were discussed based on Maddison and Marshall (2013), establishing a complete and consistent theoretical basis for the remainder of the thesis.

Chapter 3

Eddy Energy Definition

This chapter defines the eddy kinetic energy and eddy potential energy, and discusses their justification in Section 3.1. For the GEOMETRIC eddy parameterisation introduced in Section 2.4, the eddy energy constraint acts as a crucial cornerstone. Section 3.2 explores whether the thickness-weighted averaged form of the E-P eddy stress tensor could still be bounded by the total eddy energy. While the derivation of kinetic energy naturally builds upon existing literature, the formulation of potential energy introduces a deliberate methodological choice to ensure non-negativity, distinguishing it from approaches that allow non-positive-definite energy metrics. The distinction between established theoretical results and these specific analytical choices will be explicitly highlighted.

3.1 Eddy Energy under the Framework of thickness-weighted Average

The kinetic energy density (KE) is defined using the Boussinesq reference density as $\rho_0 \boldsymbol{u} \cdot \boldsymbol{u}/2$. On the application of the thickness-weighted average, the mean kinetic energy (MKE) and eddy kinetic energy (EKE) are naturally defined. Neglecting

the vertical velocity contributions to kinetic energy, this is approximated as

$$\widehat{\mathrm{KE}} \approx \frac{1}{2}\rho_0\, \widehat{\boldsymbol{u}_{\boldsymbol{h}}} \cdot \widehat{\boldsymbol{u}_{\boldsymbol{h}}} + \frac{1}{2}\rho_0\, \widehat{\boldsymbol{u}_{\boldsymbol{h}}'' \cdot \boldsymbol{u}_{\boldsymbol{h}}''}\,, \tag{3.1}$$

$$\mathrm{MKE} \overset{def}{=} \frac{1}{2}\rho_0\, \widehat{\boldsymbol{u}_{\boldsymbol{h}}} \cdot \widehat{\boldsymbol{u}_{\boldsymbol{h}}} = \frac{1}{2}\rho_0 \left(\hat{u}^2 + \hat{v}^2\right)\,, \tag{3.2}$$

$$\mathrm{EKE} \overset{def}{=} \frac{1}{2}\rho_0\, \widehat{\boldsymbol{u}_{\boldsymbol{h}}'' \cdot \boldsymbol{u}_{\boldsymbol{h}}''} = \frac{1}{2}\rho_0 \left(\widehat{u''^2} + \widehat{v''^2}\right)\,. \tag{3.3}$$

On the other hand, defining the potential energy within the TWA framework presents a recognised theoretical challenge. The potential energy density (PE) is $\rho g z$ in the Cartesian coordinate system, which is expressed as $-\rho_0 \tilde{b}\zeta + \rho_0 g\zeta$ in the buoyancy coordinates. The term $-\rho_0 \tilde{b}\zeta$ represents the potential energy density of the fluid minus that of the basic state, given by

$$-\rho_0 \tilde{b}\zeta = gz\left(\rho - \rho_0\right). \tag{3.4}$$

As concluded in Section 2.2, the averaged isopycnal height is reflected by $\overline{\zeta}$ instead of $\hat{\zeta}$ in the framework of thickness-weighted average. Thus, the mean potential energy (MPE) in the buoyancy coordinate system is defined as

$$\mathrm{MPE} \overset{def}{=} \rho_0 \left(-\tilde{b} + g\right)\overline{\zeta}\,. \tag{3.5}$$

Considering ζ' as a small displacement of a fluid parcel at the buoyancy level $b\left(z\right)$ from the equilibrium state, it can be associated with the buoyancy perturbation b' through a first-order Taylor expansion:

$$\begin{aligned} b' &= b\left(z\right) - b\left(z + \zeta'\right) \approx -\frac{\partial b}{\partial z}\zeta' \\ &= -\mathcal{N}_0^2\, \zeta', \end{aligned} \tag{3.6}$$

which also reveals the relationship between the buoyancy disturbance and the

isopycnal displacement under the Boussinesq approximation. The restoring force due to the displacement of a fluid element is

$$\mathcal{F} = \rho_0 b' = -\rho_0 \mathcal{N}_0^2 \zeta' \,. \tag{3.7}$$

As noted in prior literature, e.g., Aiki and Richards (2008), strict adherence to certain exact definitions of available potential energy in thickness-weighted equations yields a mean or eddy available potential energy that is no longer positive definite. Recent work on localised APE budgets has also emphasised that regional eddy APE definitions should remain connected to a consistent mean/eddy decomposition of APE and its associated energy transfers (Tailleux and Roullet, 2025). In the present TWA setting, the EPE definition is therefore chosen to preserve non-negativity while remaining consistent with the averaging structure of the E-P stress tensor:

$$\mathrm{EPE} \overset{def}{=} \rho_0 \overline{\sigma}^{-1} \frac{\overline{\zeta'^2}}{2} \,, \tag{3.8}$$

which is strictly positive under stable stratification, i.e. $\overline{\sigma} > 0$. In Cartesian coordinates, the corresponding EPE takes the standard quasi-geostrophic form:

$$\mathrm{EPE} = \rho_0 \frac{\overline{b'^2}}{2\mathcal{N}_0^2} \,. \tag{3.9}$$

In line with this averaging structure, EKE is defined with the thickness-weighted average, while EPE is written explicitly under the isopycnal average. This arrangement may seem counter-intuitive at first glance, but it is determined by the unique status of z and $\tilde{b}$ as the vertical coordinates in the TWA framework. Furthermore, such a property aligns with the thickness-weighted averaged form of the E-P eddy form stress tensor introduced in (2.65), where the EPE terms appear under the isopycnal average. This relationship will be discussed further in Section 3.2.

3.2 Eddy Energy Constraint on the Eliassen-Palm Stress Tensor

The GEOMETRIC parameterisation is proposed by Marshall et al. (2012) for the Eliassen-Palm stress tensor in the quasi-geostrophic (QG) system under the Eulerian average. The components of the tensor are bounded by the total eddy energy, which forms a solid theoretical foundation for the GEOMETRIC parameterisation. Clarifying the contribution of this thesis, this section demonstrates that an analogous eddy energy constraint on the E-P eddy stress tensor can be formulated under the thickness-weighted average framework. Although an exact bound for the full primitive equations is not found, establishing this constraint in the low Rossby number limit provides a more direct link to QG theory and offers a theoretical direction for further empirical testing.

To begin with, the E-P tensor under the TWA framework in (2.118) is revisited, assuming an adiabatic process:

$$\text{TWA}: \ \boldsymbol{E_p} = \begin{bmatrix} \dfrac{\widehat{u''^2} - \widehat{v''^2}}{2} + \dfrac{1}{2}\overline{\sigma}^{-1}\overline{\zeta'^2} & \widehat{u''v''} & 0 \\ \widehat{u''v''} & \dfrac{\widehat{v''^2} - \widehat{u''^2}}{2} + \dfrac{1}{2}\overline{\sigma}^{-1}\overline{\zeta'^2} & 0 \\ \overline{\sigma}^{-1}\overline{\zeta' m'_{\tilde{x}}} & \overline{\sigma}^{-1}\overline{\zeta' m'_{\tilde{y}}} & 0 \end{bmatrix}. \tag{3.10}$$

With reference to the E-P eddy stress tensor for the quasi-geostrophic flow in (2.87), a similar notation can be applied to the E-P tensor (3.10) in the buoyancy coordinate system using the calligraphic alphabet, which leads to

$$\text{TWA}: \ \boldsymbol{E_p} = \begin{bmatrix} -\mathcal{M} + \mathcal{P} & \mathcal{N} & 0 \\ \mathcal{N} & \mathcal{M} + \mathcal{P} & 0 \\ -\mathcal{S} & \mathcal{R} & 0 \end{bmatrix}, \tag{3.11}$$

where $\mathcal{M} = (\widehat{v''^2} - \widehat{u''^2})/2$ and $\mathcal{N} = \widehat{u''v''}$ denote the eddy Reynolds stresses; $\mathcal{P} = \overline{\sigma}^{-1}\overline{\zeta'^2}/2$ represents the eddy potential energy per mass; $\mathcal{R} = \overline{\sigma}^{-1}\overline{\zeta' m'_{\tilde{y}}}$ and $\mathcal{S} = -\overline{\sigma}^{-1}\overline{\zeta' m'_{\tilde{x}}}$ are the eddy form stresses.

Note that the average operator applied in (2.87) is the Eulerian average along constant depth in the Cartesian coordinates, while the overline in (3.10) represents the average along isopycnals in the buoyancy coordinates. Furthermore, the components in (2.87) can be generalised to the E-P stress tensor shown in (3.10) under the thickness-weighted averaged framework as discussed in Section 2.5. The main reason for this discrepancy is that the buoyancy profile only depends on the depth at the leading order in the QG system and thus does not distinguish between the Eulerian average and the isopycnal average.

In order to study the eddy energy constraint on the E-P stress tensor in the buoyancy coordinate system, the analysis focuses on the energetic bounds of the tensor components under the TWA framework.

In the first place, the eddy Reynolds stress components $\mathcal{M}$ and $\mathcal{N}$ are fundamentally constrained by the eddy kinetic energy per unit mass, $\mathcal{K} = (\widehat{u''^2} + \widehat{v''^2})/2$. Since this relationship stems from the geometric properties of the velocity covariance, it remains robust under various averaging operators, namely

$$\mathcal{M}^2 + \mathcal{N}^2 \leq \mathcal{K}^2. \tag{3.12}$$

Next, to constrain the eddy form stresses $\mathcal{R}$ and $\mathcal{S}$, the geostrophic approximation is applied in the limit of a low Rossby number. According to the thickness-weighted averaged momentum equations (2.59) and (2.60), the fluctuations of the Montgomery potential gradient are related to the eddy velocity as $m'_{\tilde{x}} \approx fv''$ and $m'_{\tilde{y}} \approx -fu''$. Consequently, the eddy form stress components in (3.10) can be sim-

plified to

$$\overline{\zeta' m'_{\tilde{x}}} \approx f\,\overline{\zeta' v''},\ \ \overline{\zeta' m'_{\tilde{y}}} \approx -f\,\overline{\zeta' u''}\,. \tag{3.13}$$

By applying the Cauchy-Schwarz inequality to the covariance terms in (3.13), we can establish the energetic bounds for the eddy form stresses. Introducing the layer thickness σ as a weighting factor allows the inequality to be formulated without requiring an initial approximation on the velocity variance. The squared covariance is bounded by

$$\overline{\zeta' u''}^2 \leq \overline{\sigma u''^2} \cdot \overline{\sigma^{-1}\zeta'^2}. \tag{3.14}$$

This strict inequality is demonstrated with reference to the adjusted form of the Cauchy-Schwarz inequality,

$$\left(\sum_{i=1}^{N} A_i B_i\right)^2 \leq \left(\sum_{i=1}^{N} \lambda_i^2 A_i^2\right)\left(\sum_{i=1}^{N} \frac{B_i^2}{\lambda_i^2}\right),\ \ \lambda_i \neq 0\,, \tag{3.15}$$

by setting $A = u''$, $B = \zeta'$, and the weighting parameter $\lambda = \sqrt{\sigma}$.

According to the mathematical definition of the thickness-weighted average, the first term on the right-hand side of (3.14) is exact: $\overline{\sigma u''^2} = \overline{\sigma}\widehat{u''^2}$. However, interpreting the second term in the context of the E-P tensor requires connecting it to the eddy potential energy $\mathcal{P} = \overline{\sigma}^{-1}\overline{\zeta'^2}/2$. Under the assumption of small layer thickness perturbations ($\sigma \approx \overline{\sigma}$), the inverse thickness can be decoupled from the average, such that $\overline{\sigma^{-1}\zeta'^2} \approx \overline{\sigma}^{-1}\overline{\zeta'^2} = 2\mathcal{P}$. Alternatively, as discussed in the QG scaling, this term can be estimated via the eddy buoyancy flux as $\overline{\sigma^{-1}\zeta'^2} \approx -\overline{b'\zeta'}$. Substituting the exact TWA relation and the EPE approximation into (3.14) yields

$$\frac{\overline{\sigma}}{2f^2}\left(\mathcal{R}^2 + \mathcal{S}^2\right) \leq 2\,\frac{\widehat{u''^2} + \widehat{v''^2}}{2} \cdot \left(-\overline{b'\zeta'}\right) = 2\,\mathcal{K}\mathcal{P}. \tag{3.16}$$

Finally, by combining the Reynolds stress bound (3.12) and the form stress bound

(3.16), the comprehensive energetic constraint is obtained:

$$\mathcal{M}^2 + \mathcal{N}^2 + \mathcal{P}^2 + \frac{\overline{\sigma}}{2f^2}\left(\mathcal{R}^2 + \mathcal{S}^2\right) \leq \mathcal{K}^2 + \mathcal{P}^2 + 2\,\mathcal{K}\mathcal{P} = \mathcal{E}^2, \tag{3.17}$$

where $\mathcal{E} = \mathcal{K} + \mathcal{P}$ denotes the total eddy energy per mass. Therefore, in analogy to (2.88), inequality (3.17) is an asymptotic constraint on the E-P eddy stress tensor under the TWA framework, providing a solid theoretical foundation for the GEOMETRIC parameterisation in the framework of thickness-weighted average in the limit of low Rossby number. A similar result is anticipated in Section 3.4 of Maddison and Marshall (2013), but not derived in detail.

3.3 Summary

In Chapter 3, the eddy kinetic energy and eddy potential energy under the TWA framework have been formally defined. It is concluded that defining EKE under the TWA operator and EPE under the isopycnal average operator stems from the nature of the coordinate transformation and ensures consistency with the expression of the E-P stress tensor. Moreover, upon application of the Cauchy-Schwarz inequality, it is found that EKE and EPE combine to form an energy bound for the E-P stress tensor at a low Rossby number. This implies a possible theoretical routine for extending the GEOMETRIC eddy parameterisation to the TWA framework.

Chapter 4

Eddy Energy Cycle

This chapter derives the eddy kinetic energy (EKE) and eddy potential energy (EPE) equations in Section 4.1 and Section 4.2, respectively. The derivations of both energy equations are presented using two distinct approaches. The first approach explicitly demonstrates the Reynolds decomposition, providing a highly intuitive physical interpretation suitable for diagnostic analysis. The second approach employs a rigorous flux form that naturally aligns with the thickness-weighted average framework. The energy cycle is then discussed from the perspective of mean field and eddy field in Section 4.3 and Section 4.4, respectively.

4.1 Eddy Kinetic Energy Equation

The EKE equations can be formulated using two distinct methods, leading to forms illustrated by (4.1) and (4.2). Presenting both methods is instructive: the first explicitly reveals the energetic sources via Reynolds stresses, while the second directly manipulates the momentum equations for a more concise flux-form derivation.

In the first method, the EKE equation is derived by averaging the total kinetic energy equation and subsequently subtracting the mean kinetic energy equation,

yielding:

$$\text{EKE equ1} \overset{def}{=} \widehat{(\text{mom equ} \cdot \boldsymbol{u_h})} - \widehat{\text{mom equ}} \cdot \hat{\boldsymbol{u}}_{\boldsymbol{h}}. \tag{4.1}$$

Alternatively, after subtracting the averaged momentum equation from the original momentum equation, the dot product of both sides with $\boldsymbol{u_h''}$ gives:

$$\text{EKE equ2} \overset{def}{=} \widehat{[(\text{mom equ} - \widehat{\text{mom equ}}) \cdot \boldsymbol{u_h''}]}. \tag{4.2}$$

The formulae derived from these two methods are fundamentally equivalent. Both methods will be demonstrated, revealing some less obvious results arising from this equivalence at the end of this section.

The eddy kinetic energy is defined as $\rho_0 \, \widehat{\boldsymbol{u_h''} \cdot \boldsymbol{u_h''}}/2$. To keep the formulae concise, the derivations initially consider the eddy kinetic energy per unit mass, i.e. $\widehat{\boldsymbol{u_h''} \cdot \boldsymbol{u_h''}}/2$ and then re-insert ρ_0 in the ultimate expression. This treatment is identically applied when deriving the EPE equation in Section 4.2.

The kinetic energy equation is first derived by taking the dot product of the momentum equations $(2.29 - 2.30)$ with $\boldsymbol{u_h}$:

$$\frac{\mathrm{D}}{\mathrm{D}t}\left(\frac{\boldsymbol{u_h} \cdot \boldsymbol{u_h}}{2}\right) + u\, m_{\tilde{x}} + v\, m_{\tilde{y}} = \boldsymbol{u_h} \cdot \boldsymbol{F_h}\,, \tag{4.3}$$

where $\boldsymbol{F_h} = \mathcal{X}\boldsymbol{i} + \mathcal{Y}\boldsymbol{j}$ is the body force.
Applying the thickness-weighted average yields

$$\frac{\mathrm{D}^\sharp}{\mathrm{D}t}\left(\frac{\widehat{\boldsymbol{u_h} \cdot \boldsymbol{u_h}}}{2}\right) + \nabla \cdot \boldsymbol{J}^{\frac{\boldsymbol{u_h} \cdot \boldsymbol{u_h}}{2}} + \widehat{u\, m_{\tilde{x}}} + \widehat{v\, m_{\tilde{y}}} = \widehat{\boldsymbol{u_h} \cdot \boldsymbol{F_h}}\,, \tag{4.4}$$

where the eddy-correlation flux $\boldsymbol{J}^\theta$ for a generic scalar θ under the TWA framework is formally defined using the averaged covariant basis vectors in (2.52) and

its divergence defined in (2.53). The averaged momentum equations are

$$\frac{\mathrm{D}^{\sharp}\hat{u}}{\mathrm{D}t} + \nabla \cdot \boldsymbol{J}^{u} - f\hat{v} + \widehat{m_{\tilde{x}}} = \hat{\mathcal{X}}, \tag{4.5}$$

$$\frac{\mathrm{D}^{\sharp}\hat{v}}{\mathrm{D}t} + \nabla \cdot \boldsymbol{J}^{v} + f\hat{u} + \widehat{m_{\tilde{y}}} = \hat{\mathcal{Y}}. \tag{4.6}$$

Then, applying the dot product of the averaged momentum equations $(4.5 - 4.6)$ and the averaged velocity $\hat{\boldsymbol{u}}_{\boldsymbol{h}}$ produces an equation for the mean kinetic energy (MKE):

$$\frac{\mathrm{D}^{\sharp}}{\mathrm{D}t}\left(\frac{\widehat{\boldsymbol{u}}_{\boldsymbol{h}} \cdot \widehat{\boldsymbol{u}}_{\boldsymbol{h}}}{2}\right) + \hat{u}\,\nabla \cdot \boldsymbol{J}^{u} + \hat{v}\,\nabla \cdot \boldsymbol{J}^{v} + \hat{u}\,\widehat{m_{\tilde{x}}} + \hat{v}\,\widehat{m_{\tilde{y}}} = \widehat{\boldsymbol{u}}_{\boldsymbol{h}} \cdot \widehat{\boldsymbol{F}}_{\boldsymbol{h}}\,. \tag{4.7}$$

Subtracting (4.7) from (4.4), the EKE equation is obtained:

$$\frac{1}{\rho_0}\frac{\mathrm{D}^{\sharp}}{\mathrm{D}t}\left(\mathrm{EKE}\right) + \nabla \cdot \boldsymbol{J}^{\frac{\boldsymbol{u}_{\boldsymbol{h}} \cdot \boldsymbol{u}_{\boldsymbol{h}}}{2}} - \left(\hat{u}\,\nabla \cdot \boldsymbol{J}^{u} + \hat{v}\,\nabla \cdot \boldsymbol{J}^{v}\right) + \widehat{u'' m''_{\tilde{x}}} + \widehat{v'' m''_{\tilde{y}}} = \widehat{\boldsymbol{u}''_{\boldsymbol{h}} \cdot \boldsymbol{F}''_{\boldsymbol{h}}}\,. \tag{4.8}$$

It is worth pointing out that $\nabla \cdot \boldsymbol{J}^{u}$ and $\nabla \cdot \boldsymbol{J}^{v}$ represent the Reynold stresses as seen in the thickness-weighted averaged eddy stress tensor (2.65), and the corresponding terms contribute to the eddy energy source, which will be detailed in the subsequent sections. The corresponding volume-integrated EKE budget is given by Aiki and Richards (2008, Appendix A, equation (A19)); equation (4.8) gives the local EKE budget including external forcing.

Alternatively, the eddy kinetic energy equation can be derived via the second method illustrated by (4.2), yielding a result identical to (4.8). Reviewing the material derivative (2.22) in buoyancy coordinates, it is evident that ϖ acts as a velocity penetrating the isopycnals. Accordingly, the three-dimensional velocity $\boldsymbol{U}$ under the covariant basis (2.37) in the buoyancy coordinates can be defined as

$$\boldsymbol{U} \overset{def}{=} u\,\boldsymbol{e}_1 + v\,\boldsymbol{e}_2 + \varpi\,\boldsymbol{e}_3\,, \tag{4.9}$$

so that the material derivative simplifies to

$$\begin{aligned}\frac{\mathrm{D}\theta}{\mathrm{D}t} &= \theta_{\tilde{t}} + u\theta_{\tilde{x}} + v\theta_{\tilde{y}} + \varpi\theta_{\tilde{b}} \\ &= \theta_{\tilde{t}} + \boldsymbol{U}\cdot\nabla\,\theta\,.\end{aligned} \tag{4.10}$$

In the averaged buoyancy coordinate system, $\widehat{\boldsymbol{U}}$ is naturally expressed as

$$\widehat{\boldsymbol{U}} = \hat{u}\,\overline{\boldsymbol{e}}_1 + \hat{v}\,\overline{\boldsymbol{e}}_2 + \hat{\varpi}\,\overline{\boldsymbol{e}}_3\,, \tag{4.11}$$

and the averaged thickness equation (2.45) becomes

$$\overline{\sigma}_{\tilde{t}} + \overline{\sigma}\,\nabla\cdot\widehat{\boldsymbol{U}} = 0. \tag{4.12}$$

Assuming a steady mean state, i.e. $\overline{\sigma}$ is constant in time, $\widehat{\boldsymbol{U}}$ becomes non-divergent.

The original material derivative can be decomposed into the mean and fluctuating components:

$$\frac{\mathrm{D}\theta}{\mathrm{D}t} = \frac{\partial}{\partial\tilde{t}}\left(\hat{\theta}+\theta''\right) + \left(\widehat{\boldsymbol{U}}+\boldsymbol{U''}\right)\cdot\nabla\left(\hat{\theta}+\theta''\right). \tag{4.13}$$

When subtracting averaged momentum equations $(4.5-4.6)$ from the original momentum equations $(2.29-2.30)$, the following are obtained:

$$\frac{\mathrm{D}u''}{\mathrm{D}t} + \boldsymbol{U''}\cdot\nabla\hat{u} - fv'' + m''_{\tilde{x}} - \nabla\cdot\boldsymbol{J}^u = \mathcal{X}'', \tag{4.14}$$

$$\frac{\mathrm{D}v''}{\mathrm{D}t} + \boldsymbol{U''}\cdot\nabla\hat{v} + fu'' + m''_{\tilde{y}} - \nabla\cdot\boldsymbol{J}^v = \mathcal{Y}''. \tag{4.15}$$

Taking the dot product of $(4.14-4.15)$ with $\boldsymbol{u''_h}$ yields

$$\frac{\mathrm{D}}{\mathrm{D}t}\left(\frac{\boldsymbol{u''_h}\cdot\boldsymbol{u''_h}}{2}\right) + C + u''m''_{\tilde{x}} + v''m''_{\tilde{y}} - (u''\,\nabla\cdot\boldsymbol{J}^u + v''\,\nabla\cdot\boldsymbol{J}^v) = \boldsymbol{u''_h}\cdot\boldsymbol{F''_h}\,, \tag{4.16}$$

where $C \overset{def}{=} \boldsymbol{u_h''} \cdot (\boldsymbol{U''} \cdot \nabla \widehat{\boldsymbol{u}}_{\boldsymbol{h}})$.

Taking the thickness-weighted average, the EKE equation using the second method is derived:

$$\frac{1}{\rho_0}\frac{\mathrm{D}^\sharp}{\mathrm{D}t}(\mathrm{EKE}) + \nabla \cdot \boldsymbol{J}^{\frac{\boldsymbol{u_h''}\cdot\boldsymbol{u_h''}}{2}} + \widehat{C} + \widehat{u''m_{\tilde{x}}''} + \widehat{v''m_{\tilde{y}}''} = \widehat{\boldsymbol{u_h''} \cdot \boldsymbol{F_h''}} \,. \tag{4.17}$$

Inspecting the thickness-weighted averaged form of C, it expands to

$$\begin{aligned} \widehat{C} &= \boldsymbol{J}^u \cdot \nabla \hat{u} + \boldsymbol{J}^v \cdot \nabla \hat{v} \\ &= -\left(\hat{u}\,\nabla \cdot \boldsymbol{J}^u + \hat{v}\,\nabla \cdot \boldsymbol{J}^v\right) + \left(\nabla \cdot \boldsymbol{J}^{u\hat{u}} + \nabla \cdot \boldsymbol{J}^{v\hat{v}}\right). \end{aligned} \tag{4.18}$$

Meanwhile, the second term on the left hand of (4.17) complies with an identity equation:

$$\nabla \cdot \boldsymbol{J}^{\frac{\boldsymbol{u_h''}\cdot\boldsymbol{u_h''}}{2}} = \nabla \cdot \boldsymbol{J}^{\frac{\boldsymbol{u_h}\cdot\boldsymbol{u_h}}{2}} - \left(\nabla \cdot \boldsymbol{J}^{u\hat{u}} + \nabla \cdot \boldsymbol{J}^{v\hat{v}}\right). \tag{4.19}$$

Comparing the results from the two methods above, it is observed that identities (4.18) and (4.19) add up to demonstrate the equivalence of the EKE equations (4.8) and (4.17). The physical meaning of the components in the eddy energy equations will be discussed in the following sections.

As outlined at the start of this section, the derivation of the EKE equations demonstrates the distinct advantages of both approaches. The first method, leading to (4.8), explicitly isolates the Reynolds stresses (such as $\nabla \cdot \boldsymbol{J}^u$ and $\nabla \cdot \boldsymbol{J}^v$) interacting with the mean flow. This formulation provides a highly intuitive physical interpretation, clearly identifying the energy transfer between the mean field and the eddy field via Reynolds stresses. Conversely, the second method, leading to (4.17), relies on the direct manipulation of the momentum equations. By utilising the mathematical identity (4.18), the complex cross-terms $\widehat{C}$ are absorbed into a concise flux-form divergence, which aligns with the exact TWA framework. Ultimately, the demonstrated equivalence of (4.8) and (4.17) unifies the explicit

physical insight of the Reynolds decomposition with the structural conciseness of the flux-form derivation.

4.2 Eddy Potential Energy Equation

In this section, the derivation of the eddy potential energy (EPE) equation is presented. The evolution of EPE can be derived using two distinct methods: via the isopycnal average and via the thickness-weighted average (TWA). The rationale for presenting these two pathways originate from the definition of EPE in Section 3.1. While the definition naturally yields a formulation based on the isopycnal average, the alternative TWA derivation starts from the difference between total and mean potential energy. A related volume-integrated budget for a residual potential-energy definition is given by Aiki and Richards (2008, Appendix A, equation (A17)). In the present formulation, the total-minus-mean residual differs from the chosen non-negative EPE by the additional buoyancy-derivative term in (4.29). The two derivations describe the same underlying potential-energy dynamics in different local budget forms, with distinct practical advantages. Specifically, the EPE equation based on the isopycnal average is typically more convenient for the diagnostic analysis of the eddy energy budget. In contrast, the formulation based on the TWA naturally couples with the eddy stress tensor.

In the first approach involving isopycnal averaging, the flux form of the equation for vertical movement (2.23) is given by:

$$\frac{\mathrm{D}\zeta}{\mathrm{D}t} = \zeta_{\tilde{t}} + \boldsymbol{U} \cdot \nabla\zeta = w. \tag{4.20}$$

Applying the isopycnal average to (4.20) yields

$$\overline{\zeta}_{\tilde{t}} + \overline{\boldsymbol{U}} \cdot \nabla\,\overline{\zeta} + \overline{\boldsymbol{U}' \cdot \nabla\zeta'} = \overline{w}\,. \tag{4.21}$$

The EPE equation can be constructed by subtracting (4.21) from (4.20), multiplying the result by ζ', and applying the isopycnal average:

$$\zeta'_{\tilde{t}} + \overline{\boldsymbol{U}} \cdot \nabla \zeta' + \boldsymbol{U}' \cdot \nabla \overline{\zeta} + \boldsymbol{U}' \cdot \nabla \zeta' - \overline{\boldsymbol{U}' \cdot \nabla \zeta'} = w', \tag{4.22}$$

$$\left(\overline{\frac{\zeta'^2}{2}} \right)_{\tilde{t}} + \overline{\left(\overline{\boldsymbol{U}} + \boldsymbol{U}' \right) \cdot \nabla \frac{\zeta'^2}{2}} + \overline{\zeta' \, \boldsymbol{U}'} \cdot \nabla \overline{\zeta} = \overline{w' \zeta'} \, . \tag{4.23}$$

The velocity field can alternatively be decomposed as $\hat{u} + u''$ instead of $\overline{u} + u'$, so that (4.23) takes the form of

$$\left(\overline{\frac{\zeta'^2}{2}} \right)_{\tilde{t}} + \overline{\left(\widehat{\boldsymbol{U}} + \boldsymbol{U}'' \right) \cdot \nabla \frac{\zeta'^2}{2}} + \overline{\zeta' \, \boldsymbol{U}'} \cdot \nabla \overline{\zeta} = \overline{w' \zeta'} \, . \tag{4.24}$$

From the definition of the eddy potential energy and taking $\overline{\sigma}^{-1}$ into consideration, it follows that

$$\frac{1}{\rho_0} \frac{\partial}{\partial \tilde{t}} \left(\overline{\sigma} \, \mathrm{EPE} \right) + \frac{1}{\rho_0} \widehat{\boldsymbol{U}} \cdot \nabla \left(\overline{\sigma} \, \mathrm{EPE} \right) + \overline{\boldsymbol{U}'' \cdot \nabla \frac{\zeta'^2}{2}} + \overline{\zeta' \, \boldsymbol{U}'} \cdot \nabla \overline{\zeta} = \overline{w' \zeta'} \, . \tag{4.25}$$

Recalling the definition of the adjusted material derivative with the residual velocity (2.48) and the formulation in (2.51)

$$\begin{aligned} \frac{\mathrm{D}^\sharp \theta}{\mathrm{D}t} &= \partial_{\tilde{t}} \theta + \hat{u} \partial_{\tilde{x}} \theta + \hat{v} \partial_{\tilde{y}} \theta + \hat{\varpi} \partial_{\tilde{b}} \theta \\ &= \overline{\sigma}^{-1} \left[(\overline{\sigma} \theta)_{\tilde{t}} + (\overline{\sigma} \hat{u} \theta)_{\tilde{x}} + (\overline{\sigma} \hat{v} \theta)_{\tilde{y}} + (\overline{\sigma} \hat{\varpi} \theta)_{\tilde{b}} \right], \end{aligned} \tag{4.26}$$

the EPE equation is expressed as

$$\frac{1}{\rho_0} \frac{\mathrm{D}^\sharp}{\mathrm{D}t} \left(\mathrm{EPE} \right) - \frac{1}{\rho_0} \left(\hat{u}_{\tilde{x}} + \hat{v}_{\tilde{y}} + \hat{\varpi}_{\tilde{b}} \right) \mathrm{EPE} + \overline{\sigma}^{-1} \overline{\boldsymbol{U}'' \cdot \nabla \frac{\zeta'^2}{2}} + \overline{\sigma}^{-1} \overline{\zeta' \, \boldsymbol{U}'} \cdot \nabla \overline{\zeta} = \overline{\sigma}^{-1} \overline{w' \zeta'} \, . \tag{4.27}$$

The fourth term on the left is proportional to the gradient of the mean potential energy, serving as the eddy energy source provided by the mean state via baroclinic instability. The right hand side offers an intuitive physical interpretation: the

ascent of buoyant fluid parcels (or the descent of dense parcels) coinciding with downward (or upward) isopycnal displacement yields $\overline{w'\zeta'} < 0$. This mechanism represents the conversion of EPE into EKE, consistent with the conservation of mechanical energy. Similar conversion terms in the Cartesian coordinate system have been extensively discussed in the literature, for example Grotjahn (2003) and Zhai and Marshall (2013).

Assuming a steady mean stratification, i.e. $\overline{\sigma}$ is constant in time, an approximate interpretation of the EPE equation can be readily derived from (4.24):

$$\frac{1}{\rho_0}\frac{\partial}{\partial \tilde{t}}\left(\mathrm{EPE}\right) + \overline{\sigma}^{-1}\,\overline{\left(\widehat{\boldsymbol{U}} + \boldsymbol{U}''\right)\cdot\nabla\,\frac{\zeta'^2}{2}} + \overline{\sigma}^{-1}\,\overline{\zeta'\,\boldsymbol{U}'}\cdot\nabla\,\overline{\zeta} = \overline{\sigma}^{-1}\overline{w'\zeta'}\,, \tag{4.28}$$

where the second term on the left hand side roughly represents the advection of EPE by the combined mean and eddy flows.

Meanwhile, examining the total potential energy under the thickness-weighted average provides an alternative pathway towards the EPE equation, using integration by parts:

$$\begin{aligned}
\widehat{\mathrm{PE}} &= \rho_0\left(-\tilde{b}+g\right)\hat{\zeta} = \rho_0\left(-\tilde{b}+g\right)\overline{\zeta} + \rho_0\left(-\tilde{b}+g\right)\frac{\overline{\sigma'\zeta'}}{\overline{\sigma}} \\
&= \mathrm{MPE} + \rho_0\left(-\tilde{b}+g\right)\overline{\sigma}^{-1}\left(\frac{\overline{\zeta'^2}}{2}\right)_{\tilde{b}} \\
&= \mathrm{MPE} + \rho_0\overline{\sigma}^{-1}\frac{\overline{\zeta'^2}}{2} + \rho_0\overline{\sigma}^{-1}\left[\left(-\tilde{b}+g\right)\frac{\overline{\zeta'^2}}{2}\right]_{\tilde{b}}\,.
\end{aligned} \tag{4.29}$$

It is worth pointing out that the third term on the right side of (4.29) does not contribute to the vertically-integrated energy budget when ζ' vanishes at the upper and lower boundaries:

$$\int_{-H}^{0}\rho_0\overline{\sigma}^{-1}\left[\left(-\tilde{b}+g\right)\frac{\overline{\zeta'^2}}{2}\right]_{\tilde{b}}\,\mathrm{d}z = \int_{b_{bottom}}^{b_{top}}\rho_0\overline{\sigma}^{-1}\left[\left(-\tilde{b}+g\right)\frac{\overline{\zeta'^2}}{2}\right]_{\tilde{b}}\,\overline{\sigma}\,\mathrm{d}b = 0\,. \tag{4.30}$$

Therefore, an alternative EPE equation can be obtained by subtracting the budget of mean potential energy (MPE) $\rho_0(-\tilde{b}+g)\overline{\zeta}$ from the budget of the thickness-weighted average of the total potential energy $\rho_0(-\tilde{b}+g)\zeta$. The governing equation of total potential energy is

$$\left(-\tilde{b}+g\right)\frac{\mathrm{D}\zeta}{\mathrm{D}t}=\frac{\mathrm{D}}{\mathrm{D}t}\left[\left(-\tilde{b}+g\right)\zeta\right]+\varpi\zeta=\left(-\tilde{b}+g\right)w\,. \tag{4.31}$$

The following derivation focuses exclusively on terms with the coefficient $-\tilde{b}$, which interact with the differentiation operators; whereas the terms multiplied by the constant g remain unaltered, balance on both sides of (4.31) and are thus omitted for clarity.

Applying the thickness-weighted average to the potential energy equation (4.31) gives rise to

$$\frac{\mathrm{D}^\sharp}{\mathrm{D}t}\left(-\tilde{b}\hat{\zeta}\right)+\nabla\cdot\boldsymbol{J}^{-\tilde{b}\zeta}+\widehat{\varpi\zeta}=-\tilde{b}\hat{w}\,, \tag{4.32}$$

where $\boldsymbol{J}^\theta$ denotes the eddy-correlation flux for an arbitrary scalar θ under the TWA framework, following the definition in (2.52). On the other hand, the MPE equation is

$$-\tilde{b}\frac{\mathrm{D}^\sharp\overline{\zeta}}{\mathrm{D}t}=\frac{\mathrm{D}^\sharp}{\mathrm{D}t}\left(-\tilde{b}\overline{\zeta}\right)+\hat{\varpi}\overline{\zeta}=-\tilde{b}w^\sharp\,. \tag{4.33}$$

Subtracting (4.33) from (4.32) leads to the EPE equation:

$$\frac{1}{\rho_0}\frac{\mathrm{D}^\sharp}{\mathrm{D}t}\left(\mathrm{EPE}\right)+\frac{\mathrm{D}^\sharp}{\mathrm{D}t}\left[\overline{\sigma}^{-1}\left(-\tilde{b}\,\frac{\overline{\zeta'^2}}{2}\right)_{\tilde{b}}\right]+\nabla\cdot\boldsymbol{J}^{-\tilde{b}\zeta}+\widehat{\varpi\zeta}-\hat{\varpi}\overline{\zeta}=-\tilde{b}\left(\hat{w}-w^\sharp\right). \tag{4.34}$$

With the help of the following identities,

$$\nabla\cdot\boldsymbol{J}^{-\tilde{b}\zeta}=-\tilde{b}\,\nabla\cdot\boldsymbol{J}^{\zeta}-\widehat{\varpi''\zeta''} \tag{4.35}$$

and

$$\hat{\zeta} - \overline{\zeta} = \overline{\sigma}^{-1}\,\overline{\sigma'\zeta'} = \overline{\sigma}^{-1}\left(\frac{\overline{\zeta'^2}}{2}\right)_{\tilde{b}} = \frac{1}{\rho_0}\overline{\sigma}^{-1}\left(\overline{\sigma}\,\mathrm{EPE}\right)_{\tilde{b}}\,, \tag{4.36}$$

the EPE equation (4.34) can be simplified to

$$\frac{1}{\rho_0}\frac{\mathrm{D}^\sharp}{\mathrm{D}t}\left(\mathrm{EPE}\right) + \frac{\mathrm{D}^\sharp}{\mathrm{D}t}\left[\overline{\sigma}^{-1}\left(-\tilde{b}\,\frac{\overline{\zeta'^2}}{2}\right)_{\tilde{b}}\right] - \tilde{b}\,\nabla\cdot\boldsymbol{J}^{\zeta} + \frac{1}{\rho_0}\hat{\varpi}\overline{\sigma}^{-1}\left(\overline{\sigma}\,\mathrm{EPE}\right)_{\tilde{b}} = -\tilde{b}\left(\hat{w} - w^\sharp\right). \tag{4.37}$$

Assuming a material conserved buoyancy, i.e. $\varpi = 0$, the EPE equation further simplifies to be

$$\frac{1}{\rho_0}\frac{\mathrm{D}^\sharp}{\mathrm{D}t}\left(\mathrm{EPE}\right) + \frac{\mathrm{D}^\sharp}{\mathrm{D}t}\left[\overline{\sigma}^{-1}\left(-\tilde{b}\,\frac{\overline{\zeta'^2}}{2}\right)_{\tilde{b}}\right] - \tilde{b}\,\nabla\cdot\boldsymbol{J}^{\zeta} = -\tilde{b}\left(\hat{w} - w^\sharp\right). \tag{4.38}$$

On the left hand side of (4.38), there is not only the evolution of the eddy potential energy but also an additional flux term $\overline{\sigma}^{-1}\left(-\tilde{b}\overline{\zeta'^2}/2\right)_{\tilde{b}}$. Although this term has no contribution to the vertical integral over the fluid column, its local magnitude is not negligible compared with EPE, which is demonstrated by the following scale analysis:

$$\rho_0\overline{\sigma}^{-1}\left(-\tilde{b}\,\frac{\overline{\zeta'^2}}{2}\right)_{\tilde{b}} \approx \rho_0\overline{\sigma}^{-1}\frac{O(\overline{\zeta'^2}/2)\cdot\tilde{b}}{\Delta\tilde{b}} \approx \frac{\mathrm{EPE}\cdot\tilde{b}}{\Delta\tilde{b}}\,. \tag{4.39}$$

4.3 Energy Conversion from the Perspective of the Mean Field

The analysis of the mean energy cycle begins with the thickness-weighted averaged horizontal momentum equations derived in Section 2.2. Following Young (2012), the horizontal momentum equations, recalling equations (2.75) and (2.76),

are given by

$$\frac{\mathrm{D}^\sharp \hat{u}}{\mathrm{D}t} - f\hat{v} + p^\sharp_x + \nabla \cdot \boldsymbol{E}^u = \hat{\mathcal{X}}, \tag{4.40}$$

$$\frac{\mathrm{D}^\sharp \hat{v}}{\mathrm{D}t} + f\hat{u} + p^\sharp_y + \nabla \cdot \boldsymbol{E}^v = \hat{\mathcal{Y}}, \tag{4.41}$$

where $p^\sharp$ is the modified pressure field defined as $p^\sharp \equiv \overline{m} + b^\sharp z$ as introduced in (2.73), and $\boldsymbol{E}^u, \boldsymbol{E}^v$ represent the components of the horizontal Eliassen-Palm (E-P) stress tensor. Taking the inner product of the horizontal residual-mean velocity vector $\widehat{\boldsymbol{u}}_{\boldsymbol{h}}$ with equations (4.40) and (4.41) yields the mean kinetic energy (MKE) equation:

$$\frac{\mathrm{D}^\sharp}{\mathrm{D}t}\left(\frac{\widehat{\boldsymbol{u}}_{\boldsymbol{h}} \cdot \widehat{\boldsymbol{u}}_{\boldsymbol{h}}}{2}\right) + \widehat{\boldsymbol{u}}_{\boldsymbol{h}} \cdot \nabla_h p^\sharp + \widehat{\boldsymbol{u}}_{\boldsymbol{h}} \cdot (\nabla \cdot \boldsymbol{E}_{\boldsymbol{P}}) = \widehat{\boldsymbol{u}}_{\boldsymbol{h}} \cdot \widehat{\boldsymbol{F}}_{\boldsymbol{h}}\,, \tag{4.42}$$

where $\widehat{\boldsymbol{F}}_{\boldsymbol{h}} = (\hat{\mathcal{X}}, \hat{\mathcal{Y}})$ represents the averaged horizontal forcing. The corresponding unforced MKE balance is given by Aiki and Richards (2008, Appendix A, equation (A10)), with Reynolds stress and layer-thickness form drag written separately.

By combining the MKE equation (4.42) with the mean potential energy (MPE) equation (4.33), the evolution of the mean mechanical energy is obtained:

$$\frac{\mathrm{D}^\sharp}{\mathrm{D}t}\left(\frac{\widehat{\boldsymbol{u}}_{\boldsymbol{h}} \cdot \widehat{\boldsymbol{u}}_{\boldsymbol{h}}}{2} - \tilde{b}\overline{\zeta}\right) + \widehat{\boldsymbol{u}}_{\boldsymbol{h}} \cdot (\nabla \cdot \boldsymbol{E}_{\boldsymbol{P}}) = -\widehat{\boldsymbol{u}}_{\boldsymbol{h}} \cdot \nabla_h p^\sharp - \tilde{b}w^\sharp + \widehat{\boldsymbol{u}}_{\boldsymbol{h}} \cdot \widehat{\boldsymbol{F}}_{\boldsymbol{h}}\,. \tag{4.43}$$

The first two terms on the right-hand side of (4.43) represent the work done by the mean pressure gradient and the buoyancy flux, respectively. Utilising the hydrostatic relation $p^\sharp_z = \tilde{b}$ and the non-divergence of the 3-D residual-mean velocity $\nabla \cdot \widehat{\boldsymbol{u}} = 0$, these terms can be cast into a concise flux form:

$$\widehat{\boldsymbol{u}}_{\boldsymbol{h}} \cdot \nabla_h p^\sharp + \tilde{b}w^\sharp = \widehat{\boldsymbol{u}} \cdot \nabla\, p^\sharp = \nabla \cdot \left(\widehat{\boldsymbol{u}}\, p^\sharp\right). \tag{4.44}$$

Substituting (4.44) into (4.43) leads to the final form of the mean mechanical energy equation:

$$\frac{\mathrm{D}^\sharp}{\mathrm{D}t}\left(\frac{\widehat{\boldsymbol{u}}_{\boldsymbol{h}}\cdot\widehat{\boldsymbol{u}}_{\boldsymbol{h}}}{2}-\tilde{b}\,\overline{\zeta}\right)+\widehat{\boldsymbol{u}}_{\boldsymbol{h}}\cdot(\nabla\cdot\boldsymbol{E_P})=-\nabla\cdot\left(\widehat{\boldsymbol{u}}\,p^\sharp\right)+\widehat{\boldsymbol{u}}_{\boldsymbol{h}}\cdot\widehat{\boldsymbol{F}}_{\boldsymbol{h}}\,. \tag{4.45}$$

In this formulation, the term $\widehat{\boldsymbol{u}}_{\boldsymbol{h}}\cdot(\nabla\cdot\boldsymbol{E_P})$ acts as a pivotal energy conversion link, representing a sink for mean mechanical energy and a primary source for the eddy energy field, alongside contributions from external forcing.

Aiki and Richards (2008) investigated the MKE budget using a high-resolution $(0.1^\circ\times 0.1^\circ)$ ocean general circulation model (GCM). To interpret the energy pathways, the residual-mean velocity is decomposed into the isopycnal mean and the bolus velocity components, namely $\widehat{\boldsymbol{u}}_{\boldsymbol{h}}=\overline{\boldsymbol{u}}_{\boldsymbol{h}}+\boldsymbol{u}^\star_{\boldsymbol{h}}$. The resulting physical MKE cycle, as illustrated in Figure 4.1 from Aiki et al. (2016), demonstrates how surface wind stress injects kinetic energy into the mean field, which is then redistributed. Wind-driven Ekman pumping steepens the isopycnals, representing a conversion from MKE to MPE. This isopycnal steepening triggers baroclinic instability, and a substantial portion of the mean kinetic energy is transferred to the eddy field via the E-P flux divergence $\widehat{\boldsymbol{u}}_{\boldsymbol{h}}\cdot(\nabla\cdot\boldsymbol{E_P})$.

The diagnostic results from Aiki and Richards (2008) are summarised in Figure 4.2. These panels confirm the mechanism of MKE cycle, showing the spatial distribution of the energy conversion (source to eddies), the bolus velocity work, the isopycnal mean velocity work and the surface wind work. The net number in the top-right corner of each panel represents the globally-integrated contribution of the corresponding term. Note that the study assumes a closed MKE budget; therefore residuals are attributed to the missing processes, such as bottom friction, the Reynolds stress, the eddy viscosity and diabatic processes over the global ocean.

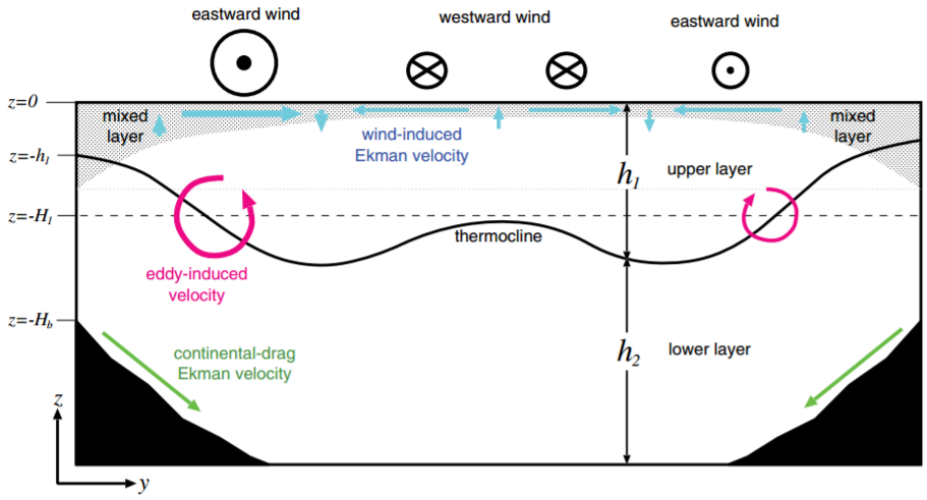


Figure 4.1: Schematic of the meridional ocean section, reproduced from Aiki et al. (2016). The wind-induced Ekman pumping steepens the isopycnals, while the eddy-induced velocity acts to flatten the isopycnals.

4.4 Energy Conversion from the Perspective of the Eddy Field

This section derives the total eddy energy equation to provide a comprehensive understanding of the energy conversion processes from the perspective of the eddy field. The divergence of the Eliassen-Palm (E-P) stress tensor, which contains the Reynold stress, the eddy form stress as well as the EPE term, acts as the primary source for eddy energy. Following the derivation of the EKE equation (4.8), where the Reynolds stress is explicitly identified, the combination of the EKE equation and the EPE equation (4.27) is expected to reveal the emergence of the eddy form stress and the EPE terms. The primary objective of this section is to formulate the total eddy energy equation in a conservative flux form. A related volume-integrated exchange relation is given by Aiki and Richards (2008, Appendix A, equation (A20)).

Substituting the residual-mean velocity $\widehat{u}$ with the non-divergent instanta-

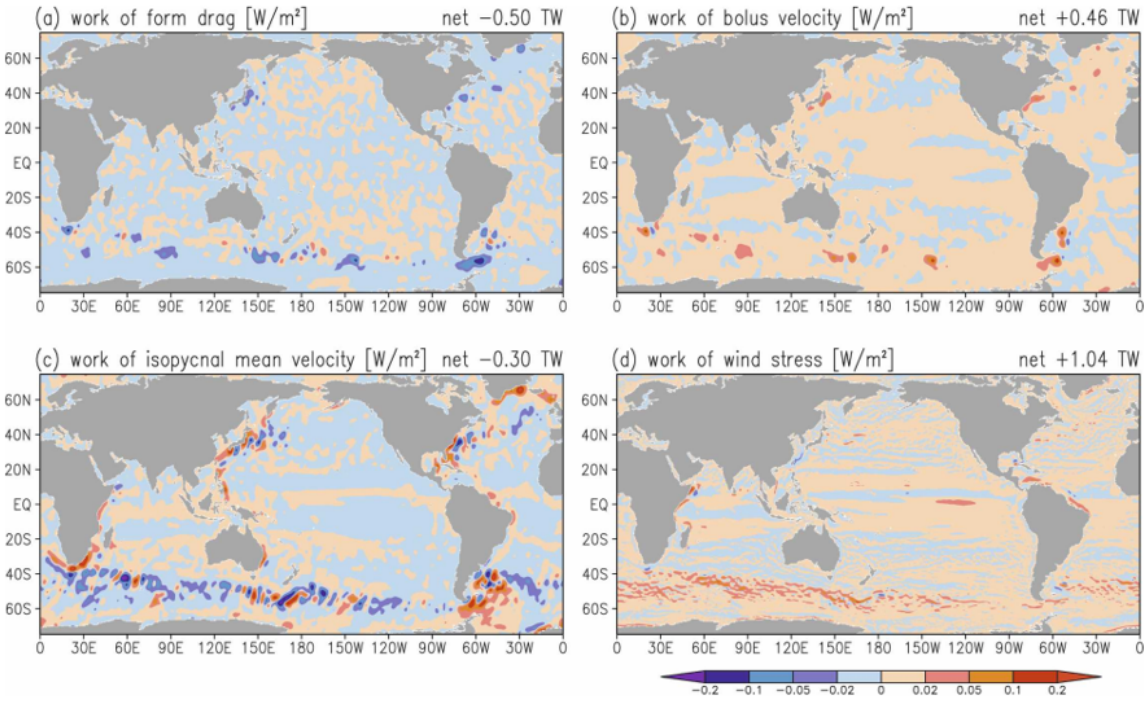


Figure 4.2: Vertically-integrated energy conversion rate diagnosed from a $1/10^{th}$ degree model for the mean kinetic energy budget from Aiki and Richards (2008), including (a) work of form drag, (b) work of bolus velocity $-\boldsymbol{u}_{\boldsymbol{h}}^{\star} \cdot \nabla_h p^{\sharp}$, (c) work of isopycnal velocity $-\overline{\boldsymbol{u}}_{\boldsymbol{h}} \cdot \nabla_h p^{\sharp}$ and (d) work of wind stress $\widehat{\boldsymbol{u}}_{\boldsymbol{h}} \cdot \widehat{\boldsymbol{F}}_{\boldsymbol{h}}$. The colour shading shows local conversion rates in $\mathrm{W\ m^{-2}}$, and the net number at the top-right corner represents the globally-integrated contribution of each term in TW.

neous velocity $\boldsymbol{u}$ in (4.44) reveals that

$$\boldsymbol{u}_{\boldsymbol{h}} \cdot \nabla_h p + \tilde{b} w = \nabla \cdot (\boldsymbol{u} p)\,. \tag{4.46}$$

Applying the thickness-weighted average to (4.46) results in

$$\tilde{b}\hat{w} + \left(\widehat{u'' m''_{\tilde{x}}} + \widehat{v'' m''_{\tilde{y}}}\right) + \left(\hat{u}\,\widehat{m_{\tilde{x}}} + \hat{v}\,\widehat{m_{\tilde{y}}}\right) = \widehat{\nabla \cdot (\boldsymbol{u} p)}\,. \tag{4.47}$$

Utilising the relationship between the TWA and isopycnal-mean Montgomery potentials established in (2.58), the subtraction of the mean pressure work (4.44)

from the averaged total pressure work (4.47) yields the following balance:

$$\tilde{b}\left(\hat{w}-w^{\sharp}\right)+\left(\widehat{u''m''_{\tilde{x}}}+\widehat{v''m''_{\tilde{y}}}\right)+\hat{u}\,\overline{\sigma}^{-1}\left[\left(\frac{1}{2}\overline{\zeta'^{2}}\right)_{\tilde{x}}+\left(\overline{\zeta' m'_{\tilde{x}}}\right)_{\tilde{b}}\right]+$$
$$\hat{v}\,\overline{\sigma}^{-1}\left[\left(\frac{1}{2}\overline{\zeta'^{2}}\right)_{\tilde{y}}+\left(\overline{\zeta' m'_{\tilde{y}}}\right)_{\tilde{b}}\right]=\widehat{\nabla\cdot(\boldsymbol{u}p)}-\nabla\cdot\left(\widehat{\boldsymbol{u}}\,p^{\sharp}\right)\,. \tag{4.48}$$

Under the adiabatic assumption, combining (4.8) with (4.38) and using the pressure-work balance above yields the total eddy energy equation in vector form:

$$\frac{1}{\rho_0}\frac{\mathrm{D}^{\sharp}\mathrm{E}}{\mathrm{D}t}+\frac{\mathrm{D}^{\sharp}}{\mathrm{D}t}\left[\overline{\sigma}^{-1}\left(-\tilde{b}\frac{\overline{\zeta'^{2}}}{2}\right)_{\tilde{b}}\right]+\nabla\cdot\boldsymbol{J}^{-\tilde{b}\zeta}+\nabla\cdot\boldsymbol{J}^{\left(\frac{\boldsymbol{u_h}\cdot\boldsymbol{u_h}}{2}\right)}+$$
$$\widehat{\nabla\cdot(\boldsymbol{u}p)}-\nabla\cdot\left(\widehat{\boldsymbol{u}}\,p^{\sharp}\right)=\widehat{\boldsymbol{u}}_{\boldsymbol{h}}\cdot(\nabla\cdot\boldsymbol{E_P})+\widehat{\boldsymbol{u}''_{\boldsymbol{h}}\cdot\boldsymbol{F}''_{\boldsymbol{h}}}\,, \tag{4.49}$$

where E denotes the total eddy energy density (EKE + EPE). The first term on the left hand side represents the material derivative of the eddy energy, while the second term accounts for the residual EPE component arising from integration by parts. It is crucial to note that all other terms on the left-hand side are expressed as flux divergences, representing the spatial redistribution of energy rather than its generation or dissipation.

4.5 Summary

In Chapter 4, the EKE and EPE equations have been derived using two complementary approaches. The first approach provides a physically intuitive decomposition for diagnostic analysis, while the second utilises the TWA framework to establish the total eddy energy budget in the flux form. The inner product of the residual-mean velocity and the E-P flux divergence serves as the primary energy conversion term between the mean and eddy fields, appearing with opposite signs in their respective budgets (4.45) and (4.49).

Chapter 5

Diagnostic Analysis of Model Results

This chapter presents a diagnostic analysis of an eddy-resolving simulation of the North Atlantic Ocean using the MITgcm. Section 5.1 briefly introduces the MITgcm and outlines the model configuration, following Zhai and Marshall (2013). Next, the eddy energy budget within this simulation is analysed. Following Mak et al. (2022), the depth-integrated eddy energy budget is modelled as

$$\frac{\mathrm{d}}{\mathrm{d}t}E + \nabla \cdot \left(\overline{\boldsymbol{u}}^{z} - |c|\,\boldsymbol{e}_{x}\right) E = \text{Source} - \text{Dissipation} + \text{Diffusion}, \tag{5.1}$$

where E is the depth-integrated eddy energy, which is assumed to be advected by the depth-averaged mean flow and propagated westward at the long Rossby wave speed $|c|$ (Chelton et al., 2007, 2011; Gill, 1982). Accordingly, Sections 5.2 through 5.4 present the diagnosis of EKE, EPE and the long Rossby wave phase speed. Finally, Section 5.5 explores the relationship between diagnosed EKE and EPE, aiming to determine whether the total eddy energy can be effectively parameterised by the EKE alone in regions with substantial eddy energy.

5.1 Overview of MITgcm and Model Configuration

The MITgcm (Massachusetts Institute of Technology general circulation model) (Marshall et al., 1997) solves the equations of motion that govern the ocean using the finite volume method. It incorporates various packages to parameterise subgrid-scale processes, including ocean eddies, internal waves, vertical mixing, sea ice, and geochemistry. Consequently, the MITgcm is widely applied to simulate oceanic fluid phenomena across a broad range of spatial and temporal scales.

A regional simulation of the North Atlantic Ocean in the presence of atmospheric forcing is employed to diagnose the eddy energy budget, using the model configuration and restart checkpoint files provided by Xiaoming Zhai. The configuration is described by Zhai and Marshall (2013). The model extends in latitude from 14°S to 74°N and in longitude from 100°W to 20°E, with a horizontal resolution of $1/10^{\circ}$. The water column is discretised into 33 vertical levels with vertical grid spacing increasing from 10 m at the surface to 250 m near the seafloor. The oceanic bathymetry is derived from the 5-arc-minute ETOPO5 global topography dataset (NOAA, 1988). The eddy parameterisation is disabled, allowing the model to explicitly resolve eddy dynamics. Biharmonic operators are applied for the horizontal grid-scale diffusion of tracers, utilising a background diffusivity of $1 \times 10^{10}\ \mathrm{m^4 s^{-1}}$ and a biharmonic friction is similarly applied to the horizontal momentum equations. Linear bottom friction is parameterised with a drag coefficient of 1.1×10^{-3}. The model is driven by climatological monthly-mean atmospheric forcing obtained from National Centers for Environmental Prediction-National Center for Atmospheric Research (NCEP–NCAR) reanalysis. Within 4°-wide sponge layers at the open domain boundaries, the temperature and salinity fields are restored toward monthly-averaged climatological values to approximate the influence of adjacent ocean basins. The restoring time scale varies from three days to infinite in the

sponge layer, and the influence of sea ice is neglected. Further model details are available in Zhai and Marshall (2013).

The simulation described by Zhai and Marshall (2013) was initially spun up at a $1/5^\circ$ resolution for 23 years, followed by an integration at an eddy-resolving $1/10^\circ$ resolution for an additional 9 years. For the present study, the model was restarted from the supplied checkpoint files and integrated for a further year. The diagnostic analysis utilises the 5-day snapshot output generated during this additional year. A 4-month averaging period is applied to this final-year dataset to define the mean state and extract the mesoscale eddy field in the TWA framework, providing a stable statistical baseline for the energy budget diagnostics.

The model outputs, originally structured on a Cartesian vertical grid, are mapped into the buoyancy / neutral density coordinate during the pre-processing to align with the TWA framework. To guarantee a monotonically increasing density profile with depth and ensure a well-defined buoyancy coordinate, the density field is first vertically sorted within each water column. Most of the required vertical displacements during this sorting process are confined to the mixed layer, with notable exceptions occurring in the Labrador Sea due to the deep convection. The projected neutral density coordinate comprises 152 layers. The resolution is set to 0.02 kg m^{-3} for neutral density between 27.2 and 27.8 kg m^{-3}, then refines to 0.004 kg m^{-3} between 27.80 and 28.16 kg m^{-3} to capture enhanced stratification, and 0.02 kg m^{-3} from 28.16 to 28.20 kg m^{-3}. Beyond these ranges, the neutral density resolution coarsens to 0.2 kg m^{-3}.

5.2 Eddy Energy

The depth-integrated eddy kinetic energy (EKE) and eddy potential energy (EPE) diagnosed from the MITgcm North Atlantic model are presented in Figure 5.1 and

Figure 5.2. The spatial distributions are displayed on a logarithmic scale utilising the perceptually uniform *Turbo* colour map. To clarify the diagnostic procedure, the model outputs are initially mapped into the neutral density coordinates. Within the TWA framework, the mean state is defined via a 4-month temporal average to separate the mesoscale eddy field, thereby reducing the transient noise that typically contaminates shorter averaging windows. The three-dimensional EKE and EPE fields are then evaluated using their respective definitions (3.3) and (3.8), and are subsequently integrated over the full water column.

High EKE is predominantly localised within the Gulf Stream, its extension jet, the tropical area, the Caribbean Sea and the subtropical eastern boundary current. There is also a large value of EKE in the Caribbean Sea. In contrast, the EKE in the ocean interior is substantially weaker. Meanwhile, EPE is primarily concentrated along the Gulf Stream path and within the subpolar gyre, most notably in the Labrador Sea. Overall, EPE systematically exceeds EKE in the ocean interior. Both EKE and EPE patterns reveal a dramatic eastward decline along the Gulf Stream extension region. This sharp reduction is attributed to the steering and dissipation over shallow bathymetry, indicated by the 500 m topography contour in the left panel of Figure 5.1, where enhanced bottom friction effectively suppresses mesoscale eddy activity.

Figure 5.3 illustrates the basin-integrated EKE and EPE over the North Atlantic, smoothed via a four-month running mean to examine seasonal variations. It is evident that the total EPE systematically outweighs the EKE. Furthermore, while the EKE remains relatively stable throughout the year, the EPE experiences a substantial increase during the winter months, driven by the seasonal deepening of the mixed layer and the corresponding displacement of isopycnal outcrops. It should be noted that this time series represents only the final year of the simulation. Therefore, while it captures a seasonal cycle, a longer simulation period would be

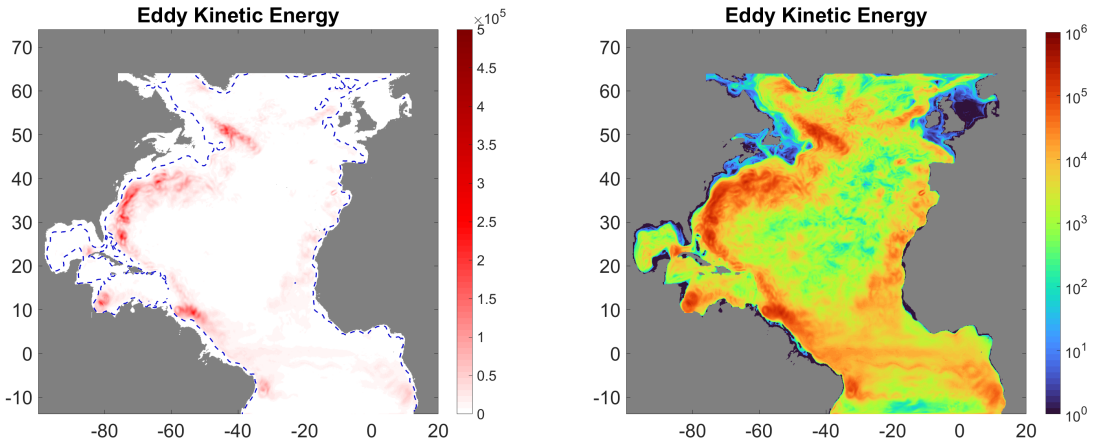


Figure 5.1: Depth-integrated eddy kinetic energy ($\mathrm{kg\ s^{-2}}$) on the linear scale (left panel) and logarithmic scale (right panel) diagnosed from the North Atlantic simulation. The left panel contains a 500 m topography contour (the blue dashed line).

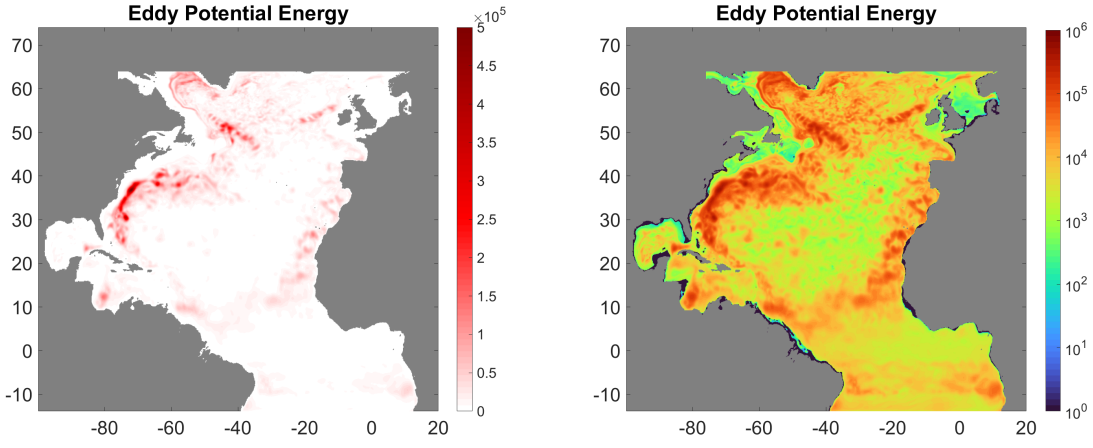


Figure 5.2: Depth-integrated eddy potential energy ($\mathrm{kg\ s^{-2}}$) on the linear scale (left panel) and logarithmic scale (right panel) diagnosed from the North Atlantic simulation.

required to assess inter-annual variability.

To validate the model results, the diagnosed eddy energy in the upper ocean is compared against observational estimates derived from Argo floats and AVISO satellite altimetry data, presented in Figure 5.4 and Figure 5.5. Because the present diagnostic analysis operates in the buoyancy coordinates, the model eddy energy is mapped along specific isopycnal surfaces on a logarithmic scale. Specifically, Figure 5.4 displays the eddy energy on the neutral density surface of $27.0\ \mathrm{kg\ m^{-3}}$, which generally resides in the upper 500 meters, allowing for a qualitative comparison with the observational data in Figure 5.5. To provide context for the observational data, Roullet et al. (2014) reconstructed the global interior eddy available potential energy by estimating isopycnal displacements from Argo float profiles relative to a long-term climatological mean state, and applying the classic quasi-geostrophic approximation.

Through dimensional analysis utilising the thermal-wind balance (Vallis, 2017), the theoretical ratio between EKE and EPE can be estimated as

$$\frac{\mathrm{EKE}}{\mathrm{EPE}} = \frac{1/2\rho_0 \widehat{\boldsymbol{u}_h'' \cdot \boldsymbol{u}_h''}}{1/2\rho_0 \overline{\sigma}^{-1} \overline{\zeta'^2}} \approx \frac{U^2}{f^2 U^2 L^2 / \left(\mathcal{N}_0^2 H^2\right)} = \frac{\mathcal{N}_0^2 H^2}{f^2 L^2} = \frac{L_d^2}{L^2}, \tag{5.2}$$

where U is the characteristic horizontal velocity scale, L the horizontal length scale, and H the vertical scale of the eddies; f is the Coriolis parameter, $\mathcal{N}_0$ is the background buoyancy frequency, and $L_d \equiv \mathcal{N}_0 H / f$ denotes the Rossby radius of deformation. The diagnostic finding that EPE and EKE are of comparable magnitude implies that the mesoscale eddies resolved in the model are fundamentally scaled by the Rossby deformation radius ($L \sim L_d$).

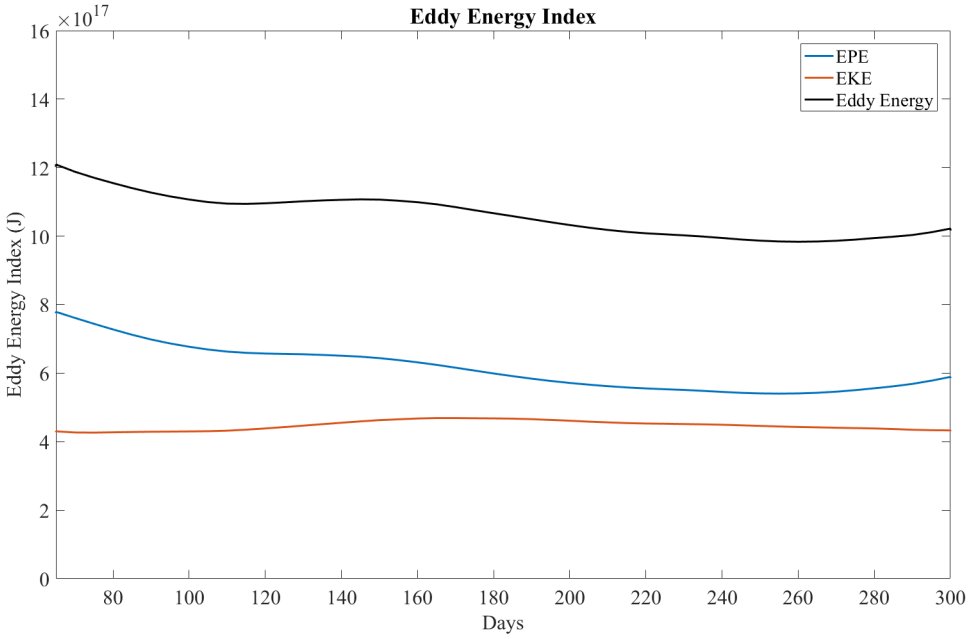


Figure 5.3: Eddy potential energy (blue) and eddy kinetic energy (red) over the North Atlantic basin (J), smoothed via a 4-month running mean.

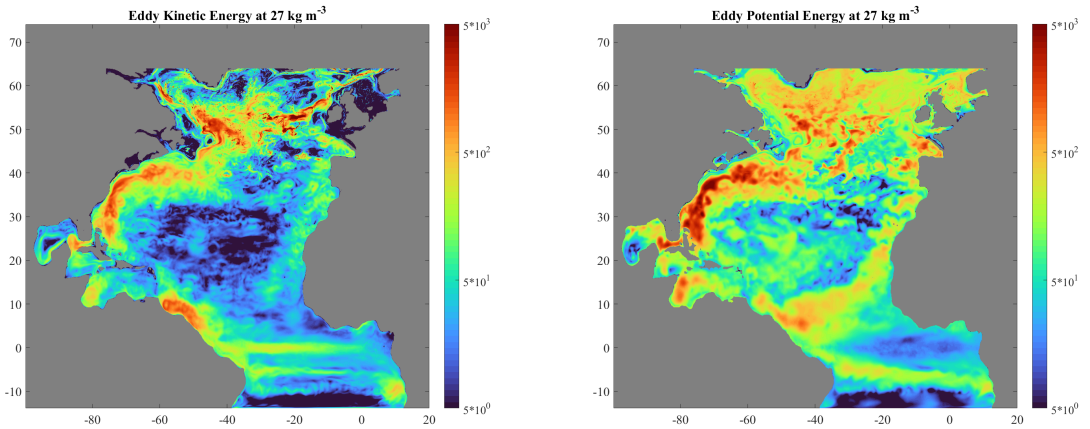


Figure 5.4: The eddy kinetic energy (left panel) and eddy potential energy (right panel) on the 27.0 $\mathrm{kg\ m^{-3}}$ neutral density surface diagnosed from the North Atlantic simulation. Note that the variables are presented as specific energies (i.e., normalised by the reference density ρ_0) to maintain unit consistency ($\mathrm{cm^2\ s^{-2}}$) with the observational data in Figure 5.5.

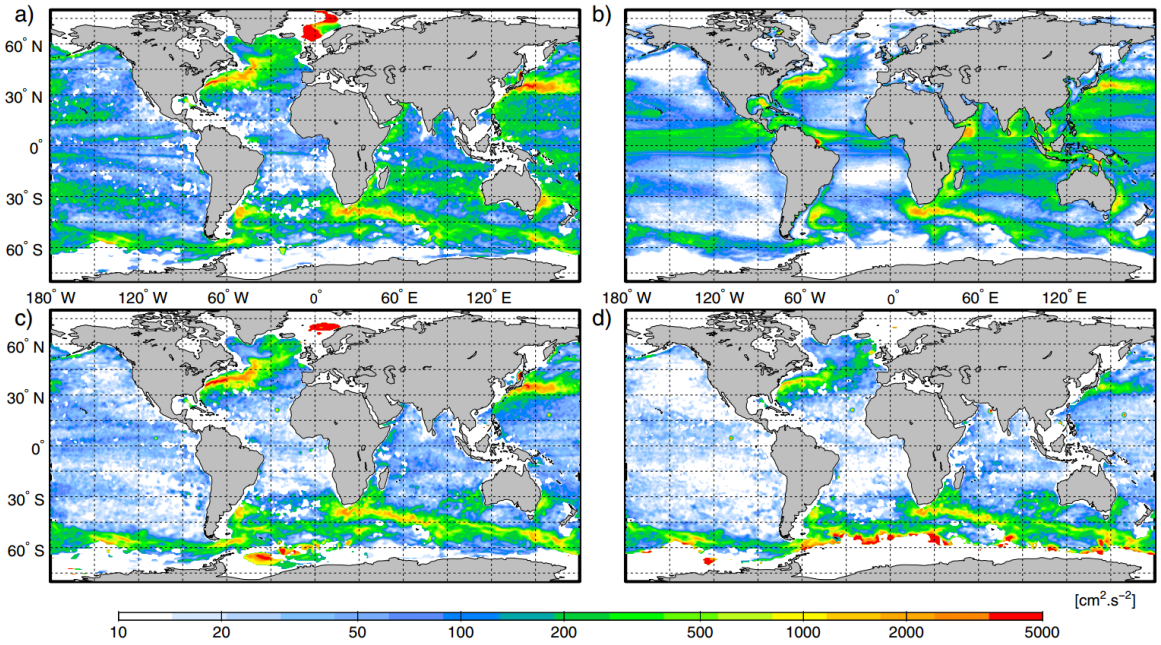


Figure 5.5: Global eddy energy diagnosed from observational data, reproduced from Roullet et al. (2014). (a), (c), (d) Eddy available potential energy (EAPE; $\mathrm{cm}^2\ \mathrm{s}^{-2}$) derived from Argo floats at depths of 250m, 500m, and 1000m, respectively. (b) Eddy kinetic energy ($\mathrm{cm}^2\ \mathrm{s}^{-2}$) diagnosed from AVISO sea level anomaly measurements. All panels are displayed on a logarithmic scale.

5.3 Eddy Energy Source

Recalling the eddy kinetic energy (EKE) and eddy potential energy (EPE) equations (4.8) and (4.27) derived in Chapter 4, the diagnostic evaluation of the vertically-integrated eddy energy sources can be performed. The governing equations are formulated as

$$\frac{1}{\rho_0}\frac{\mathrm{D}^\sharp}{\mathrm{D}t}\left(\mathrm{EKE}\right)+\nabla\cdot\boldsymbol{J}^{\left(\frac{\boldsymbol{u_h}\cdot\boldsymbol{u_h}}{2}\right)}-\hat{u}\,\nabla\cdot\boldsymbol{J}^{\boldsymbol{u}}-\hat{v}\,\nabla\cdot\boldsymbol{J}^{\boldsymbol{v}}+\left[\widehat{u''\left(m_{\tilde{x}}\right)''}\right]+\left[\widehat{v''\left(m_{\tilde{y}}\right)''}\right]=\widehat{\boldsymbol{u}_{\boldsymbol{h}}''\cdot\boldsymbol{F}_{\boldsymbol{h}}''}\,,$$

$$\begin{aligned}\frac{1}{\rho_0}\frac{\mathrm{D}^\sharp}{\mathrm{D}t}\left(\mathrm{EPE}\right)-\frac{1}{\rho_0}\mathrm{EPE}\left(\hat{u}_{\tilde{x}}+\hat{v}_{\tilde{y}}+\hat{\varpi}_{\tilde{b}}\right)+\overline{\sigma}^{-1}\,\overline{\boldsymbol{U}''\cdot\nabla\,\frac{\zeta'^2}{2}}\\=-\overline{\sigma}^{-1}\left(\overline{u'\zeta'}\,\overline{\zeta_{\tilde{x}}}+\overline{v'\zeta'}\,\overline{\zeta_{\tilde{y}}}\right)+\overline{\sigma}^{-1}\overline{w'\zeta'}\,.\end{aligned}$$

In the EKE equation, the Reynolds stress and Montgomery potential terms make non-vanishing net contributions to the basin-integrated eddy energy source, as they do not reduce to pure transport fluxes. Meanwhile, the first term (horizontal buoyancy flux) on the right-hand side of the EPE equation accounts for the eddy energy released by the baroclinic instability, whereas the second term (vertical buoyancy flux) governs the eddy energy conversion from the EPE field to the EKE field.

The primary components of the domain-integrated eddy energy sources are presented in Figure 5.6. Each term is written as a source contribution to its respective energy equation; thus, positive values increase EKE or EPE, as appropriate. The diagnostic indices are integrated over the entire basin, with the mean and eddy fields defined using a 4-month moving averaging window. Baroclinic instability and the Montgomery potential work provide a substantial increase in eddy energy, while the contribution of Reynolds stress is relatively minor. The negative sign of

the vertical buoyancy flux indicates a persistent energy transfer from the EPE field to the EKE field.

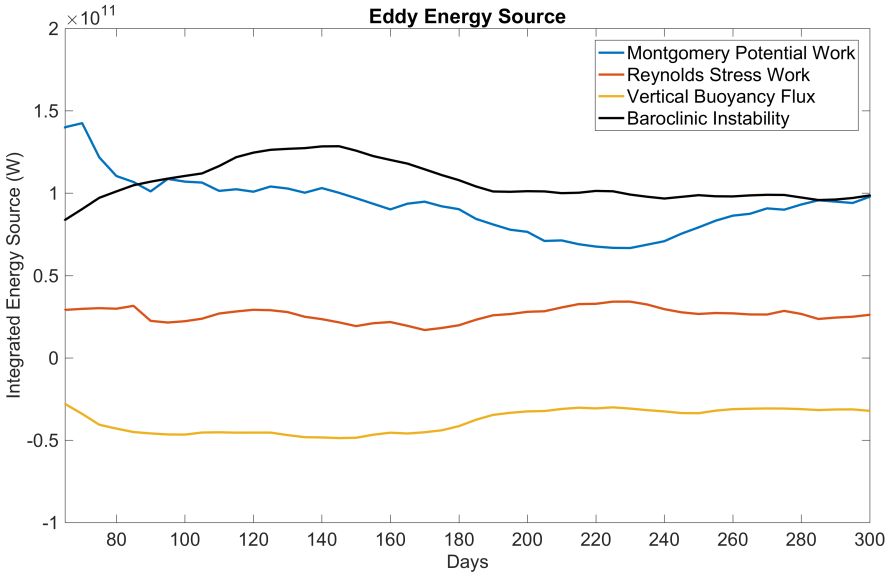


Figure 5.6: Basin-integrated eddy energy budget contributions over the North Atlantic (W), diagnosed using a 4-month moving averaging window. The Montgomery potential work (blue) and Reynolds stress work (red) are the corresponding source contributions from (4.8). The baroclinic instability (black) corresponds to the negative of the horizontal part of the fourth term on the left-hand side of (4.27), while the vertical buoyancy flux (yellow) corresponds to its right-hand-side term. All curves use the source-side sign convention, so positive values increase the energy in the corresponding EKE or EPE budget.

From the perspective of the EPE budget, the basin-integrated source and advection terms are illustrated in Figure 5.7. The mean-flow and eddy-flow advection contributions correspond to the horizontal parts of the second term on the left-hand side of (4.28), associated with $\widehat{\boldsymbol{U}}$ and $\boldsymbol{U}''$, respectively. These terms are integrated over the basin and plotted using the source-side sign convention. The two advective contributions effectively cancel each other out, resulting in a negligible

net advection (shown in purple). Consistent with Figure 5.6, baroclinic instability remains the dominant source term in the EPE budget.

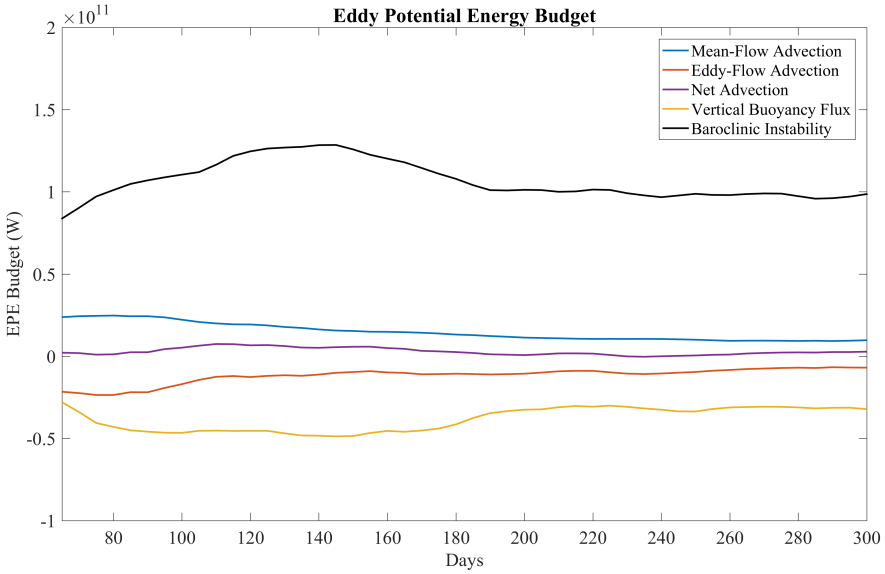


Figure 5.7: Basin-integrated EPE budget contributions over the North Atlantic (W), diagnosed using a 4-month moving averaging window. Mean-flow advection (blue) and eddy-flow advection (red) correspond to the horizontal contributions involving $\widehat{\boldsymbol{U}}$ and $\boldsymbol{U}''$, respectively, in the second term on the left-hand side of (4.28). Net advection (purple) is their sum. The vertical buoyancy flux (yellow) and baroclinic instability (black) are the right-hand-side term and the negative of the horizontal part of the third left-hand-side term in (4.28), respectively. All curves include the factor ρ_0 and use the source-side sign convention.

The spatial distributions of the depth-integrated eddy energy source terms, regionally smoothed over $1^\circ \times 1^\circ$ grid boxes, are shown in Figure 5.8. The Montgomery potential and Reynolds stress terms contribute to the EKE source, featuring significant values localised along the western boundary current, the subpolar gyre and the eastern coast of subtropical regions. This spatial distribution broadly corresponds to the pattern of eddy energy. The Reynolds stress term exhibits lo-

calised alternating positive and negative contributions along the Gulf Stream and its extension. Eddy feedbacks can decelerate the upstream jet core and weakly accelerate the downstream jet in idealised barotropic jet simulations (Waterman and Lilly, 2015). The baroclinic instability and vertical buoyancy flux terms exhibit some spatial correspondence in the vicinity of the Gulf Stream, with locally opposing signs. Where positive baroclinic contributions coincide with negative vertical buoyancy flux, the pattern is consistent with extraction of potential energy from the mean state and subsequent conversion from EPE to EKE. Furthermore, relatively large values of the baroclinic instability term are also present in the subpolar gyre, a region where the vertical buoyancy flux remains comparatively quiescent. Overall, the fields in this averaging window provide only weak evidence for the expected regional patterns of Reynolds stress feedback and of EPE production and conversion to EKE.

The combined eddy energy source diagnostic, summing the four components from Figure 5.8, is illustrated in Figure 5.9. Large positive values are concentrated densely along the western boundary. The explicit energy-transport terms of the full eddy energy budget are not included in this diagnostic, so the map alone does not establish a local balance between energy sources and dissipation. In a balanced energy cycle, these source contributions may be offset by energy transport as well as localised eddy energy sinks, such as coastal friction, bottom friction and wind-eddy interactions. The western boundary has been described as a “graveyard” of eddy energy because of its intense eddy energy dissipation (Zhai et al., 2010).

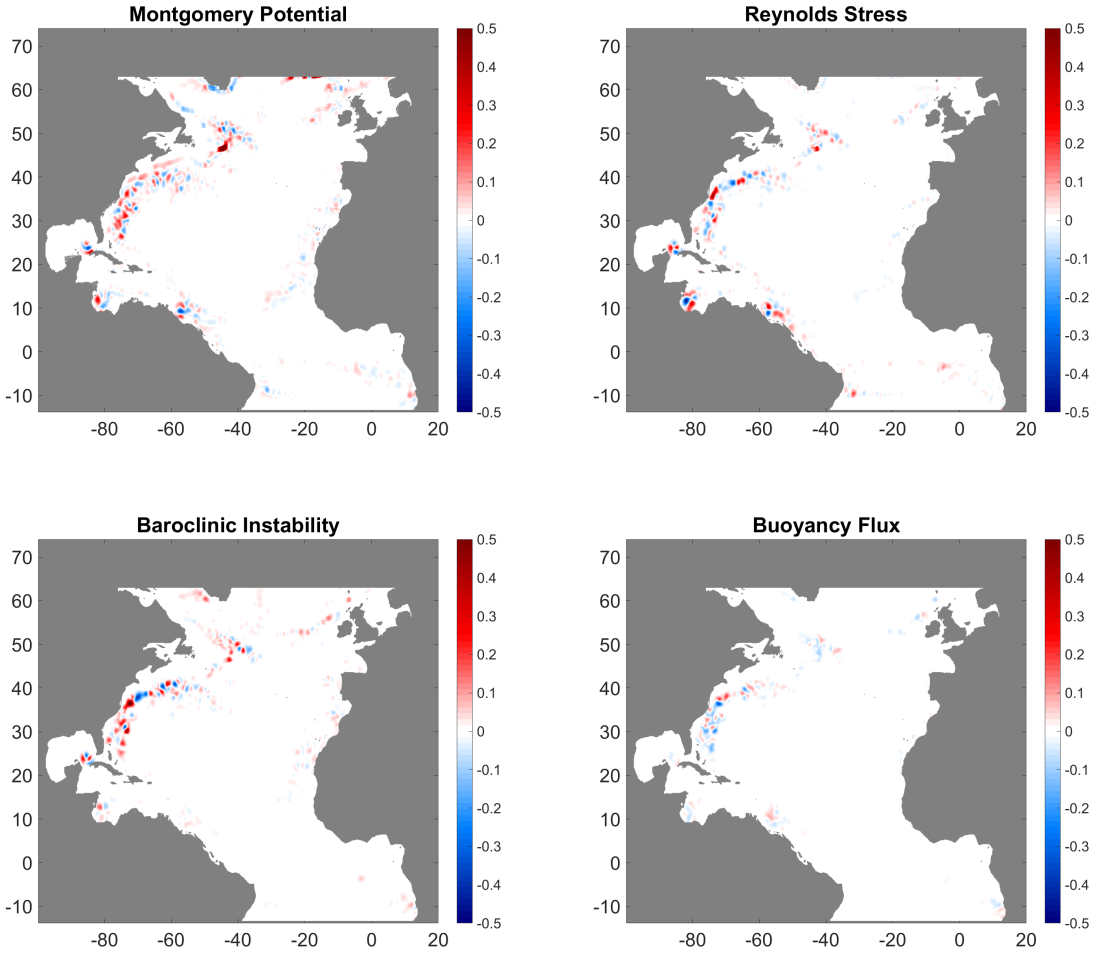


Figure 5.8: Depth-integrated eddy energy sources over the North Atlantic basin (Wm^{-2}), including the contributions of Montgomery potential, Reynolds stress, baroclinic instability and vertical buoyancy flux. The fields are diagnosed for day 275 of the additional simulation year using a centred 4-month averaging window spanning days 215–335. Fields are regionally smoothed over $1^\circ \times 1^\circ$ grid boxes.

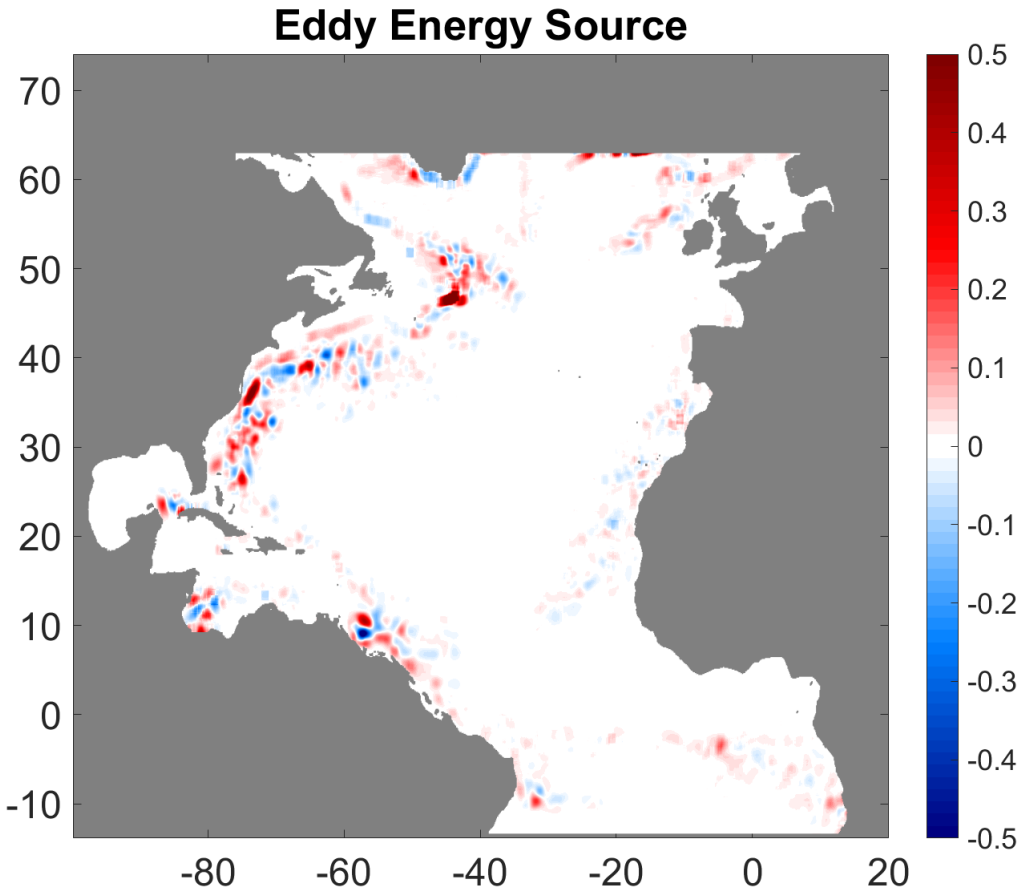


Figure 5.9: Depth-integrated total eddy energy source over the North Atlantic basin (Wm^{-2}), regionally smoothed over $1^\circ \times 1^\circ$ grid boxes. The explicit energy-transport terms of the full budget are not included.

5.4 The Phase Speed of Long Baroclinic Rossby Wave

In this section, the propagation term associated with the Rossby waves in (5.1) is further investigated. Chelton et al. (2007, 2011) employ an automatic algorithm to identify and track the eddies according to sea-surface height (SSH) fields. The tracked mesoscale eddies are observed to propagate westward approximately at the phase speed of long baroclinic Rossby waves.

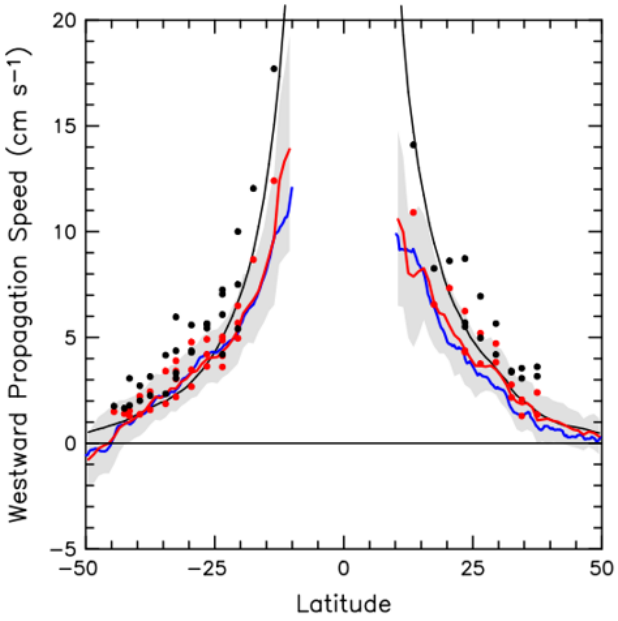


Figure 5.10: Latitudinal variation of eddy westward zonal propagation speed ($\mathrm{cm\ s^{-1}}$) estimated by various methods, reproduced from Chelton et al. (2011). The black and red dots represent the eddy performance in 45 selected areas. The red and blue lines denote results from the global zonal average. The black line indicates the long baroclinic Rossby wave phase speed predicted by the classical theory.

First, the classical long Rossby wave theory is reviewed. The Rossby wave is essentially the linear response of potential vorticity to small perturbations. The adjustment processes after small perturbations in the continuously stratified ocean

are examined. Following Tulloch et al. (2009) and Vallis (2017), the westward phase speed of the non-dispersive Rossby wave is derived.

The quasi-geostrophic potential vorticity (QGPV) on the β-plane is

$$\mathrm{QGPV} \overset{def}{=} \beta y + \nabla^2 \psi + \left(\frac{f^2}{\mathcal{N}_0^2} \psi_z \right)_z , \tag{5.3}$$

where ψ is the stream function satisfying $\boldsymbol{u} = -\psi_y \boldsymbol{i} + \psi_x \boldsymbol{j}$.

Assuming the background mean state satisfies $\partial_t \overline{q} + \overline{\boldsymbol{u}} \cdot \nabla \overline{q} = 0$, the linearised QGPV equation in the ocean interior is

$$\frac{\partial q'}{\partial t} + \overline{\boldsymbol{u}} \cdot \nabla q' + \boldsymbol{u'} \cdot \nabla \overline{q} = 0. \tag{5.4}$$

Considering an ocean state of rest, i.e. $\overline{\boldsymbol{u}} = 0$ and $\overline{q} = \beta y$, the linearised QGPV equation (5.4) can be further simplified to

$$\frac{\partial}{\partial t} \left[\nabla^2 \psi' + \left(\frac{f^2}{\mathcal{N}_0^2} \psi'_z \right)_z \right] + \beta \frac{\partial \psi'}{\partial x} = 0. \tag{5.5}$$

Solutions of the wave form are sought:

$$\psi' (x, y, z, t) = \mathrm{Re} \left\{ \tilde{\psi} (z) \, e^{i(kx + ly - \omega t)} \right\}, \tag{5.6}$$

where $\tilde{\psi}(z)$ represents the vertical structure of the Rossby wave, and k and l are the zonal and meridional wavenumbers, respectively. Substituting the wave solution (5.6) into (5.5) yields

$$\omega \left[-K^2 \tilde{\psi} + \left(\frac{f^2}{\mathcal{N}_0^2} \tilde{\psi}_z \right)_z \right] - \beta k \tilde{\psi} = 0, \tag{5.7}$$

where $K^2 \overset{def}{=} k^2 + l^2$ is the squared horizontal wavenumber.

Specifically, the “neutral modes" of the vertical structures $\tilde{\psi}_n$ satisfy

$$\frac{\mathrm{d}}{\mathrm{d}z}\left(\frac{f^2}{\mathcal{N}_0^2}\frac{\mathrm{d}\tilde{\psi}_n}{\mathrm{d}z}\right) = -\Gamma_n^2\tilde{\psi}_n,\ \left.\frac{\mathrm{d}\tilde{\psi}_n}{\mathrm{d}z}\right|_{z=0,-H} = 0,\ n \in \mathbb{N}. \tag{5.8}$$

Equation (5.8) is a Sturm-Liouville problem, and the resulting neutral modes constitute an orthonormal basis for the vertical structure of the Rossby wave. If the resting ocean has a uniform stratification (i.e. $\mathcal{N}_0^2$ is a constant), the analytical solution have the eigenfunctions $\tilde{\psi}_n(z) = \cos(n\pi z/H)$ and the related eigenvalues $\Gamma_n^2 = (fn\pi)^2/(\mathcal{N}_0 H)^2$. Otherwise, the solutions of (5.8) are sought utilising numerical methods. The neutral modes also determine the Rossby deformation radius L_n associated with the nth baroclinic mode, namely

$$L_n \overset{def}{=} \frac{1}{\Gamma_n} = \frac{\mathcal{N}_0 H}{n\pi f}. \tag{5.9}$$

Substituting (5.8) and (5.9) into (5.7) provides the Rossby wave dispersion relationship in the resting ocean:

$$\omega_n = -\frac{\beta k}{K^2 + L_n^{-2}}. \tag{5.10}$$

The westward zonal wave phase speed corresponding to the nth baroclinic mode is defined as

$$c_n \overset{def}{=} \frac{\omega_n}{k} = -\frac{\beta}{k^2 + l^2 + L_n^{-2}}. \tag{5.11}$$

This indicates that the maximum westward propagation for a given zonal wavenumber k occurs when the meridional wavenumber is zero ($l = 0$). Letting the total horizontal wavenumber K reduce to zero, the Rossby wave phase speed under the non-dispersive long-wave limit is acquired:

$$c_{\mathrm{Rossby}} \overset{def}{=} -\beta L_n^2. \tag{5.12}$$

Relevant variables estimated from the annual mean hydrographic data in the North Atlantic model are presented here. The zonally-averaged Rossby deformation radius of the first baroclinic mode is diagnosed (not shown). It is found that most of the ocean interior (beyond $10^{\circ}\mathrm{N}$) has a deformation radius smaller than $100\,\mathrm{km}$. The spatial pattern of the non-dispersive long Rossby wave phase speed and the corresponding zonal mean are shown in Figure 5.11. The diagnosed phase speed is mainly controlled by latitude, with comparatively weak zonal variation away from regions of complex bathymetry. Its latitudinal dependence and order of magnitude are broadly consistent with the observational estimates in Figure 5.10 from Chelton et al. (2011).

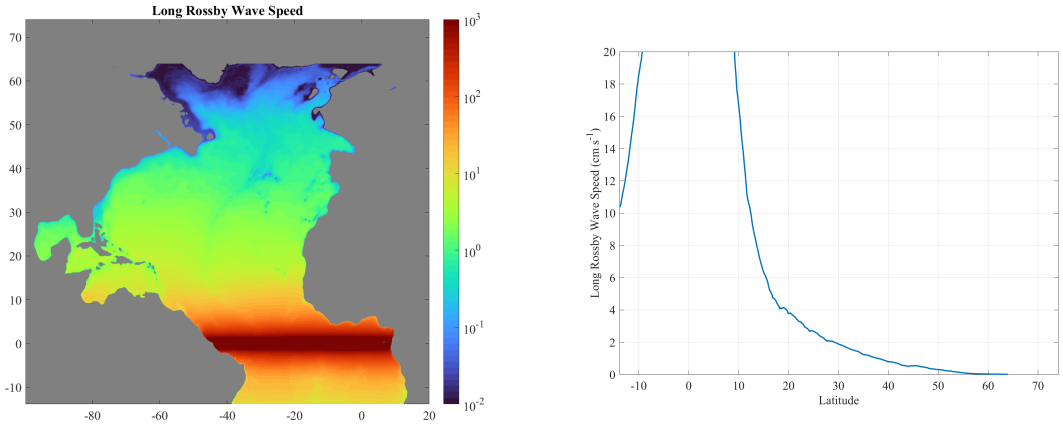


Figure 5.11: Long Rossby wave phase speed diagnosed from the first baroclinic mode. The left panel shows the spatial distribution in $\mathrm{cm\,s^{-1}}$ on a logarithmic colour scale, and the right panel shows the zonal mean phase speed in $\mathrm{cm\,s^{-1}}$ as a function of latitude.

5.5 Positive Correlation between EPE and EKE

The diagnosed depth-integrated eddy energy shown in Figure 5.1 and Figure 5.2 exhibits a positive correlation between depth-integrated EPE and EKE. This relation-

ship is relevant to eddy parameterisation because, in the GEOMETRIC framework, the total eddy energy constrains the eddy fluxes in the E-P tensor. This section quantifies the local relationship between EPE and EKE and assesses whether EKE can provide a useful diagnostic predictor for EPE.

A baseline linear regression is first performed between EPE and EKE on the logarithmic scale at each snapshot of the diagnosed eddy energy, i.e.

$$\log_{10}(\mathrm{EPE}) = \beta_1 \log_{10}(\mathrm{EKE}) + \beta_0, \tag{5.13}$$

where β_1 is the slope and β_0 is the intercept. The expression of the linear regression is also equivalent to

$$\mathrm{EPE} = 10^{\beta_0} \cdot (\mathrm{EKE})^{\beta_1}\,. \tag{5.14}$$

The ordinary least squares (OLS) fit provides a baseline estimate by minimising the unweighted residual sum of squares. However, the scatter distribution contains numerous low-energy points, which can strongly influence the unweighted least-squares criterion. As a result, the unweighted fit can deviate from the local orientation of the high-density scatter contours in the energetic range. Weighted linear regression therefore serves as a diagnostic tool to emphasise high-energy regions while retaining the same logarithmic relationship in (5.13).

Weighted Linear Regression

Weighted least squares (WLS), applied here as weighted linear regression, provides a standard way to assign different contributions to different observations in the least-squares cost function (Kutner et al., 2005, Section 11.1). Here, it is used to prioritise the fitting accuracy of higher-magnitude eddy energy.

In the traditional linear regression, which assumes a linear model $\hat{y} = \beta_1 x + \beta_0$,

the cost function based on the least squares estimate is

$$f = \sum_{i=1}^{n} (y_i - \hat{y}_i)^2 \,, \tag{5.15}$$

assuming the length of the data series is n. The matrix form is then

$$f = (\boldsymbol{Y} - \boldsymbol{X}\boldsymbol{\beta})^T (\boldsymbol{Y} - \boldsymbol{X}\boldsymbol{\beta}) \,, \tag{5.16}$$

where $\boldsymbol{\beta} = (\beta_0, \beta_1)^T$, $\boldsymbol{Y} = (y_1, \ldots, y_n)^T$, and the design matrix is

$$\boldsymbol{X} = \begin{bmatrix} 1 & x_1 \\ 1 & x_2 \\ \vdots & \vdots \\ 1 & x_n \end{bmatrix} . \tag{5.17}$$

The estimate of the parameter is

$$\boldsymbol{\beta} = \left(\boldsymbol{X}^T \boldsymbol{X}\right)^{-1} \boldsymbol{X}^T \boldsymbol{Y}. \tag{5.18}$$

In weighted linear regression, the weighted cost function is

$$f_w = \sum_{i=1}^{n} w_i \, (y_i - \hat{y}_i)^2 \,. \tag{5.19}$$

The corresponding matrix form is simply

$$f_w = (\boldsymbol{Y} - \boldsymbol{X}\boldsymbol{\beta})^T \boldsymbol{W} (\boldsymbol{Y} - \boldsymbol{X}\boldsymbol{\beta}) \,, \tag{5.20}$$

where the diagonal weight matrix $\boldsymbol{W}$ is defined as

$$\boldsymbol{W} = \begin{bmatrix} w_1 & 0 & \cdots & 0 \\ 0 & w_2 & \cdots & 0 \\ \vdots & \vdots & \ddots & \vdots \\ 0 & 0 & \cdots & w_n \end{bmatrix} \in \mathbb{R}^{n \times n}. \tag{5.21}$$

The weighted linear regression coefficients are obtained by minimising the weighted cost function:

$$\boldsymbol{\beta}_w = \left(\boldsymbol{X}^T \boldsymbol{W} \boldsymbol{X}\right)^{-1} \boldsymbol{X}^T \boldsymbol{W} \boldsymbol{Y}. \tag{5.22}$$

The weighted problem can be written as an ordinary least-squares problem by defining $\boldsymbol{Y}^* = \boldsymbol{W}^{\frac{1}{2}} \boldsymbol{Y}$ and $\boldsymbol{X}^* = \boldsymbol{W}^{\frac{1}{2}} \boldsymbol{X}$. The transformed design matrix is

$$\boldsymbol{X}^* = \begin{bmatrix} \sqrt{w_1} & \sqrt{w_1} x_1 \\ \sqrt{w_2} & \sqrt{w_2} x_2 \\ \vdots & \vdots \\ \sqrt{w_n} & \sqrt{w_n} x_n \end{bmatrix}. \tag{5.23}$$

Thus the intercept column in the original design matrix is also transformed by the weights. Weighted linear regression is therefore not equivalent to a simple OLS regression of $\sqrt{w_i} y_i$ against $\sqrt{w_i} x_i$ with an intercept. Instead, in the transformed space, it is equivalent to an OLS regression with no additional intercept column and two predictors, namely $\sqrt{w_i}$ and $\sqrt{w_i} x_i$. Consequently, the coefficients β_0 and β_1 are obtained directly from this transformed regression.

The regressions are evaluated using the coefficient of determination R^2. These diagnostics are used both to select the weight exponent and to assess the final OLS

and WLS fits. For the OLS fit, the standard definition is

$$R^2_{\mathrm{OLS}} \overset{def}{=} 1 - \frac{\sum \left(y_i - \hat{y}_{u,i}\right)^2}{\sum \left(y_i - \bar{y}\right)^2}\,, \tag{5.24}$$

where $\hat{y}_{u,i}$ is the prediction from the unweighted regression and $\bar{y}$ is the unweighted mean of y_i. For the WLS fit, two related diagnostics are useful. The weighted coefficient of determination evaluates the fit in the same weighted space as the WLS cost function:

$$R^2_{\mathrm{WLS},w} \overset{def}{=} 1 - \frac{\sum w_i \left(y_i - \hat{y}_{w,i}\right)^2}{\sum w_i \left(y_i - \bar{y}_w\right)^2}\,, \tag{5.25}$$

where $\hat{y}_{w,i}$ is the prediction from the weighted regression and the weighted mean is

$$\bar{y}_w \overset{def}{=} \frac{\sum w_i y_i}{\sum w_i}\,. \tag{5.26}$$

In contrast, the same WLS fit can also be evaluated in the original unweighted sample space:

$$R^2_{\mathrm{WLS},u} \overset{def}{=} 1 - \frac{\sum \left(y_i - \hat{y}_{w,i}\right)^2}{\sum \left(y_i - \bar{y}\right)^2}\,. \tag{5.27}$$

These two WLS diagnostics answer different questions. The weighted value $R^2_{\mathrm{WLS},w}$ measures how well the WLS fit explains the variance emphasised by the chosen weights, whereas $R^2_{\mathrm{WLS},u}$ measures how the same weighted fit performs over the full unweighted sample. Therefore, a higher weighted R^2 should not be interpreted as a uniformly better fit over all data points.

For the diagnostic application, the weights are chosen as a power of the dimensional EKE at each grid point:

$$w_i = \left(\mathrm{EKE}_i\right)^{\alpha}\,. \tag{5.28}$$

The unweighted case is recovered when $\alpha = 0$. To choose α, a range of exponents

was applied snapshot by snapshot. The diagnostic scan examined the mean and standard deviation of the fitted slope, the weighted and unweighted coefficients of determination, the residual error, and the concentration of the weights. An alternative weighting based on powers of $\log_{10}(\mathrm{EKE})$ was also tested as a sensitivity check, but the dimensional EKE-based weight has a more direct physical interpretation and is therefore used for the final analysis.

For each snapshot, let n denote the number of valid paired EKE–EPE grid points used in the regression. The effective sample size is defined as

$$n_{\mathrm{eff}} \overset{def}{=} \frac{\left(\sum_{i=1}^{n} w_i\right)^2}{\sum_{i=1}^{n} w_i^2},$$

and the effective sample size ratio is n_{eff}/n. This ratio equals one for equal weights and decreases as the weights become more concentrated. It is used here as a measure of weight concentration.

The top 1% and top 5% weight shares are the fractions of the total weight carried by the highest-EKE 1% and 5% of the grid points, respectively. These weight-concentration diagnostics are calculated for each snapshot and then averaged across snapshots.

Figure 5.12 summarises the main trade-off in the EKE-based exponent scan. Increasing α gives more influence to energetic points. Panel (a) shows that the mean fitted slope initially increases with α, reaches a maximum near $\alpha = 2$, and then decreases. Panel (b) shows that the weighted coefficient of determination reaches a high value near $\alpha = 1$, indicating an improved fit in the weighted space. However, panel (c) shows that larger values of α degrade the unweighted coefficient of determination for the same WLS fits. Panel (d) further shows that increasing α concentrates the regression on a progressively smaller fraction of the sample, as indicated by the reduction in the effective sample size ratio and the increasing

share of the total weight carried by the largest EKE values. The final analysis uses $\alpha = 1$, so that $w_i = \mathrm{EKE}_i$. This choice emphasises energetic regions more strongly than OLS, retains a simple physical interpretation, and avoids selecting a larger tuned exponent solely to force the fitted slope toward unity.

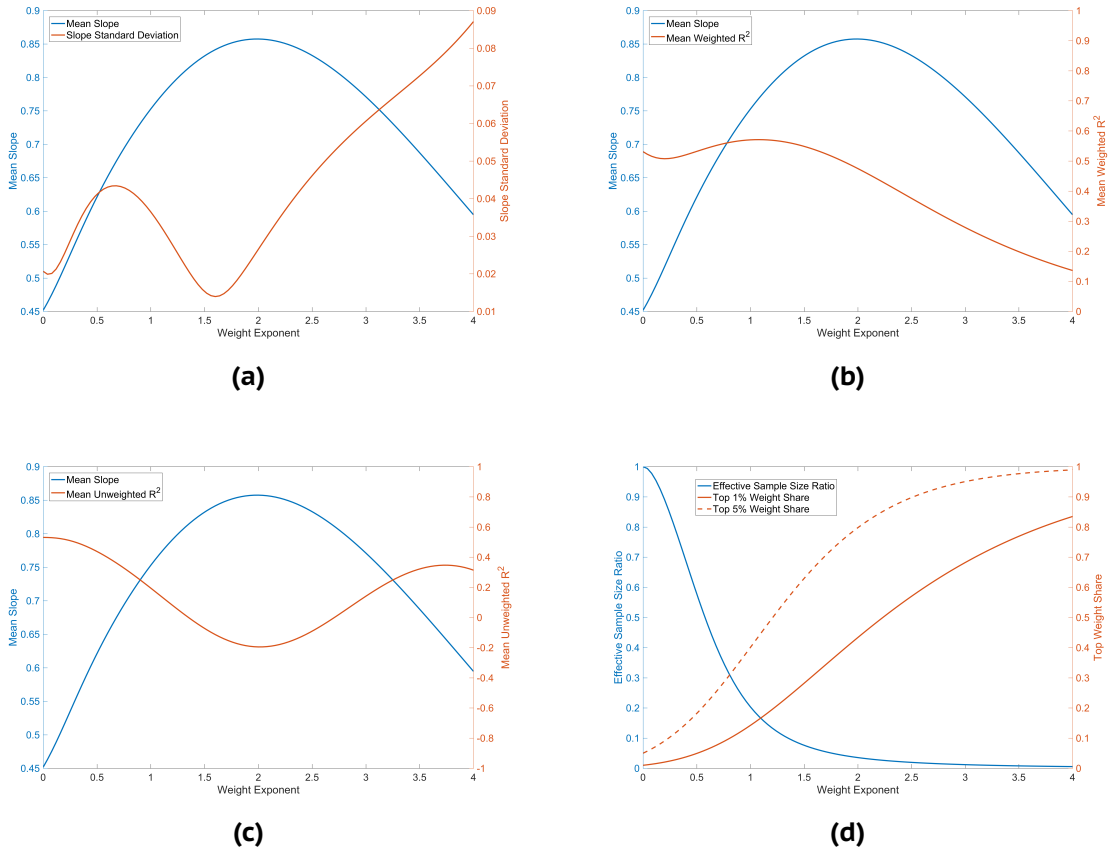


Figure 5.12: Diagnostics used to select the exponent in the EKE-based weight $w_i = (\mathrm{EKE}_i)^{\alpha}$. Panel (a) shows the mean and sample standard deviation of the fitted slope β_1 across snapshots. Panels (b) and (c) show the weighted and unweighted WLS coefficients of determination, respectively. Panel (d) shows the effective sample size ratio n_{eff}/n and the top 1% and top 5% weight shares.

Figure 5.13 compares the OLS and WLS fits for one snapshot of the diagnosed eddy energy. The WLS fit uses the weights in (5.28) with $\alpha = 1$. In the OLS panel, the fitted line is pulled by the numerous low-energy points and deviates from the

orientation of the high-density contours in the energetic range. Relative to the OLS fit, the WLS fit gives greater influence to the high-EKE part of the scatter distribution and therefore follows the high-energy branch more closely.

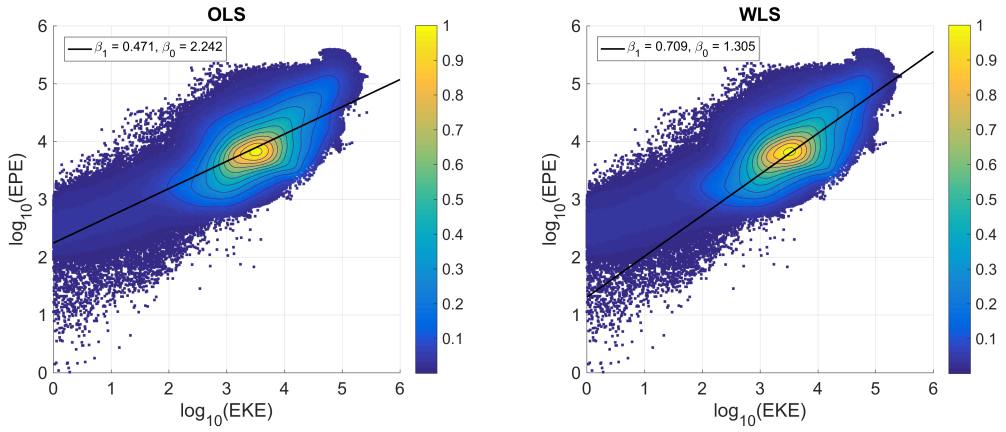


Figure 5.13: Scatter plot between EPE and EKE on the logarithmic scale at one snapshot of the eddy energy. The underlying EPE and EKE fields are depth-integrated quantities in $\mathrm{kg\ s^{-2}}$ before the logarithm is taken. The left panel shows the OLS fit, while the right panel shows the WLS fit with $w_i = \mathrm{EKE}_i$. The black lines show the fitted linear regressions in (5.13); β_1 and β_0 denote the slope and intercept, respectively. The colour shading and contours represent the scatter density.

Applying the same procedure to each snapshot gives the time-dependent regression coefficients shown in Figure 5.14. The WLS fit produces a larger slope and a smaller intercept than the OLS fit because the energetic part of the scatter distribution follows a steeper branch in logarithmic space. The coefficients remain time dependent, indicating that the EPE–EKE relation is not a fixed proportionality across all snapshots.

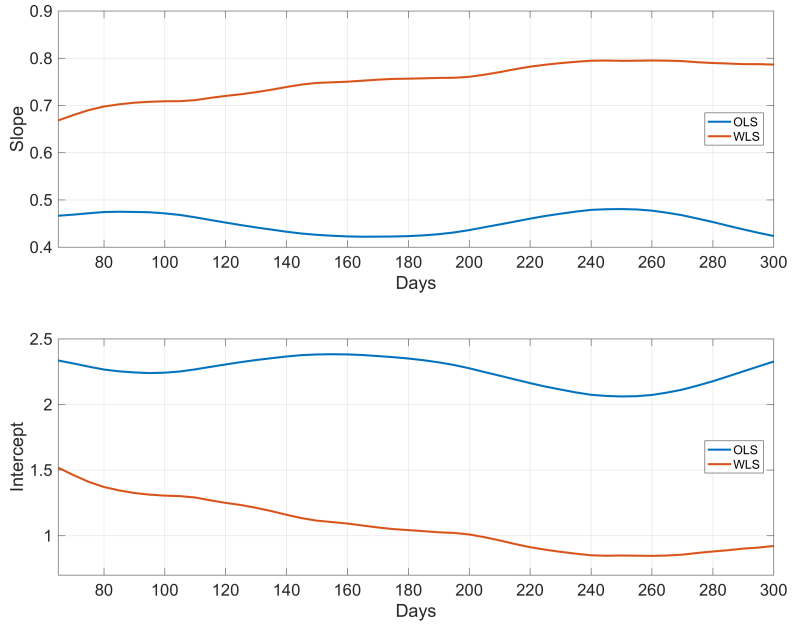


Figure 5.14: Slope and intercept from the OLS and WLS regressions between EPE and EKE on the logarithmic scale. The WLS regression uses $w_i = \mathrm{EKE}_i$. The horizontal axis shows the valid days after excluding the endpoints affected by the running-mean window.

Figure 5.15 shows the three R^2 diagnostics for the valid snapshots. The weighted R^2 of the WLS fit is generally higher than the OLS R^2, confirming that the weighted regression improves the description of the high-EKE part of the distribution. By contrast, the unweighted R^2 of the WLS fit is lower than the OLS R^2, as expected because OLS is the least-squares optimum in the unweighted space. This contrast shows that the WLS fit should be interpreted as a targeted diagnostic for energetic regions rather than a globally superior regression over the full scatter distribution.

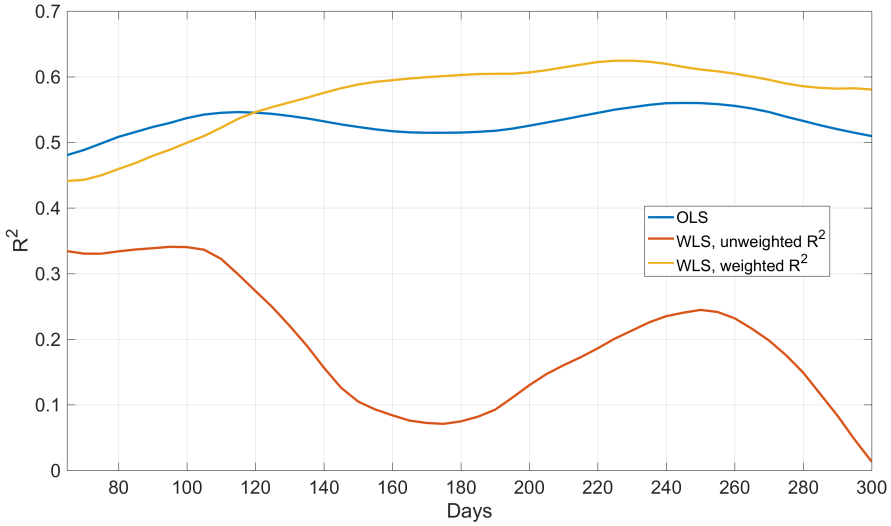


Figure 5.15: Coefficient of determination for the OLS and WLS regressions between EPE and EKE on the logarithmic scale. The WLS regression uses $w_i = \mathrm{EKE}_i$. The unweighted WLS R^2 evaluates the WLS fit in the original sample space, whereas the weighted WLS R^2 evaluates the same fit in the weighted space used by the WLS cost function.

The fitted log–log regressions can also be used to reconstruct EPE from EKE through $\widehat{\mathrm{EPE}} = 10^{\beta_0}\,\mathrm{EKE}^{\beta_1}$. Figure 5.16 compares the OLS and WLS reconstructions with the diagnosed EPE field at one snapshot. Both reconstructions reproduce the basin-scale contrast between the energetic western boundary current system and the weaker interior basin. However, the OLS reconstruction is relatively

smooth because the unweighted regression is strongly influenced by the numerous low-energy points. The WLS reconstruction, which uses $w_i = \mathrm{EKE}_i$, gives greater influence to energetic regions and better preserves enhanced EPE structures along the western boundary current, the Gulf Stream separation region, and the Gulf Stream extension.

Discrepancies nevertheless remain. In the subpolar gyre, the diagnosed EPE contains localised high-energy structures that are only partly recovered by the WLS reconstruction. The WLS field also reproduces the enhanced EPE along the Gulf Stream extension in a more spatially diffuse form, rather than capturing the sharper structure in the diagnosed field. In the subtropical and tropical parts of the basin, the reconstruction can overestimate EPE where EKE is locally elevated but the diagnosed EPE remains weak. These mismatches indicate that EKE alone does not fully determine the EPE field, especially where stratification, buoyancy fluxes, and regional dynamical structure modify the EPE–EKE relationship. Therefore, the reconstruction should be interpreted as a diagnostic illustration of the EPE–EKE relationship in energetic regions rather than as a complete parameterisation of EPE.

5.6 Summary

This chapter has diagnosed the eddy energetics of a 1/10 degree eddy-resolving North Atlantic simulation. The depth-integrated EKE and EPE fields show energetic structures concentrated around the Gulf Stream, its downstream extension, the subpolar gyre, and the western tropical North Atlantic. Their magnitudes and spatial patterns are broadly consistent with observational estimates based on Argo float and altimetry data (Roullet et al., 2014), indicating that the simulation captures the main large-scale distribution of mesoscale eddy energy.

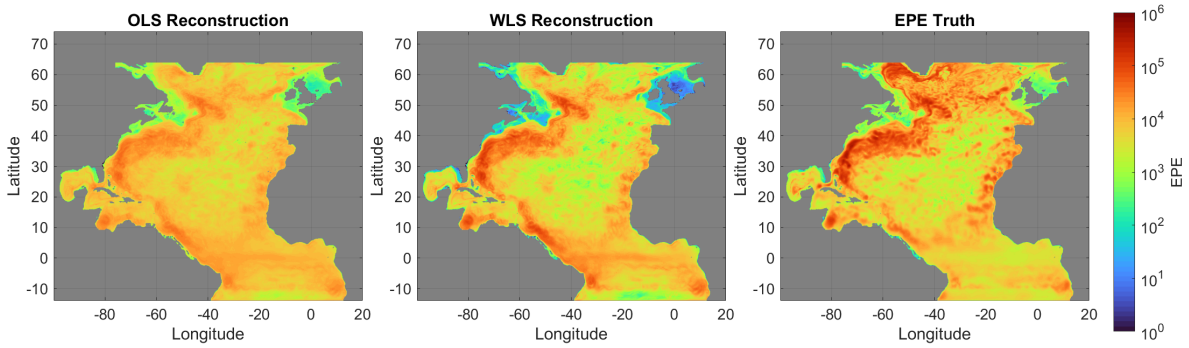


Figure 5.16: EPE reconstructed from EKE using the fitted log–log regressions. The left panel shows the OLS reconstruction, the middle panel shows the WLS reconstruction with $w_i = \mathrm{EKE}_i$, and the right panel shows the diagnosed EPE field. All panels show depth-integrated EPE ($\mathrm{kg\ s^{-2}}$) on the same logarithmic colour scale.

The eddy energy source analysis further separates the contributions from Montgomery potential, Reynolds stress, baroclinic instability, and vertical buoyancy flux. The Montgomery potential and baroclinic instability terms provide the dominant contributions, while the buoyancy flux term represents the conversion between EKE and EPE. The diagnosed source terms are strongest in the Gulf Stream region, its downstream extension, and the western tropical North Atlantic, consistent with the strong western-boundary dissipation described as the eddy-energy “graveyard" by Zhai et al. (2010). The diagnosed long Rossby wave phase speed is also consistent with the observed westward propagation of mesoscale eddies (Chelton et al., 2007, 2011).

The final part of the chapter examined the positive relationship between EPE and EKE in logarithmic space. OLS regression provides a useful baseline, but the large number of low-energy points can dominate the unweighted least-squares criterion. WLS was therefore used as a diagnostic method to emphasise energetic regions, with the final weight chosen as $w_i = \mathrm{EKE}_i$ after balancing the fitted slope, weighted and unweighted coefficients of determination, and weight concentration. The WLS fit better represents the high-EKE branch of the scatter distribution and improves the reconstruction of energetic EPE structures from EKE. However, the reduced unweighted performance of the WLS fit and the remaining reconstruction errors show that EKE alone does not fully determine the EPE field. The EPE–EKE relationship should therefore be interpreted as a useful diagnostic constraint in energetic regions, rather than as a complete parameterisation of EPE.

Chapter 6

Discussion and Conclusions

6.1 Summary of the Thesis

This thesis has investigated the role of eddy energy in constraining eddy parameterisation under the thickness-weighted average (TWA) framework. The theoretical foundation was established by reviewing the Boussinesq primitive equations in buoyancy coordinates and their corresponding TWA form, in which the eddy contributions appear through the Eliassen-Palm (E-P) stress tensor (Young, 2012). The GEOMETRIC parameterisation (Marshall et al., 2012) was also reviewed because its eddy stress closure is constrained by the total eddy energy, making the definition, budget and diagnosis of eddy energy central to its practical application. Various forms of the E-P stress tensor and their mutual transformations were then discussed following Maddison and Marshall (2013).

The second part of the thesis defined eddy kinetic energy (EKE) and eddy potential energy (EPE) under the TWA framework and derived their energy budgets. EKE naturally follows from the TWA decomposition, whereas EPE is formulated using the isopycnal average in order to preserve non-negativity and maintain consistency with the E-P stress tensor. Applying the Cauchy-Schwarz inequality shows that, in the low Rossby number limit, EKE and EPE combine to provide an en-

ergy bound for the E-P stress tensor. This identifies the energetic constraint that connects the TWA formulation with the GEOMETRIC eddy parameterisation. The subsequent derivation of the EKE, EPE and total eddy energy equations further shows that the inner product of the residual-mean velocity with the E-P stress-tensor divergence acts as the primary energy conversion term between the mean and eddy fields.

The diagnostic part of the thesis applied this framework to a $1/10^{\circ}$ eddy-resolving MITgcm simulation of the North Atlantic Ocean. The diagnosed EKE and EPE fields show energetic structures concentrated around the Gulf Stream, its downstream extension, the subpolar gyre and the western tropical North Atlantic. The eddy energy source terms were decomposed into contributions from Montgomery potential, Reynolds stress, baroclinic instability and vertical buoyancy flux. The Montgomery potential and baroclinic instability terms provide dominant contributions, while the vertical buoyancy flux represents conversion between EKE and EPE. The diagnosed source terms are strongest in the western boundary current system, consistent with the western-boundary “graveyard" of eddy energy discussed by Zhai et al. (2010). The diagnosed long Rossby wave phase speed is also broadly consistent with the observed westward propagation of mesoscale eddies (Chelton et al., 2007, 2011). Finally, the positive relationship between EPE and EKE was examined using ordinary least squares and weighted least squares regressions. The weighted regression, with $w_i = \mathrm{EKE}_i$, better represents the high-energy branch of the scatter distribution and improves the reconstruction of energetic EPE structures. Nevertheless, remaining regional mismatches show that EKE alone does not fully determine the EPE field. The EPE–EKE relationship should therefore be interpreted as a useful diagnostic constraint in energetic regions, rather than as a complete parameterisation of EPE or total eddy energy.

6.2 Future Work

Future work should first test the theoretical route proposed here in controlled numerical settings. Coarser-resolution ocean models or idealised channel configurations representative of Southern Ocean dynamics could be used to assess whether the energy constraint central to the GEOMETRIC framework can improve Gent and McWilliams (GM)-type eddy closures and their representation of unresolved eddy effects. Such experiments could follow the spirit of Mak et al. (2018), in which the eddy diffusivity is adjusted according to GEOMETRIC predictions, but should also test the assumed eddy energy budget (5.1) more directly. This would help determine whether the diagnostic energy relationships established in this thesis can be used in prognostic parameterisations.

Future extensions could also place the diagnosed TWA energy budget in a more explicitly scale-aware framework. The scale-dependent isopycnal energy-cycle analysis of Loose et al. (2023) provides a useful example of how mean–eddy energy transfers can be examined across spatial scales in an isopycnal model. In parallel, the localised APE-budget framework of Tailleux and Roullet (2025) offers a theoretical reference for comparing the present EPE diagnostic with broader regional energetics formulations.

Further diagnostic work is also required to improve the reconstruction of EPE and total eddy energy. The weighted regression analysis shows that EKE provides useful information in energetic regions, but the remaining errors indicate that additional physical controls are needed. Future predictors could include stratification, regional dynamical indicators and buoyancy-flux-related terms, especially in regions where the EPE–EKE relationship is modified by local dynamics. Longer simulations and additional model configurations with different resolutions, forcing conditions or domains would also be valuable for testing the robustness of the

diagnosed relationship across averaging windows, seasons and circulation regimes. These extensions should be evaluated using reconstruction errors together with weighted and unweighted skill metrics, so that improvements in energetic regions can be assessed without losing sight of basin-wide performance.

Finally, further work is required on the mechanisms of eddy energy dissipation, which remain difficult to represent even in eddy-permitting models. Eddy energy sinks at lateral boundaries and near the seafloor are central components of the full eddy energy budget. Potential mechanisms include bottom drag (Sen et al., 2008), lee-wave scattering (Nikurashin and Ferrari, 2010; Melet et al., 2015), and western-boundary dissipation associated with the eddy-energy “graveyard" (Zhai et al., 2010). Understanding these sinks will require ultra-high-resolution numerical process studies and more detailed diagnostics of energy transfer from resolved mesoscale eddies to smaller-scale motions.

References

Aiki, H. and Richards, K. J. (2008), "Energetics of the global ocean: The role of layer-thickness form drag", *Journal of Physical Oceanography* **38**(9), 1845–1869.

Aiki, H., Zhai, X. and Greatbatch, R. J. (2016), Energetics of the global ocean: the role of mesoscale eddies, *in* "Indo-Pacific Climate Variability and Predictability", World Scientific, pp. 109–134.

Aris, R. (2012), *Vectors, tensors and the basic equations of fluid mechanics*, Courier Corporation.

Bachman, S. and Fox-Kemper, B. (2013), "Eddy parameterization challenge suite i: Eady spindown", *Ocean Modelling* **64**, 12–28.

Bachman, S., Marshall, D., Maddison, J. and Mak, J. (2017), "Evaluation of a scalar eddy transport coefficient based on geometric constraints", *Ocean Modelling* **109**, 44–54.

Chelton, D. B., DeSzoeke, R. A., Schlax, M. G., El Naggar, K. and Siwertz, N. (1998), "Geographical variability of the first baroclinic rossby radius of deformation", *Journal of Physical Oceanography* **28**(3), 433–460.

Chelton, D. B., Schlax, M. G. and Samelson, R. M. (2011), "Global observations of nonlinear mesoscale eddies", *Progress in Oceanography* **91**(2), 167–216.

Chelton, D. B., Schlax, M. G., Samelson, R. M. and de Szoeke, R. A. (2007), "Global observations of large oceanic eddies", *Geophysical Research Letters* **34**(15).

De Szoeke, R. A. and Bennett, A. F. (1993), "Microstructure fluxes across density surfaces", *Journal of physical oceanography* **23**(10).

Eady, E. T. (1949), "Long waves and cyclone waves", *Tellus* **1**(3), 33–52.

Eden, C. and Greatbatch, R. J. (2008), "Towards a mesoscale eddy closure", *Ocean Modelling* **20**(3), 223–239.

Eyring, V., Gillett, N. P., Achuta Rao, K. M., Barimalala, R., Barreiro Parrillo, M., Bellouin, N., Cassou, C., Durack, P. J., Kosaka, Y., McGregor, S. et al. (2021), "Human influence on the climate system (chapter 3)".

Fox-Kemper, B., Ferrari, R. and Hallberg, R. (2008), "Parameterization of mixed layer eddies. part i: Theory and diagnosis", *Journal of Physical Oceanography* **38**(6), 1145–1165.

Gent, P. R. and McWilliams, J. C. (1990), "Isopycnal mixing in ocean circulation models", *Journal of Physical Oceanography* **20**(1), 150–155.

Gill, A. (1982), "Atmospheric-ocean dynamics, int. geophys. ser", *Academic Press* **30**, 662.

Grotjahn, R. (2003), Baroclinic instability, *in* J. R. Holton, ed., "Encyclopedia of Atmospheric Sciences", Academic Press, Oxford, pp. 179–188.

Jansen, M. F., Adcroft, A., Griffies, S. M. and Grooms, I. (2024), "The averaged hydrostatic boussinesq ocean equations in generalized vertical coordinates", *Journal of Advances in Modeling Earth Systems* **16**(12), e2024MS004506.

Kundu, P. K., Cohen, I. M., Dowling, D. R. and Capecelatro, J. (2024), *Fluid mechanics*, Elsevier.

Kutner, M., Nachtsheim, C., Neter, J. and Li, W. (2005), "Applied linear statistical models. mcgraw-hill", *New York* **7**.

Lee, M.-M., Marshall, D. P. and Williams, R. G. (1997), "On the eddy transfer of tracers: Advective or diffusive?", *Journal of Marine Research* **55**(3), 483–505.

Loose, N., Bachman, S., Grooms, I. and Jansen, M. (2023), "Diagnosing scale-dependent energy cycles in a high-resolution isopycnal ocean model", *Journal of Physical Oceanography* **53**(1), 157–176.

Maddison, J. R. and Marshall, D. P. (2013), "The Eliassen-Palm flux tensor", *Journal of Fluid Mechanics* **729**, 69–102.

Mak, J., Maddison, J. R., Marshall, D. P. and Munday, D. R. (2018), "Implementation of a geometrically informed and energetically constrained mesoscale eddy parameterization in an ocean circulation model", *Journal of Physical Oceanography* **48**(10), 2363–2382.

Mak, J., Marshall, D. P., Madec, G. and Maddison, J. R. (2022), "Acute sensitivity of global ocean circulation and heat content to eddy energy dissipation timescale", *Geophysical Research Letters* **49**(8), e2021GL097259.

Marshall, D. P., Maddison, J. R. and Berloff, P. S. (2012), "A framework for parameterizing eddy potential vorticity fluxes", *Journal of Physical Oceanography* **42**(4), 539–557.

Marshall, J., Adcroft, A., Hill, C., Perelman, L. and Heisey, C. (1997), "A finite-volume, incompressible navier stokes model for studies of the ocean on parallel computers", *Journal of Geophysical Research: Oceans* **102**(C3), 5753–5766.

Melet, A., Hallberg, R., Adcroft, A., Nikurashin, M. and Legg, S. (2015), "Energy

flux into internal lee waves: Sensitivity to future climate changes using linear theory and a climate model", *Journal of Climate* **28**(6), 2365–2384.

Munday, D. R., Johnson, H. L. and Marshall, D. P. (2013), "Eddy saturation of equilibrated circumpolar currents", *Journal of Physical Oceanography* **43**(3), 507–532.

Nikurashin, M. and Ferrari, R. (2010), "Radiation and dissipation of internal waves generated by geostrophic motions impinging on small-scale topography: Theory", *Journal of Physical Oceanography* **40**(5), 1055–1074.

NOAA, N. (1988), "Digital relief of the surface of the earth.", *Data Announce. 88–MGG-02* .

Qiu, B. (1999), "Seasonal eddy field modulation of the north pacific subtropical countercurrent: Topex/poseidon observations and theory", *Journal of Physical Oceanography* **29**(10), 2471–2486.

Roullet, G., Capet, X. and Maze, G. (2014), "Global interior eddy available potential energy diagnosed from argo floats", *Geophysical Research Letters* **41**(5), 1651–1656.

Sen, A., Scott, R. B. and Arbic, B. K. (2008), "Global energy dissipation rate of deep-ocean low-frequency flows by quadratic bottom boundary layer drag: Computations from current-meter data", *Geophysical Research Letters* **35**(9).

Tailleux, R. and Roullet, G. (2025), "Energetically consistent localised APE budgets for local and regional studies of stratified flow energetics", *Ocean Modelling* **197**, 102579.

Tulloch, R., Marshall, J. and Smith, K. S. (2009), "Interpretation of the propagation of surface altimetric observations in terms of planetary waves and geostrophic turbulence", *Journal of Geophysical Research: Oceans* **114**(C2).

Vallis, G. K. (2017), *Atmospheric and oceanic fluid dynamics*, Cambridge University Press.

Van Sickle, J. (2017), *Basic GIS coordinates*, 2nd ed., CRC press, Boca Raton, FL.

Visbeck, M., Marshall, J., Haine, T. and Spall, M. (1997), "Specification of eddy transfer coefficients in coarse-resolution ocean circulation models", *Journal of Physical Oceanography* **27**(3), 381–402.

Waterman, S. and Lilly, J. M. (2015), "Geometric decomposition of eddy feedbacks in barotropic systems", *Journal of Physical Oceanography* **45**(4), 1009–1024.

Young, W. R. (2012), "An exact thickness-weighted average formulation of the Boussinesq equations", *Journal of Physical Oceanography* **42**(5), 692–707.

Zhai, X., Johnson, H. L. and Marshall, D. P. (2010), "Significant sink of ocean-eddy energy near western boundaries", *Nature Geoscience* **3**(9), 608–612.

Zhai, X. and Marshall, D. P. (2013), "Vertical eddy energy fluxes in the north atlantic subtropical and subpolar gyres", *Journal of Physical Oceanography* **43**(1), 95–103.